

Double Master Degree in Automotive Engineering



**Politecnico
di Torino**



**University
of Windsor**

Thermal modelling of second-life repurposed EV battery pack

Supervisors:

Dr. B. A. Schuelke-Leech

Dr. A. Bonfitto

Dr. M. Karushev

Dr. V. Ravello

Dr. S. Panchal

Candidate:

Emanuele Lettieri

22 October 2024

Declaration of originality

I hereby certify that I am the sole author of this thesis and that no part of this thesis has been published or submitted for publication.

I certify that, to the best of my knowledge, my thesis does not infringe upon anyone's copyright nor violate any proprietary rights and that any ideas, techniques, quotations, or any other material from the work of other people included in my thesis, published or otherwise, are fully acknowledged in accordance with the standard referencing practices. Furthermore, to the extent that I have included copyrighted material that surpasses the bounds of fair dealing within the meaning of the Canada Copyright Act, I certify that I have obtained a written permission from the copyright owner(s) to include such material(s) in my thesis and have included copies of such copyright clearances to my appendix.

I declare that this is a true copy of my thesis, including any final revisions, as approved by my thesis committee and the Graduate Studies office, and that this thesis has not been submitted for a higher degree to any other University or Institution.

Abstract

Lithium-ion batteries, retired from their first life in automotive field, can still retain 70% - 80% of their original capacity. Consequently, they could be repurposed for less demanding energy storage applications, delaying or eliminating the need for new systems. However, identifying suitable second-life applications is challenging and uncertain, as lithium-ion batteries passed through their first life, do not show the same thermal behaviour and heat production of a new battery, posing safety risks if not properly managed.

This thesis focuses on high-fidelity evaluation of the thermal performance of a PHEV's battery in second-life scenarios, using limited cell information and minimal experimental data. The evaluation employs a coupled electrochemical-thermal modeling approach. The first model, developed and optimized using PyBaMM software, accurately represents cell behavior and, thanks to a lumped thermal sub-model, can evaluate the heat generated under a wide range of operating conditions. The second model, based on the battery's CAD design and implemented in the SimScale environment, assesses the thermal behaviour of the battery under various boundary conditions. These models are interdependent, as the thermal model requires heat production data estimated by the PyBaMM model, which in turn depends on the battery temperature data provided by the thermal model. Once validated by means of experimental data, the complete model is used to simulate duty cycles and boundary conditions of second life scenarios, accurately selected for the battery protagonist of this study. The implemented approach allows the evaluation of battery's suitability and safety under the new operating conditions.

The scope and execution of this thesis are exceptionally ambitious due to its multidisciplinary nature and innovative approach. Moreover, it has proven to be remarkably effective in addressing multiple facets of battery performance and safety. The integrated models have demonstrated optimal fidelity with the experimental tests, achieving exceptional average accuracy and enabling representative simulations for the selected second-life applications. The final results have shown the suitability and safety of the battery module in all the new operating scenarios.

*A Gianluigi.
Grazie per aver illuminato, fin da quando ne ho ricordo, il mio cammino e per
l'amore che ci legherà sempre, oltre la distanza e le parole.*

Acknowledgements

English Version

I would like to express my deepest gratitude to all the people who have supported me throughout my academic journey and in the realization of this thesis project.

Foremost, I extend my sincere thanks to my supervisors Dr. A.B. Schuelke-Leech from University of Windsor, Dr. M. Karushev from Acculon Energy, Dr. A. Bonfitto from Politecnico di Torino, Dr. V. Ravello from Stellantis Italia and Dr. S. Panchal from Stellantis Canada for their guidance, support and expertise. Their feedback and encouragement were instrumental in shaping this research and its outcome.

I am really grateful to the two institutions with which I took my academic path. Politecnico di Torino for teaching me the importance of dedication and hardworking to reach personal objectives. University of Windsor for allowing me be included of a immersive and multicultural environment, and felling part of it.

Furthermore I would like to express my gratitude to Prof. M. Cavatorta, Dr. O. Jianu and Dr. Ravello that, from both sides, actively worked for the collaboration between these universities for this project, supporting and encouraging its realization, and allowing me to take part to an unique and unforgettable experience.

I would like also to acknowledge the financial support of Stellantis, which made this project possible.

My final thanks go to my family, to whom I owe everything I have become today. Thank you to my parents for allowing me to freely find my path without ever letting me lack anything, for supporting and reassuring me in difficult times, but also for celebrating my successes even more than if they were their own. Thanks to my grandparents, who, with their examples of honesty, humility, and sense of duty, have passed on to me the most important values in life, allowing me to become a man of which they can be proud. Thanks to my aunts for always showing me deep and sincere affection, and for standing by my side during the important moments of my life.

Versione Italiana

Vorrei esprimere la mia più profonda gratitudine a tutte le persone che mi hanno supportato durante il mio percorso accademico e nella realizzazione di questo progetto di tesi.

Innanzitutto, rivolgo i miei sinceri ringraziamenti ai miei supervisori: alla Dott.ssa A.B. Schuelke-Leech dell'Università di Windsor, al Dr. M. Karushev di Acculon Energy, al Dr. A. Bonfitto del Politecnico di Torino, al Dr. V. Ravello di Stellantis Italia e al Dr. S. Panchal di Stellantis Canada per la loro guida, supporto ed esperienza. I loro pareri e incoraggiamenti sono stati fondamentali per lo sviluppo e l'esito di questa ricerca.

Sono davvero grato alle due istituzioni con cui ho intrapreso il mio percorso accademico. Il Politecnico di Torino, per avermi insegnato l'importanza della dedizione e del duro lavoro per raggiungere gli obiettivi personali. L'Università di Windsor, per avermi permesso di vivere in un ambiente immersivo e multiculturale, facendomi sentire parte di esso.

Inoltre, vorrei esprimere la mia gratitudine alla Prof. M. Cavatorta, alla Dott.ssa O. Jianu e al Dr. Ravello che, da entrambe le parti, hanno lavorato attivamente alla collaborazione tra queste università per questo progetto, supportandone e incoraggiandone la realizzazione e permettendomi di partecipare a un'esperienza unica e indimenticabile.

Vorrei inoltre ricordare e ringraziare il supporto finanziario di Stellantis, che ha reso possibile questo progetto.

Il mio ringraziamento finale va alla mia famiglia, alla quale devo tutto quello che sono diventato oggi. Grazie ai miei genitori per avermi permesso di trovare liberamente la mia strada, senza mai farmi mancare nulla, per avermi supportato e rassicurato nei momenti difficili, ma anche per aver celebrato i miei successi ancor più di come se fossero stati i loro. Grazie a miei nonni, che con i loro esempi di onestà, umiltà e senso del dovere, mi hanno trasmesso i valori più importanti della vita, permettendomi di diventare un uomo di cui essere orgogliosi. Grazie alle mie zie per avermi sempre dimostrato profondo e sincero affetto, e per essere state al mio fianco nei momenti importanti della mia vita.

Contents

Declaration of originality	i
Abstract	iii
Dedication	iv
Acknowledgements	v
List of Figures	x
List of Tables	xiv
List of Abbreviations	xv
1 Introduction	1
1.1 Background	1
1.2 Problem definition	4
1.3 Objective	5
1.4 Approach	6
2 Literature Review	8
2.1 Introduction to lithium-ion cells and batteries	8
2.1.1 Negative Electrode (Anode)	11
2.1.2 Positive Electrode (Cathode)	12
2.1.3 Electrolyte	12
2.1.4 Separator	12
2.1.5 Current Collectors	13
2.1.6 Cell Enclosures	13
2.2 Heat generation in lithium-ion cells	15
2.3 Cooling system types	19
2.3.1 Air cooling	20
2.3.2 Liquid cooling	21
2.3.3 PCM (Phase change material) cooling	21
2.4 Aging phenomena	22
2.4.1 Degradation modes	22

2.4.2	External factors	23
2.5	First life of the battery pack	26
2.6	Battery Models	29
2.6.1	Data-driven model (DDM)	30
2.6.2	Bucket model	31
2.6.3	Equivalent circuit model (ECM)	32
2.6.4	Electrochemical model (EM)	33
2.6.5	Modelling approach	34
2.7	Overview of electrochemical models	36
2.7.1	Single particle model (SPM)	36
2.7.2	Single particle model with electrolyte (SPMe)	36
2.7.3	Doyle–Fuller–Newman (DFN) model	37
2.7.4	Homogenised model	39
2.7.5	Microscale model	40
2.7.6	Model decision	41
2.7.7	SPMe Founding equations	44
2.8	Battery second life	47
2.8.1	Repurposing procedure	48
2.8.2	Potential configurations	49
2.8.3	Configuration decision	49
2.8.4	Second usage requirements	51
2.8.5	Second life scenarios	52
2.9	Existing literature	56
3	Methodology	58
3.1	Electrochemical model	58
3.1.1	SPMe Generation	61
3.1.2	Cell teardown and geometrical parameters measurement	63
3.1.3	Parameters optimization based on cell tests	69
3.2	Heat production within the cell	77
3.3	CAD Development	81
3.4	Thermal simulation	85
3.5	Models coupling	91
3.6	Module thermal test	92
3.7	Second life applications	97
3.7.1	Renewable solar firming	98

3.7.2	ESS for PV domestic application	100
3.7.3	Electric forklift	103
4	Results	107
4.1	Electrochemical model	107
4.1.1	Experimental data	107
4.1.2	Pre-optimization model results	108
4.1.3	Post-optimization model results	110
4.2	Coupled electrochemical-thermal model	114
4.2.1	Thermal experimental results	114
4.2.2	Model validation	122
4.3	Second life assessment	133
4.3.1	Renewable solar firming	133
4.3.2	ESS for PV domestic application	137
4.3.3	Electric forklift	140
5	Conclusion	146
6	Possible future developments	148
	References	149
	Vita auctoris	163

List of Figures

2	Early Historical Moments of Electric Vehicles.	1
3	Global CO2 emissions by sector in 2019 [127].	2
4	Global EV sales [69].	3
5	Rechargeable battery market forecast [31].	3
6	Cycle life of batteries.	4
7	HONDA CLARITY: Cell-Module-Car.	6
8	Faced fields in this thesis.	6
9	Flow chart of the thesis.	7
10	Lithium-ion battery essential parts [46].	8
11	Chemical reactions in a NMC lithium-ion cell.	9
12	Charging and discharging mechanisms in lithium-ion battery [46].	9
13	Packaging of a battery system[102].	10
14	Different battery configurations [48].	10
15	Electrodes arrangement in lithium-ion cells.	11
16	Cell components [107].	13
17	Cell configurations [43]	15
18	Illustration of categories and process of heat generation within LIBs [85].	16
19	Result of heat generation on Li-ion cell [13].	19
20	Thermal runaway process [92].	19
21	Air cooling systems [32].	20
22	Liquid cooling systems.	21
23	PCM cooling [21].	22
24	Graphical representation of LIBs degradation modes and external factors [28].	25
25	HONDA CLARITY PHEV [125].	26
26	Typical battery SOC profile for a PHEV [125].	27
27	IPU Technologies [125].	27
28	IPU Cooling system [125].	29
29	Battery modelling types	32
30	Sketch of the geometry of the SPMe model [17].	38
31	Sketch of the geometry of DFN model [17].	39
32	Sketch of the geometry of the homogenised model [17].	41
33	Sketch of the microscale model [17].	42

34	PyBaMM architecture [115].	58
35	PyBaMM code for SPMe creation, data set population and example of a simulation set-up.	61
36	Result of the simulation example.	62
37	Data set update with cell specifications.	63
38	Disassembled cell.	64
39	Extraction equipment	65
40	Cell case puncture and draw of the electrolyte not absorbed by electrodes.	65
41	Electrodes extraction.	66
42	Stripped electrodes/separator and voltage measurement.	67
43	Thickness measurements.	67
44	Width measurements.	68
45	Electrodes unrolling, spreading and electrodes length measurement.	68
46	Data set update with measured parameters.	69
47	Ranking of the normalized parameter sensitivity for terminal voltage [80].	72
48	Results of preliminary optimization.	74
49	Objective function cost landscape of preliminary optimization.	75
50	Data set update with optimized parameters.	77
51	PyBaMM code for SPMe with lumped thermal sub-model creation, data set population and example of a simulation set-up.	79
52	Result of the simulation example.	80
53	CAD Model of the cell.	82
54	CAD Model of the module.	83
55	Serpentine cooling plate.	84
56	Module's internal flow volumes.	86
57	Simulation global settings.	87
58	Model gravity.	87
59	Simulation boundary conditions.	89
60	Power sources selection.	89
61	Mesh settings.	91
62	Coupling between electrochemical and thermal models.	92
63	Module within adiabatic styrofoam chamber.	94
64	Thermistors set-up on the module.	96
65	PV plant with its ESSs [44].	98

66	Duty cycle signal for renewables solar firming application [112].	99
67	PV and ESS in a residential application [55].	100
68	PV generation in summer [41].	101
69	Scheduling plan for domestic appliances [41].	102
70	Hypothetical charging and discharging power of ESS under optimal scheduling.	102
71	Electric forklift [62].	104
72	Total power drawn from storage system during an hypothetical forklift's duty cycle [121].	104
73	Results of experimental tests on the cell.	108
74	Model match of experimental data before optimization.	109
75	Model match of experimental discharge curves after optimization.	110
76	Model match of experimental CC-CV charge/CC discharge curves after optimization.	111
77	Model match of GITT at 40A and 25°C.	112
78	Model match of GITT at 40A and 45°C.	112
79	Thermistors measurements on Cell 6 with initial temperature 24°C.	115
80	Thermistors measurements at cells bottom with initial temperature 24°C.	116
81	Thermistors measurements within adiabatic chamber.	118
82	Thermistors measurements on Cell 6 with high initial temperature.	119
83	Thermistors measurements at cells bottom with high initial temperature	120
84	Thermistors measurements within adiabatic chamber.	121
85	Cells voltage record during thermal tests.	121
86	Outcomes of PyBaMM models for the simulated discharge at initial temperature 24°C.	124
87	Simulation match with thermistors measurements on cell 6, for the test with initial temperature 24°C.	126
88	Simulation match with thermistors measurements on cells 6, 9 and 12, for the test with initial temperature 24°C.	127
89	Outcomes of PyBaMM models for the simulated discharge at high initial temperature.	128
90	Simulation match with thermistors measurements on cell 6, for the test with high initial temperature.	130

91	Simulation match with thermistors measurements on cells 6, 9 and 12, for the test with high initial temperature.	131
92	Solar firming duty cycle.	134
93	Jelly rolls temperature evolution in solar firming duty cycle.	135
94	Module temperature at the end of firming duty cycle.	136
95	Domestic ESS duty cycle.	137
96	Jelly rolls temperature evolution in domestic ESS duty cycle.	138
97	Module temperature at the end of domestic ESS duty cycle.	139
98	Forklift voltage duty cycle.	140
99	Forklift current duty cycle.	141
100	Forklift power duty cycle.	142
101	Forklift heat production duty cycle.	142
102	Jelly rolls temperature evolution in forklift duty cycle.	143
103	Module temperature at the end of forklift duty cycle.	144

List of Tables

1	Cell enclosures characteristics [67].	14
2	Cell specifications [125].	28
3	Battery models summary.	34
4	Electrochemical model summary.	43
5	Model variables.	44
6	Model parameters and functions.	44
7	Model constants.	45
8	List of symbols used in SPMe equations.	45
9	Summary of main advantages and drawbacks of the second life application configuration [96].	50
10	Requirements observed in this thesis for second life application decision and design.	52
11	Mobile second-life applications [93].	55
12	Stationary second-life applications [93].	55
13	Literature analysis	57
14	Measured geometrical parameters of the cell	69
15	Range of optimization for the parameter values [80].	76
16	Material and properties of module and cell components.	85
17	Thermistors position.	95
18	Battery pack characteristics in second life applications.	106

List of Abbreviations

ANN:	Artificial neural network.
BESS:	Battery energy storage system.
BMS:	Battery management system.
DDM:	Data-driven model.
DNN:	Deep neural network.
DFN:	Doyle Fuller Newman.
DOD:	Depth of discharge.
CC:	Constant current.
CV:	Constant voltage.
ECM:	Equivalent circuit model.
EM:	Electrochemical model.
EMS:	Energy management system.
EOFL:	End of first life.
ESS:	Energy storage system.
EV:	Electric vehicle.
GITT:	Galvanostatic intermittent titration technique
HPPC:	Hybrid pulse power characterization.
HV:	Hybrid vehicle.
LAM:	Loss of active material.
LIB:	Lithium-ion batteries.
LLI:	Loss of active lithium inventory.
OCV:	Open circuit voltage.
OEM:	Original equipment manufactures.

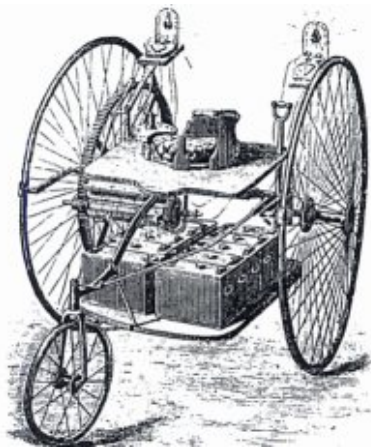
PDE:	Partial differential equation.
PHEV:	Plug-in hybrid electric vehicle.
PV:	Photovoltaic.
RC:	Resistance-capacitance.
RUL:	Remaining useful life.
SEI:	Solid electrolyte interface.
SLB:	Second life battery.
SLBESS:	Second life battery energy storage system.
SOC:	State of charge.
SOH:	State of health.
SPM:	Single particle model.
SPMe:	Single particle model with electrolyte.
SVM:	Support vector machine.
TMS:	Thermal management system.
UPS:	Uninterruptible power supply.
2D:	Two-dimensional.
3D:	Three-dimensional.

1 Introduction

1.1 Background

The employment of batteries in propulsion and automotive field is nothing new, but it is possible to assert that it has been used since the very invention of automobiles. In the second half of the 19th century, in fact, the French Gustave Trouvè realized what is considered the first electric vehicle, based on electrochemical lead battery and DC electric motor inventions [107]. Other vehicle were realized in the successive years, with two examples are in Figures 2a and 2b.

Thanks to the increasing availability of the lead batteries, several improvements were done in the following years, culminating in 1899, when Jamais Contente's electric vehicle reached the max speed world record with near 106 km/h [107]. This event confirms how, at the beginning of 20th century, the battery electric vehicles (BEVs) performance and reliability levels were higher than ICE based ones. However, the pros of the battery electric propulsion systems including higher efficiency, no direct noxious emission, largely lower acoustic noise and higher quality and regulation in the motor torque have not been enough to overcome the advantages of internal combustion engine (ICE) based ones. In the road applications, without a continuous connection to the electric grid, the poor specific energy and energy density of the electrochemical batteries, plus very long recharge time (hours), made the battery electric vehicles worse than the ICE based ones.



(a) Ayrton and Perry electric motor based three-wheeler (1882) [42] .



(b) The Camille Jenatzy speed record Jamais Contente electric vehicle (1898) [45].

Figure 2: Early Historical Moments of Electric Vehicles.

In 20th century, several efforts were made to promote the diffusion of electric vehicles: during the second world war due to oil shortage; in the seventies, with the

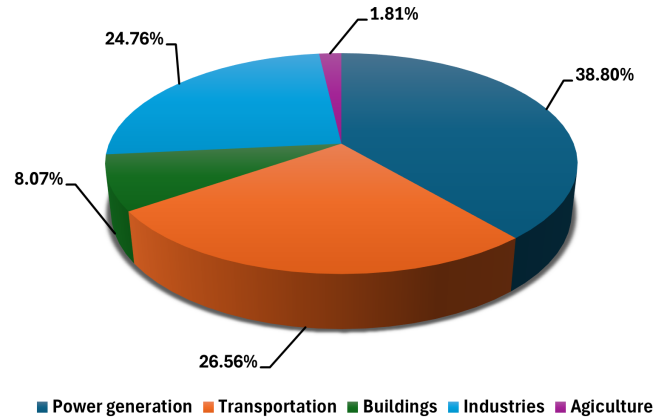


Figure 3: Global CO₂ emissions by sector in 2019 [127].

first predictions of the oil shortage and in the nineties, with the increasing pollution problems in the big metropolitan areas (California Clean Air Act). However no real mass market appreciable results were experienced [107].

Nowadays, as shown in the pie chart in Figure 3, the transportation sector emits more than 190 billion Mt of CO₂, representing 26.56% of the total emissions [127]. The increasing level of pollutants and green house effects, coupled with a dramatic climate change that will lead to an increase of the atmospheric temperature of 2°C by 2050, pushed both institutions and car manufacturers to finally make a real effort to make truly the advent of electric vehicles. Indeed, all electric vehicles produce zero direct emissions (tank-to-wheel), contributing to improve air quality of the atmosphere. As a consequence, driven by the government and the market, pure electric vehicles (EVs) and plug-in hybrid EVs (PHEVs) have been rapidly developed and employed [64]. According to the global EV sales database, part of which is reported in Figure 4, EVs and PHEVs reached over 6.4 million units in 2021 [69].

Among all the different types of available batteries on the market (e.g. nickel metal hydride, nickel cadmium and lead acid), lithium-ion (Li-ion) batteries are the most widespread typology for EV applications (as well evident in Figure 5, due to their numerous advantages [94][99] [30]:

- relatively high energy density of typically 0.4-2.4 MJ/L;
- low maintenance;
- long life service;
- good cycling performance;

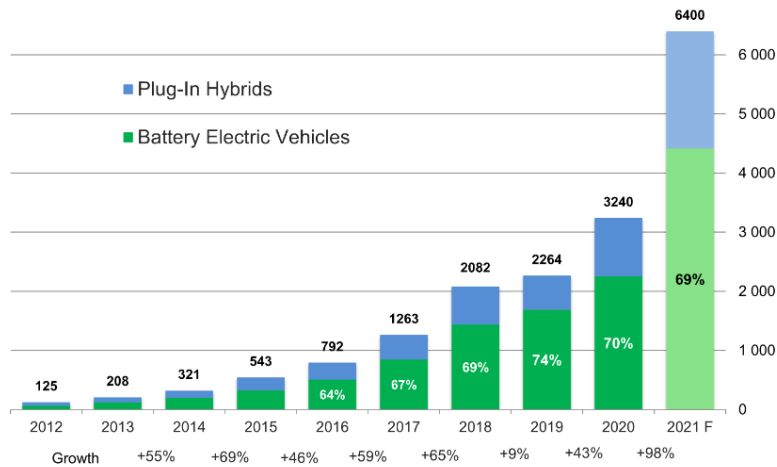


Figure 4: Global EV sales [69].

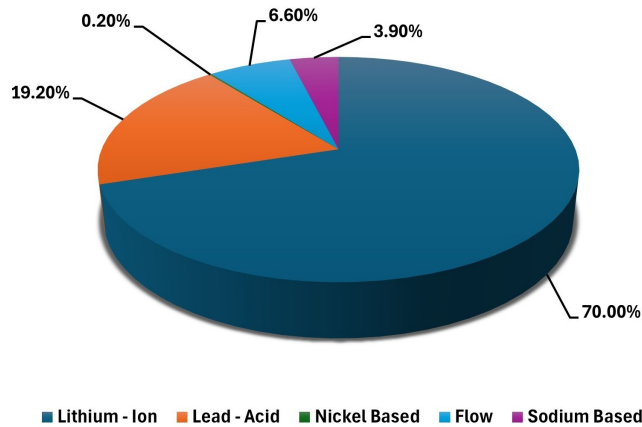


Figure 5: Rechargeable battery market forecast [31].

- low self discharge;
- no memory effect;
- high operating voltage;
- fast charge capability;

As a consequence, an enormous number of lithium-ion batteries have been used in the last years: 14 GWh or 102000 ton have been retired from EVs, a number that will double every five years [100]. After serving in vehicles for a span of eight to ten years in fact, these batteries are typically retired due to diminished capacity and inadequate power to meet driving requirements [65]. Nonetheless, these retired batteries still preserve 70%–80% of their original capacity [110], as shown in Figure 6a. Therefore they are still capable of providing storage service in

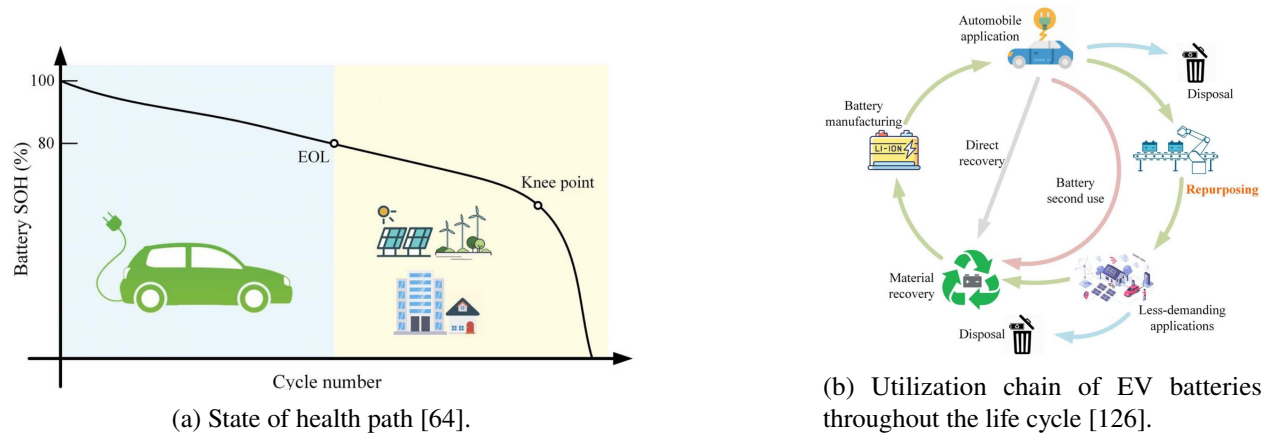


Figure 6: Cycle life of batteries.

less-demanding applications, in which battery performance, volume and weight are not critical requirements [89]. This approach could extend the operational life of retired batteries, avoiding or deferring the manufacturing of new systems. Figure 6b shows a complete battery cycle life, characterized by direct recovery or second usage.

Emilsson et al. [29] estimated the emission of more than 106 kg of CO₂ per each kWh of new lithium-ion battery manufactured. Consequently, the emission savings due to the utilization of existing energy system would be enormous. Furthermore it would alleviate the environmental footprint and material recovery pressures associated with battery decommissioning, providing also cost benefits for EV buyers. Additionally, the battery reusing could even provide an alternative revenue stream for a sub-product that otherwise would be at disposal stage. This aspect is increasingly getting the attention of important Original Equipment Manufactures (OEMs) like Nissan-Renault, BMW, Tesla or Daimler [34].

1.2 Problem definition

In order to assess the field of future application of a battery after its first life in the automotive field, a deep knowledge about characteristics, performance and "managing how" of the constituting cells is crucial. However, it is a matter of fact that the information about a cell provided by the manufacturers are always particularly limited, with complete absence of details about the internal construction and components properties, due to trade secret and know how maintenance. Additionally, first automotive usage can drastically change the cell behaviour, resulting not only in capacity fade, but also in the variation of other parameters, moving them away from design conditions and altering the normal functioning of

the battery.

Despite their advantages, lithium-ion batteries are highly thermal sensitive and can become dangerous if not properly managed. Due to the high specific energy and energy density, and chemical composition, they are subjected to heat generation, which may induce overheating [90], thermal runaway [99] and even cause fire and explosion [2]. Precisely because of this, heat generation and temperature control in LIBs are the most important issues that should be addressed in the choice of a second life application. Such decision is particularly challenging and must never be taken for granted.

1.3 Objective

This thesis has the scope of solving this tangled situation, simulating a condition in which, thermal performance and electrical characteristics of an HONDA CLARITY's battery (Figure 7), chosen for its ease obtainability, must be evaluated in order to define its second life application. In particular, thermal performance evaluation will be carried out by means of a double modelling approach, consisting of a battery model and a thermal model, coupled together.

The target of this study is not common or predictable, but rather particularly daring: the achievement of the highest possible accuracy of the modelling resorting to very limited information about the battery. Indeed, it could be identified as a "black box", with information mainly related to nominal characteristics and completely missing construction/test data, and knowledge about the first life and usage.

As it is evident from Figure 8, scope and realization of this thesis work are more audacious than ever, due to its multidisciplinary nature. Several aspects will be faced and touched, resulting in an innovative and, as ever, useful work. These characteristics highlight the contribution that this study can bring to the literature: no existing studies are in fact comparable, making it essential to fill this gap. This aspect will be further and deeply discussed in the last part of the methodology, in section 2.9.



(a) Cell of Honda Clarity [50].



(b) Module of Honda Clarity [53].



(c) Honda Clarity PHEV [60].

Figure 7: HONDA CLARITY: Cell-Module-Car.

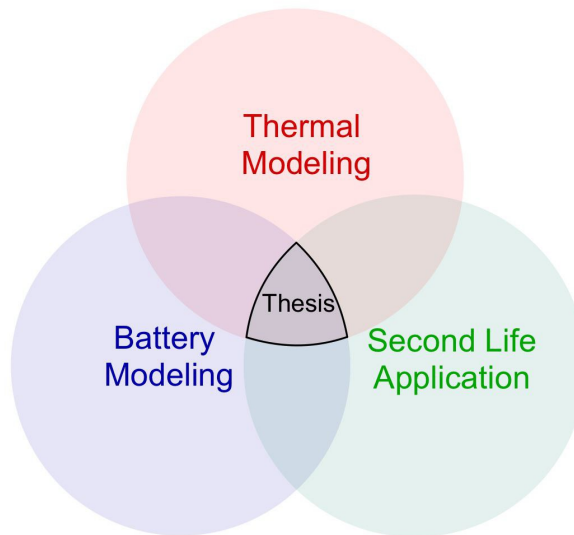


Figure 8: Faced fields in this thesis.

1.4 Approach

The study will be implemented methodologically in different steps, well schematized in Figure 9. The starting point will be the realization of an accurate cell model, based on literature, measured and optimized parameters. This model will be used to estimate the heat produced by the cell during any kind of discharge/charge cycle. This information will be used to model the cell as a heat power source that, coupled with a CAD model of the module, will allow to implement a thermal simulation. This model will be validated using temperature test on the real module. Thereafter, known the characteristic of the module, different second usage scenarios will be analyzed and chosen. By means of the thermal model it will be possible to simulate the duty cycle (in terms of required power and current) and boundary condition (in terms of cooling) of the chosen application, verifying the thermal performance of

the module and, finally, assessing it for the second application life.

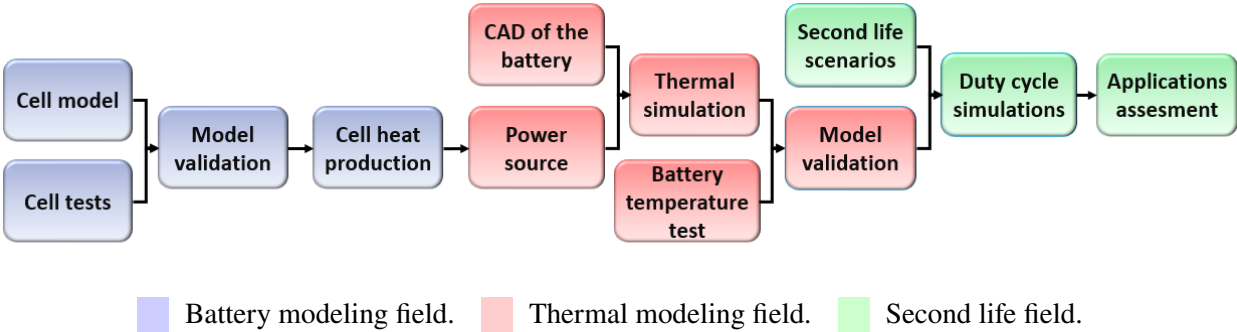


Figure 9: Flow chart of the thesis.

2 Literature Review

2.1 Introduction to lithium-ion cells and batteries

The objective of this first section of the literature review is to give a brief introduction about lithium-ion cell functioning and peculiarities, including also the critical aspects related to this kind of energy storing system. Most of the information is taken from [94], thus take it as a reference for a deeper understanding.

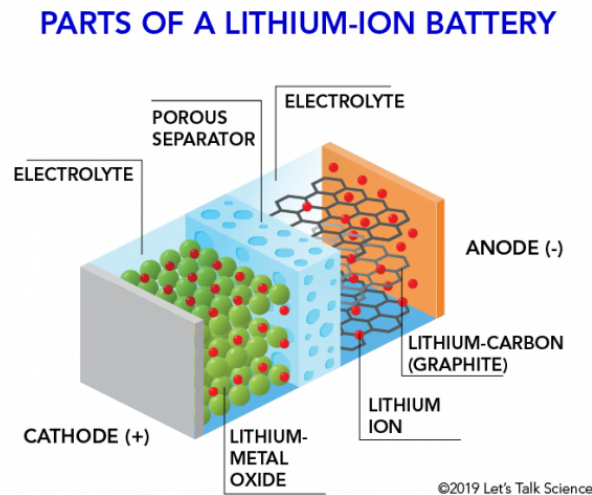


Figure 10: Lithium-ion battery essential parts [46].

The term lithium-ion refers to an entire family of battery chemistry where the negative electrode (anode) and positive electrode (cathode) serve as a host for the lithium ions (Li^+). Figure 10 shows essential components of this technology. During discharging phases, the ions are extracted from the anode (deintercalation mechanism), enter the liquid phase, migrate through the separator and reach the metal oxide cathode (intercalation mechanism). During charging phase, the ions leave the cathode (deintercalation mechanism), enter the liquid phase, migrate through the separator and are inserted in the anode (intercalation mechanism). The current moves out from the positive pole of the battery in discharge mode and moves in the positive pole in charge mode [107]. Since lithium ions are intercalated into host materials during charge or discharge, there is no free metal within a lithium-ion cell. Figures 11 and 12 respectively show chemical reactions and graphical representation of the charging/discharging processes.

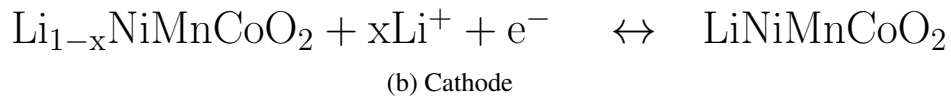
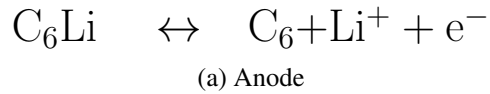
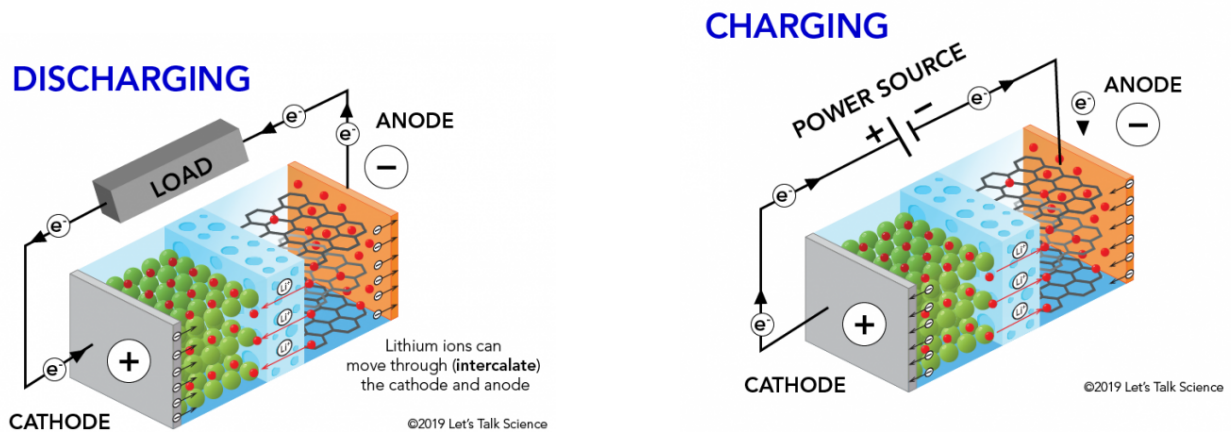


Figure 11: Chemical reactions in a NMC lithium-ion cell.



(a) Discharging phase in a lithium-ion battery : deintercalation from the anode - intercalation into the cathode.

(b) Charging phase in a lithium-ion battery : deintercalation from the cathode - intercalation into the anode.

Figure 12: Charging and discharging mechanisms in lithium-ion battery [46].

Usually the cells are connected to form a module , which is used to facilitate readily changed configurations and easy replacement. Modules can be further connected in series and/or in parallel to form a full battery pack equipped with their protection electronics. An illustration of this procedure can be seen in Figure 13.

By connecting cells (but also modules) in parallel and in series is increased respectively capacity (Ah) and voltage (V) of the system. Cells and modules are connected mostly of the time both in series and in parallel, with a configuration depending on application type and desired performance. An example of this method is shown in Figure 14.

Indeed, one of the main issues of the batteries cells is the practical impossibility to design the cells to have at the same time:

- the highest specific power (to satisfy limited time requests). Typically more inactive material for current /power transfer resulting in lower Whr/kg and Whr/l;

- the highest specific energy (to satisfy long duration requests). Typically more active material for current/power transfer resulting in higher Whr/kg and Whr/l.

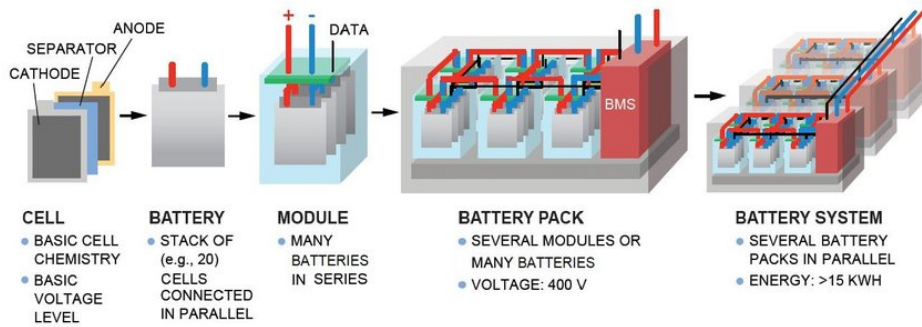


Figure 13: Packaging of a battery system[102].

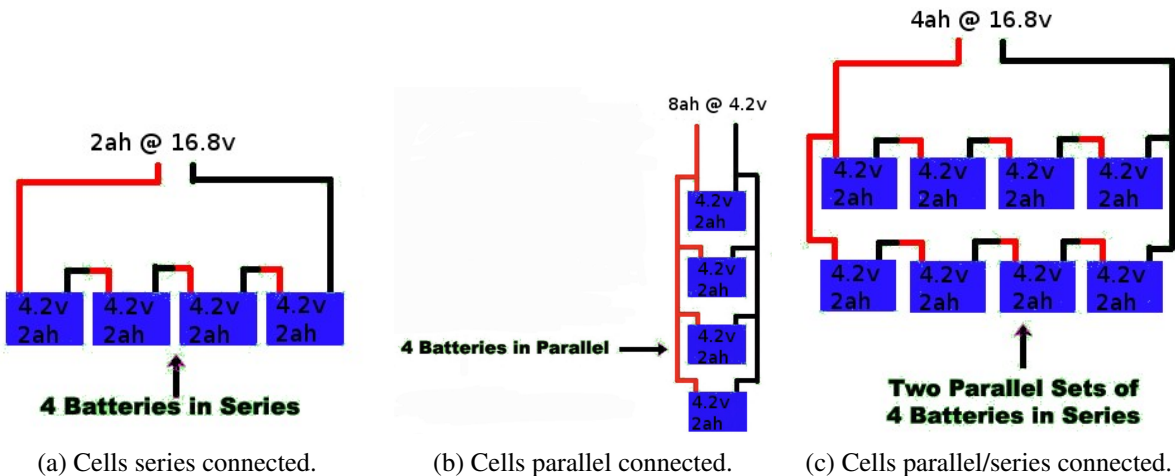


Figure 14: Different battery configurations [48].

In a lithium-ion cell, alternating layers of anode and cathode are separated by a porous film called separator. An electrolyte provides the media for lithium ion transport. A cell can be constructed by stacking alternating layers of electrodes (as shown in Figure 15a) or by winding long strips of electrodes into "jelly roll" configuration (as shown in Figure 15b). Electrode stacks or rolls can be inserted into hard cases that are sealed with gaskets, laser-welded hard cases or enclosed in foil pouches with heat-sealed seams.

Cell components, chemistry, electrode materials, particle sizes, particle size distributions, coatings on individual particles, binder materials, cell construction styles, etc., are typically chosen by a cell designer to optimize a range of cell properties and performance criteria. As a result, there is no "standard" lithium-

ion cell, and even seemingly identical cells can exhibit significantly different performance and safety behaviours.

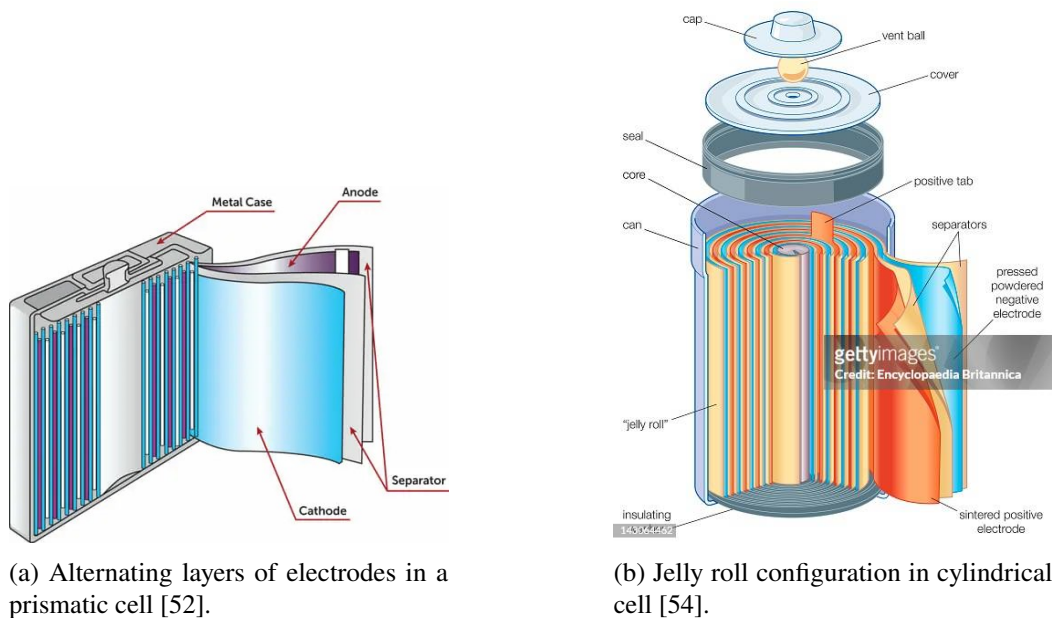


Figure 15: Electrodes arrangement in lithium-ion cells.

Currently, the market is dominated by lithium-ion cells with similar designs: a negative electrode made from carbon/graphite coated onto a copper current collector, a metal oxide positive electrode coated onto an aluminum current collector, a polymeric separator, and an electrolyte composed of a lithium salt in an organic solvent. In next sections each of these components is briefly described.

2.1.1 Negative Electrode (Anode)

The negative electrode (Figure 16c) consists of a thin layer of lithium intercalation compound applied to a metal (copper) current collector. Typically, the used anode material is carbon type, commonly graphite, in a powdered state, mixed with a binder material. There have been attempts to produce and test anodes made from silicon, germanium, and Titanate ($Li_4Ti_5O_{12}$) materials. Achieving thin and uniform coatings of active material is crucial in cells utilizing organic electrolytes. Therefore, the process of mixing and coating the negative electrode material is often proprietary, given that variations in processing parameters significantly impact the resulting coating, influencing cell capacity, rate capability and aging behaviour.

2.1.2 Positive Electrode (Cathode)

Various positive electrode materials are utilized in conventional lithium-ion cells, they are in powder form, mixed with conductivity enhancers (such as carbon) and binder (Figure 16a). Subsequently, they are coated in a thin layer onto a metallic (Aluminum) current collector. Numerous cathode materials exist, with the most prevalent being lithium cobalt dioxide. Nevertheless, alternative materials include lithium iron phosphate ($LiFePO_4$), spinels like lithium manganese oxide ($LiMn_2O_4$), or mixed metal oxides incorporating cobalt (Co), nickel (Ni), aluminum (Al), and manganese oxides, such as nickel cobalt aluminate (NCA) material ($LiNi_{0.8}Co_{0.15}Al_{0.05}O_2$) or nickel manganese cobaltite (NMC) material ($LiNi_{1/3}Mn_{1/3}Co_{1/3}O_2$). Similar to negative electrode materials, positive electrode materials can exhibit significant variations based on factors like their source, purity, particle characteristics, coatings on particles, use of dopants, mixture ratios of various components, degree of compaction, crystallinity, and more.

2.1.3 Electrolyte

The electrolyte in a lithium-ion cell acts as a carrier for ion flow between the electrodes and it typically consists of a blend of organic carbonates, like ethylene carbonate or diethyl carbonate. The specific proportions in the mixture vary based on the desired properties of the cell. These solvents contain lithium ions in a solvated state, provided by lithium salts, with lithium hexafluorophosphate (LiPF₆) being the most commonly used. Cell manufacturers usually incorporate small amounts of various additives to enhance performance characteristics such as resistance to overcharging, cycle life, calendar life, and overall cell stability.

Under typical cell voltages, combinations of lithiated carbon (or lithium metal) and organic electrolyte are not thermodynamically stable, leading to a reaction between the two materials. This reaction, occurring near room temperature, results in the formation of a protective layer on the carbon surface, commonly known as the solid electrolyte interphase (SEI). During cell manufacturing and post-assembly, the cell undergoes a gradual charging process referred to as "cell formation". This process aims to create a consistent and stable SEI layer on the cell's anode.

2.1.4 Separator

Lithium-ion cell separator (Figure 16b) is a porous membrane between the positive and negative electrodes. The primary role of the separator is to prevent direct contact between the anode and cathode, making pass, thanks to its porous nature, during



Figure 16: Cell components [107].

both charging and discharging phases, only positive ions. Commonly it is made from porous materials like polyethylene, polypropylene, or a combination of both, known as composite polyethylene / polypropylene films. Separator characteristics, including thickness, porosity, permeability, toughness, and resistance to penetration, can vary significantly based on the desired properties of the cell.

2.1.5 Current Collectors

Current collectors (one for each electrode) connect the cell to other cells and/or electric sources/loads. Their role is to transfer current evenly throughout the cell to the active material and to provide mechanical support for the active material. The most common current collectors are thin foils of copper (used as a substrate for anode active materials) and aluminum (used as a substrate for cathode active materials).

2.1.6 Cell Enclosures

There are three kinds of battery cells commonly used in EVs and they can be broadly categorized as:

- Cylindrical cells.
- Prismatic cells.
- Pouch cells.

The primary distinction among cell formats is found in their structural design and the spatial arrangement of the cathode, anode, and separator components. Prismatic and cylindrical cells are encased in rigid housings, typically constructed from aluminum or stainless steel, providing robust protection. Conversely, pouch cells are enclosed in multilayer aluminum composite foils, offering a more flexible and lightweight packaging solution.

Table 1: Cell enclosures characteristics [67].

Type	Cylindrical	Prismatic	Pouch
Packaging material	Metal can	Metal can	Foil
Electrodes	Wound or Stacked	Wound	Stacked(or semi-wound)
Cell expansion	None	Mild, requires compression.	Moderate, requires compression.
Thermal	Tabs on opposite ends - difficult interface for liquid cooling.	Tabs on opposite side where cold-plate typically interfaces.	Heat rejection through aluminum heatsinks and cold-plate.
Safety	Small-format cells able to contain failure events at cell level.	Large-format cells more difficult to pass single-cell propagation.	Large-format cells more difficult to pass single-cell propagation, unpredictable pressure release.
Terminals material	Typically nickel plated steel.	Aluminum (cathode) and plated copper (anode).	Aluminum (cathode) and plated copper (anode).
Advantages	<ul style="list-style-type: none"> • Efficient heat dissipation. • High energy density. • Robust structure. 	<ul style="list-style-type: none"> • Space efficiency. • Simplified packaging. 	<ul style="list-style-type: none"> • Flexibility in design. • Lightweight. • Cost-effective production.
Disadvantages	<ul style="list-style-type: none"> • Space inefficiency. 	<ul style="list-style-type: none"> • Heat dissipation. • Lower energy density. 	<ul style="list-style-type: none"> • Durability. • Thermal management.

In cylindrical cells, the electrode sheets are wound together with separators to create a compact jelly roll structure. Prismatic cells, on the other hand, utilize either flat jelly rolls or stacked electrodes, providing a more uniform shape conducive to space-efficient design. Pouch cells exclusively adopt a stacked configuration, which allows for a thinner and more adaptable cell profile [7].

In Table 1 are summarized the main characteristics of the cell enclosures, while Figure 17 illustrates the three different cell configurations, highlighting the unique design features and structural differences of each format.

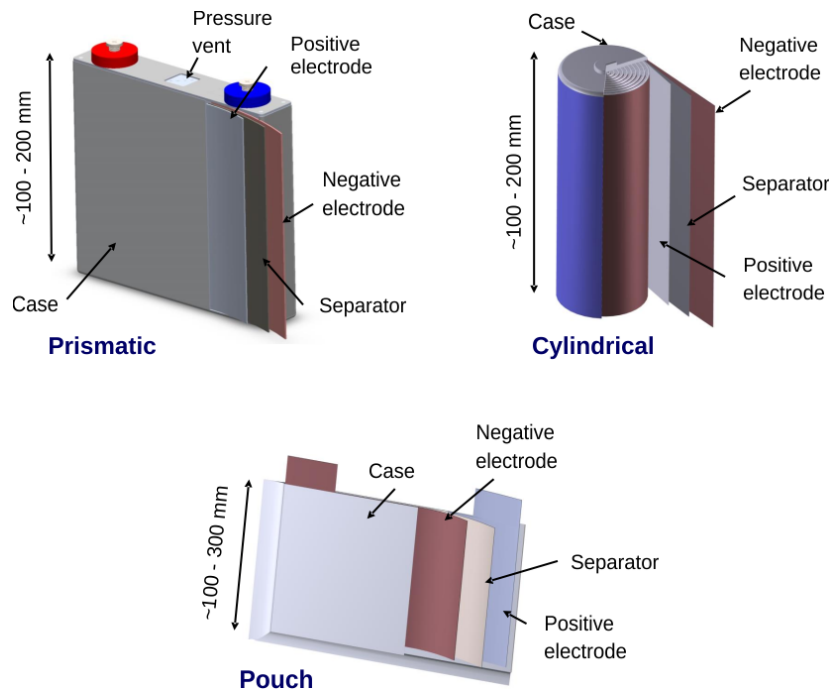


Figure 17: Cell configurations [43] .

2.2 Heat generation in lithium-ion cells

As mentioned in "Problem definition " (section 1.2), thermal management plays a crucial role when handling lithium-ion batteries. Performance, life and safety are in fact all strongly effected by operation and storage temperatures [10], which should be maintain in proper thresholds.

When the temperature is too low (e.g.10°C), the diffusion rate of lithium-ions in the electrolyte seriously decreases, resulting in significant increase of internal resistance. Furthermore the number of ions participating in the reaction decreases, affecting electricity storage and release, and leading to the attenuation of battery capacity and power. Also the charging in such condition is problematic, with lithium dendrites that may pierce the film, forming an internal short circuit and threatening

the safety of use [131]. The only solution is a proper thermal management coupled with effective heating strategies. In any case, the low temperature operations remedies will not be the focus of this thesis, which, instead, will focus on high temperatures operations (e.g. $>50^{\circ}\text{C}$) and managing strategies. Consequently, it is fundamental to understand the mechanisms of heat production within a cell.

Firstly the produced heat can be reversible or irreversible. Reversible heat is generated at cathode and anode level. It is entropic heat originated from reversible entropy change during the electrochemical reactions. This heat may be endothermic or exothermic type, but in any case is due to insertion and de-insertion of lithium ions in electrodes. The irreversible heat is generated at electrodes, electrolyte, and current collector. It has major contribution of more than 70% of total heat and is characterized by the Joule heating of the battery cell, which is C-rate dependant [131]. Figure 18 summarizes the contributions of heat generation process within a cell.

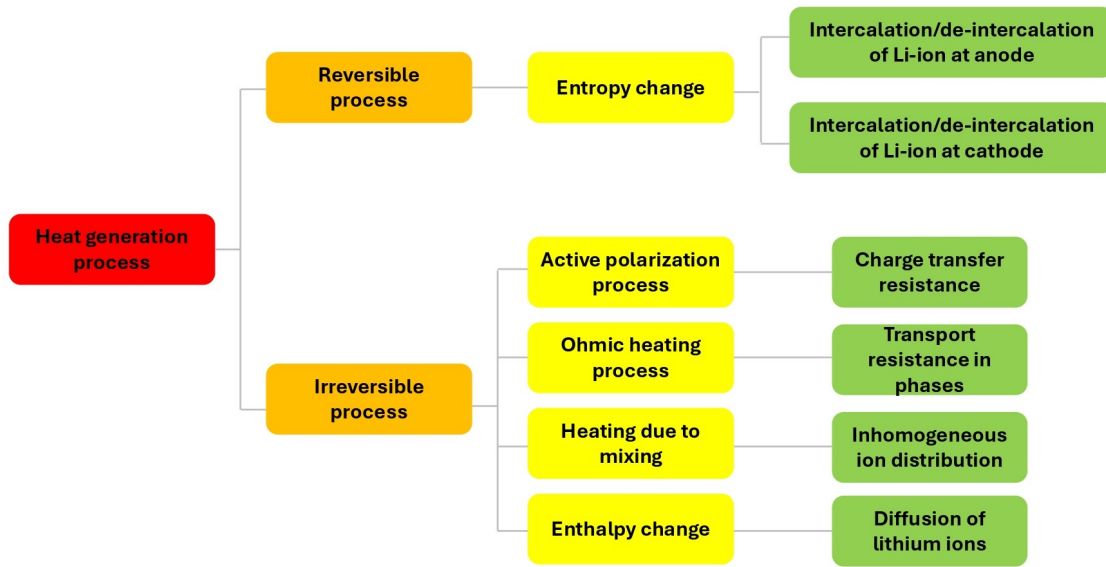


Figure 18: Illustration of categories and process of heat generation within LIBs [85].

Several theoretical studies have been conducted in order to formulate a mathematical expression to describe the heat production within a cell.

Bernardi et al. [12] derived the expression of battery heat by applying the first law of thermodynamics around the cell control volume (not including current

collectors), obtaining the following expression for heat generation inside a battery:

$$\begin{aligned}
q = & -IV - \sum_l I_l T^2 \frac{dU_{l,\text{avg}}}{dT} \\
& + \sum_j \frac{d}{dt} \left[\int_{v_j} \sum_i c_{i,j} RT^2 \frac{\delta}{\delta T} \ln \left(\frac{\gamma_{i,g}}{\gamma_{i,j}^{\text{avg}}} \right) dv_j \right] \\
& + \sum_{j,j \neq m} \sum_i \left[\left(\Delta H_{i,j \rightarrow m}^O - RT^2 \frac{d}{dT} \ln \frac{\gamma_{i,m}^{\text{avg}}}{\gamma_{i,j}^{\text{avg}}} \right) \frac{dn_{i,j}}{dt} \right]
\end{aligned} \tag{1}$$

The first term on the right-hand-side is the electrical power produced by the battery. The second term is the sum of producible reversible work and entropic heating from the reaction and it is summed over all simultaneously occurring reactions. The third term is heat produced from mixing. Since the reaction rates are not uniform, concentration variations across the battery are developed as the reaction proceeds. When the current is interrupted, the concentration gradients developed inside the battery relax, causing heat to be released or absorbed.

Rao and Newman [106] presented two different methodologies for estimating heat generation: a thermodynamic energy balance and a local heat generation model. In the first approach, neglecting phase change and mixing effect, they arrived at the following expression for the battery heat generation:

$$q = - \int_v \left(\sum_l a i_{n,l} U_{H,l} dv \right) - IV \tag{2}$$

The first term is the average enthalpy potential integrated where the reactions are actually taking place across the thickness of the battery.

In the second approach, the local heat generation is the summation of all the relevant local thermal effects occurring inside the battery, including heat generated at the electrochemical interfaces and in the bulk material in different parts of the cell. The resultant equation is:

$$q'' = i(\eta_a + \Delta\phi_s) + \int_{x_1}^{x_2} \left(a i_n \eta_c - i_1 \frac{d\phi_1}{dx} - i_2 \frac{d\phi_2}{dx} \right) dx \tag{3}$$

After integrating these expressions and applying the appropriate boundary conditions, the above expression is equivalent to the energy balance method.

In addition to electrochemical heat generation, Joule heating is produced from bulk electron movement in the current collectors. With a two-dimensional (2D) model, consisting of two electrode current collectors coupled via a temperature-independent parametrized electrochemical model, Kim et al. [75] proposed the following local heat generation rate:

$$q''' = i''' \left(U - V - T \frac{\delta U}{\delta T} \right) + \left(\sigma |\nabla \phi|^2 \right)_{cc,pos} + \left(\sigma |\nabla \phi|^2 \right)_{cc,neg} \quad (4)$$

The first term is the electrochemical heat generation already present in the other equations. The last two terms are resistive heating due to current movement in the positive and negative metal current collectors, respectively [10].

As it is clear from the previous expressions, heat production mechanisms is at the base of normal function of a lithium-ion cell. However, the heat must be properly and accurately managed in each phase of cell operation, with the scope of avoiding several dramatic consequences. Indeed, the untreated heat production within a battery leads to an increase of temperature, stimulating degradation in each of the cell components, as depicted in Figure 19:

- Degradation of the cathode is due to the development of surface film which lowers the reaction rate for both lithium-ion intercalation and de-intercalation. This will decrease the charge transfer rate and ultimately transport rate.
- Degradation in the graphite electrode is mainly due to evolution of SEI layer, that, not being completely permeable for lithium-ion, decreases the charge transfer rate. Solvent could co-intercalate into carbon and the expansion of carbon particle forms ternary graphite intercalation compound, leading active material loss and contributing to capacity loss.
- The electrolyte ($LiPF_6$) breaks into Lithium fluoride (LiF) and Phosphorous pentafluoride (PF_5), which can originate corrosive and poisonous gases. At higher temperatures (90-120°C), solid electrolyte interface layer decomposes, followed by electrolyte (above 200°C), which releases toxic gases (e.g CO , C_2H_4 , H_2S , HF).
- The separator starts melting above 140°C, slowing and even blocking the flow.

The degradation of cell components is not the only consequence of untreated heat production and temperature raise: an excessive overheating can induce a dramatic

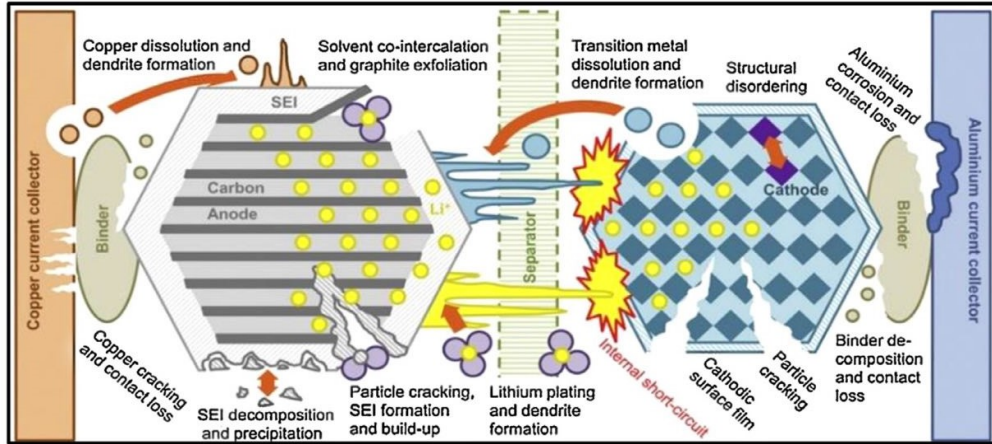


Figure 19: Result of heat generation on Li-ion cell [13].

thermal runaway, with eventual smoke, emissions, fire and decomposition of electrolyte and electrode material (Figure 20). The phenomena of thermal runaway can be experienced above 300°C and is comparable to an internal combustion engine, where can be observed an initial slow temperature increase, followed by a really steep raise, due high reaction rates [131].

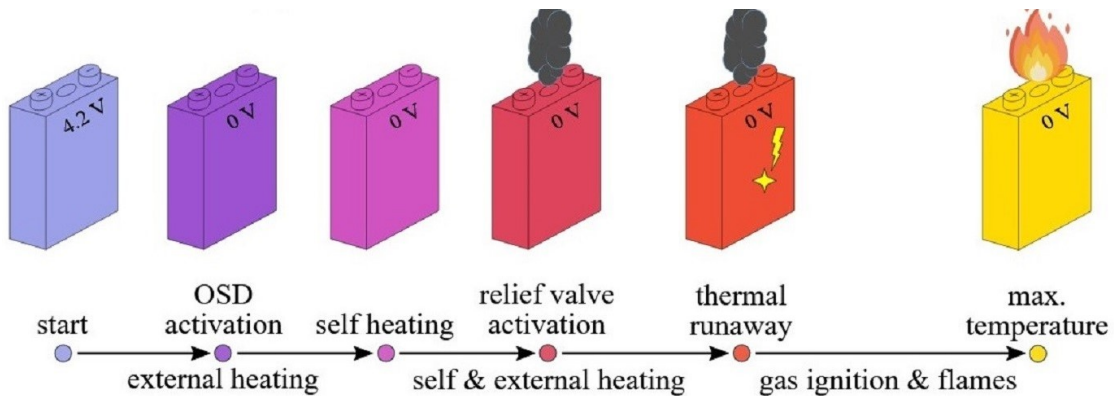


Figure 20: Thermal runaway process [92].

2.3 Cooling system types

As mentioned in the previous section, the untreated heat can induce dramatic and dangerous temperature increase. Consequently, it is necessary a precise and deep control of heat dissipation mechanisms within the battery. Such role is carried out by the thermal management system, which, by means of an accurately designed cooling system, must maintain the pack at an optimum average temperature and with even temperature distribution, as identified by the vehicle manufacturer. Pack thermal management system must be also compact, lightweight, low cost, easily

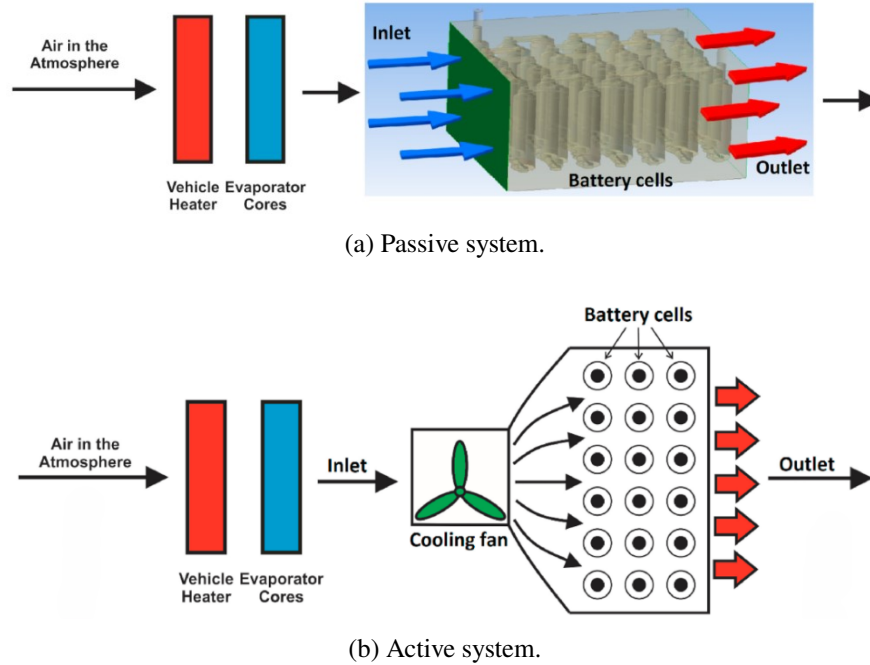


Figure 21: Air cooling systems [32].

packaged and absolutely reliable [103]. Several cooling strategies/methods have been proposed for lithium ion batteries, but they can be summarized into three typologies.

2.3.1 Air cooling

Air cooling is the most widely used heat dissipation method for battery packs, by directly using natural convection or by generating forced airflow through a fan operation. Natural convection (Figure 21a) has the obvious advantage of simplicity and low cost, while it has the disadvantage of weak dissipation capacity, effective for low C-rates (generally up to 0.5C in both charging and discharging [129]). With the rise in C-rate, current increases quickly and correspondingly heat generation within the battery cell, requiring forced convection by a fan (Figure 21b). This method is more reliable and easier to maintain than the natural convection, which is highly dependent on conditions of the surrounding air. In any case, both systems are influenced by factors like cross-section area, temperature of the inlet air, direction of the flow, position of the blower, structure, cell spacing discharge rate, etc [71] [24]. However, a common problem for both systems is temperature non-uniformity within the battery, with higher values for cells collocated in the interior of the pack structure due to mutual heating [105].

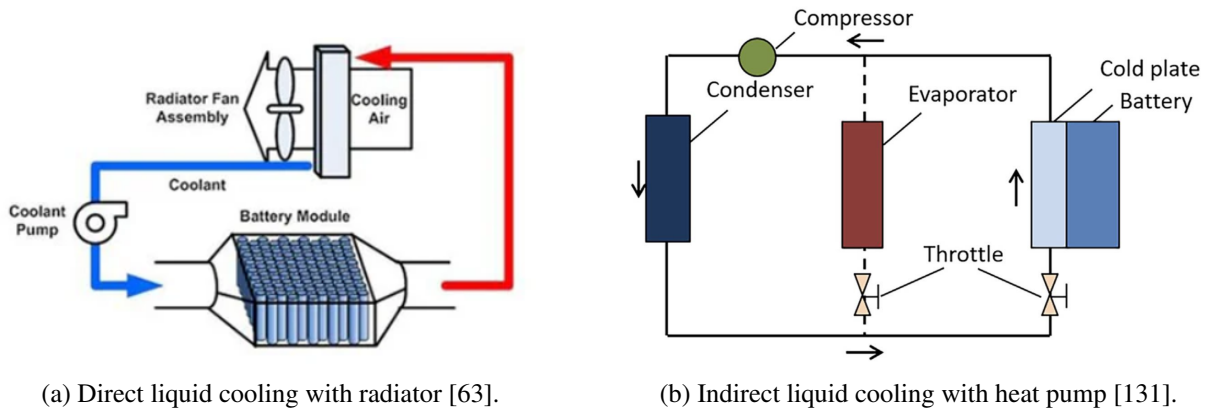


Figure 22: Liquid cooling systems.

2.3.2 Liquid cooling

Compared with air cooling, liquid cooling is more efficient due to higher heat transfer coefficient of the coolant (which is commonly a blend of water and glycol). Liquid cooling can be classified into direct and indirect cooling. The first type (Figure 22a), commonly liquid immersion cooling, can cool the entire battery surface, greatly contributing to temperature uniformity of LIBs. However, high requirements on the waterproof performance of battery system, and the risk of short circuit and electrochemical reactions makes the employment of this system particularly challenging. Indirect liquid cooling (Figure 22b) has several different declensions depending on design of the pack: tube cooling, cold plate cooling with micro/macro channels, jacket cooling, ect. In any case, all of these systems are easier implementable, safer and realized to be compact and light, even if they present lower cooling capacity [131]. The cooling capacity in these techniques is mainly influenced by channel height and width (less impacting factors), number of channels, and flow rate and temperature of coolant through the channels (more impacting factors) [25]. The temperature of the coolant can be regulated by means of a classical radiator (which is able to maintain the coolant at ambient temperature) or by means of a more advanced and effective heat pump (capable of decreasing the coolant temperature also at lower temperatures for highly demanding thermal conditions).

2.3.3 PCM (Phase change material) cooling

The PCM system (Figure 23) exploits the change of phase property to absorb excess latent heat generated during battery operation, maintaining it at relatively constant temperature within its operating range. During periods of low or no operation, when

the battery is not generating much heat, the PCM changes phase again, releasing the stored latent heat. The classification of PCM can be done in four categories based on phase-change type: solid-solid, solid-liquid, solid-gas and liquid-gas [25]. Surely this system offer the advantage of not requiring extra energy for its functioning, however it presents limited heat absorption capacity (which could result insufficient for high-demand situations or rapid temperature increase) and high design complexity as well as additional weight and size of the system.

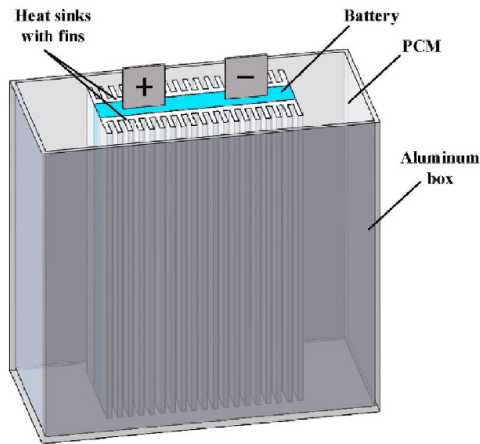


Figure 23: PCM cooling [21].

2.4 Aging phenomena

As mentioned in sections 1.2 and 1.3, the battery protagonist of this thesis study will be a sort of "black box", with really limited information (mainly related to nominal characteristic of the cell) and no knowledge about its first usage life. This is certainly an aspect to not underestimate, since Lithium-ion batteries are subjected to important aging phenomena, which can drastically change the cell behaviour, resulting not only in capacity fade and power loss, but also in the variation of other parameters, moving them away from design conditions and altering the normal functioning of the battery. Consequently, it is fundamental to have a clear vision on all the aging mechanisms acting on the cell during its first life.

2.4.1 Degradation modes

The deterioration of LIBs is often categorized into two modalities of analysis: loss of active lithium inventory (LLI) and loss of positive and negative active materials (LAM_{NE}/LAM_{PE}):

- **Loss of Lithium Inventory (LLI):** This occurs when the amount of cyclable lithium decreases due to SEI layer growth and lithium deposition reactions. During battery formation, Li^+ ions are consumed to form a dense SEI film, which can grow over time and crack during lithium ion insertion and extraction, leading to further loss of Li^+ ions. Batteries with a low N/P ratio or those subjected to extreme charging conditions are prone to lithium plating reactions, where Li^+ ions deposit as lithium metal, increasing cell polarization and hindering the intercalation process.
- **Loss of Active Material (LAM):** This involves the mechanical destruction of electrode particles and changes in their crystal structure. Solvent cointercalation and gas evolution can cause graphite particle exfoliation and cracking, leading to rapid electrode degradation. High C-rates and high states of charge can create significant Li^+ ion concentration gradients, causing mechanical strain and fractures. Nickel-rich cathodes, like NMCs, are prone to instability, which reduces battery life and thermal stability. High potentials and temperatures can dissolve transition metal ions (Ni, Co, Mn), altering the electrode composition and crystal structure, reducing the number of available host structures for Li^+ ion intercalation and decreasing cathode capacity [28].

Both degradation modes primarily result from the regular cycles of charge and discharge inherent to the cell's operation, making them unavoidable. The literature presents several models that aim to accurately predict aging phenomena and capacity fade, such as those proposed by Ding et al.[28], Li et al. [79], and Lopetegi et al. [82]. However, this area of research remains in its early stages due to the complex interplay between utilization patterns and boundary conditions. Consequently, for this thesis, and particularly for selecting second-life applications, the aging phenomena associated with the normal functioning of the cell will not be considered. Instead, the focus will shift to external factors influencing the aging.

2.4.2 External factors

With the diversification of LIBs application and usage scenarios, the operating conditions they encounter can vary significantly, profoundly affecting cell aging if not properly managed. External factors are crucial when considering second-life scenarios because they are the only aspects that, kept under control, can potentially preserve battery life. Therefore, it is essential to identify and understand these external factors that drive aging phenomena.

They can be categorized into four types:

- **Temperature:** lithium-ion batteries are characterized by an ideal working temperature range, operations below or beyond this range would hasten battery aging. At low temperatures, the electrolyte and SEI conductivity decreases, deteriorating the Li^+ charge transfer kinetics and intercalation into graphite layer, resulting in the formation of large Li^+ concentration gradient in the solid phase, which initiates lithium plating reactions. On the contrary, temperature increase during cycling highly amplifies electrolyte decomposition and anodic SEI film growth (beyond of the phenomena already explained in section 2.2).
- **SOC operating interval:** after prolonged cycling in a wide SOC range, numerous microcracks were observed in the cathode particles, followed by crystal structure transformation into a rock-salt-like structure, resulting in an increase in charge transfer resistance [28]. Furthermore the cells can be over charged or discharged (due to improper managing or manufacture inaccuracies), causing LAM and copper current collector dissolution, respectively.
- **Charge-Discharge rate:** for extreme fast charging, lithium plating is the most important battery degradation phenomena, followed by severe crystal structure disruption and interfacial reactions. Furthermore, high current rates, not only produce heat with the above mentioned consequences but cause also diffusion stresses within the cell and drastic volume changes of the electrode particles, raising internal impedance. In general, high charging currents effects battery cycle life more than high discharge currents.
- **Mechanical stress:** under conditions of unconstrained expansion or excessively low external pressure, battery components may delaminate, severely reducing battery capacity. In contrast, excess pressure could cause the separator pores to close and impede ion transport, resulting in high localized current densities and accelerating the cell's inhomogeneous degradation [28].

Figure 24 provide a graphical representation of all the aging mechanisms acting on a battery cell. In the assessment and design of a second-life application for a battery pack, it is essential to consider the aforementioned external factors. Among these, temperature management is particularly crucial and forms the central focus of this thesis. However, this study will specifically address the management of higher temperatures, including cooling strategies, while the challenges associated with charging and discharging at extremely low temperatures (and the necessary heating) will remain areas for future investigation.

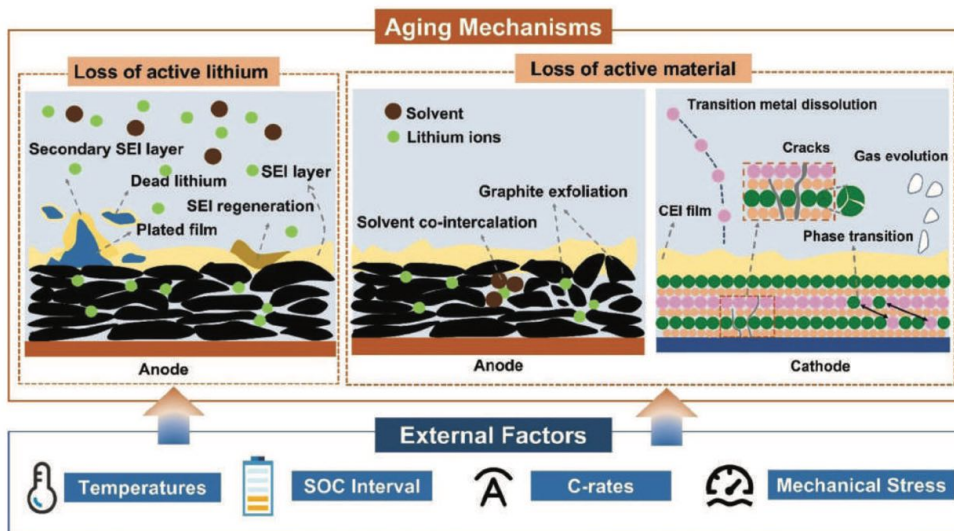


Figure 24: Graphical representation of relationship LIBs degradation modes and external factors [28]. The relationship between battery degradation modes, aging mechanisms, and external factors is illustrated. SEI film growth and irreversible lithium plating would result in LLI; particle cracking and exfoliation of active material, phase transition, gas generation, and transition metal dissolution would result in both positive and negative LAM. External factors include temperature, operating SOC, C-rates, and mechanical stress.

The SOC control is a delicate issue since most second-life applications cannot operate effectively within a limited discharge range. Imposing second-life scenarios that work with narrow range of SOC would in fact be highly restrictive. A potential solution could be the employment of an appropriate battery management system to manage and prevent the battery from reaching its limits.

In contrast, the discharge rate can be effectively controlled with a careful redesign of the new pack configuration in the second-life application. Limiting the maximum discharge rate to 1C, as this project proposes, will help to preserve the battery's capacity by reducing degradation caused by high current. Additionally, it will minimize heat production, which occurs at higher current rates.

Finally, mechanical integrity is strictly related to the configuration and arrangement of the pack in the second-life application, as will be discussed in section 2.8.2. The closer the battery remains to its original design conditions, the greater the likelihood of preserving the pack's integrity. Ensuring the correct spatial arrangement and mechanical stability of the pack in all operating conditions is fundamental to the success of second-life applications.

2.5 First life of the battery pack

The scope of this section is to give more details about the battery subject of this thesis. In particular are included, not only numerical data and properties, but also the first usage environment of the pack. As previously mentioned, the battery first life is a crucial aspect to not underestimate for the evaluation of the performance of the pack, in sight of a possible second usage scenario.

The used module was extracted from the battery pack of the HONDA CLARITY PLUG-IN HYBRID 2018, a midsize sedan. All the following information are taken from [125].

The powertrain of the vehicle (depicted in Figure 25) was constituted by drive motor, generator, engine and PCU which were positioned in the front of the vehicle while the IPU was positioned under the floor.

The presence of the electric powertrain allowed the vehicle to perform different driving modes depending on the vehicle energy demand and SOC of the battery:

- EV Driving Mode, in which the motor is driven by battery power.
- HV Driving Mode, in which both engine-generated power and battery power are used.
- Engine Driving Mode, in which both engine power (via the connection to the clutch) and motor power are used.

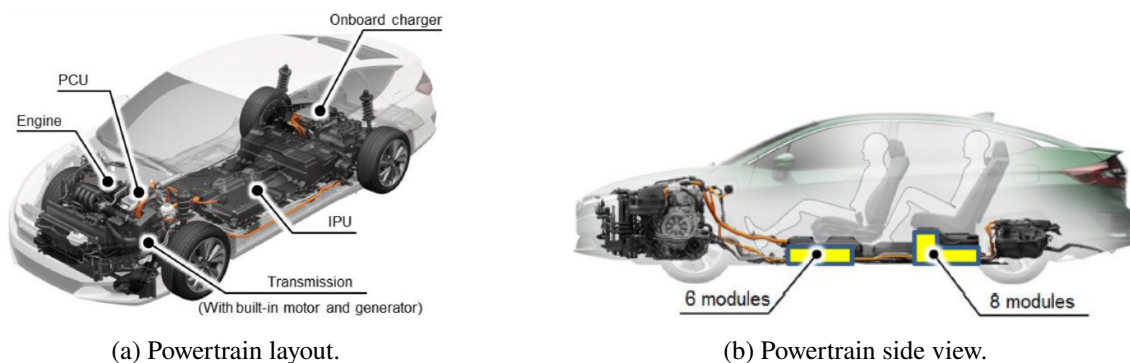


Figure 25: HONDA CLARITY PHEV [125].

In Figure 26 is represented a typical battery SOC profile for a PHEV. The vehicle operates as an EV when there is a high SOC, resulting in charge-depleting (CD) operation. When the SOC falls under a minimum threshold, the system switches to charge-sustaining (CS) operation, in which the powertrain operates to maintain the SOC in a certain window (especially by using the internal combustion engine).

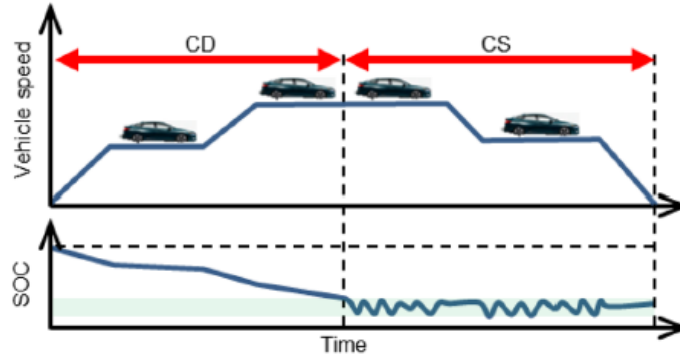
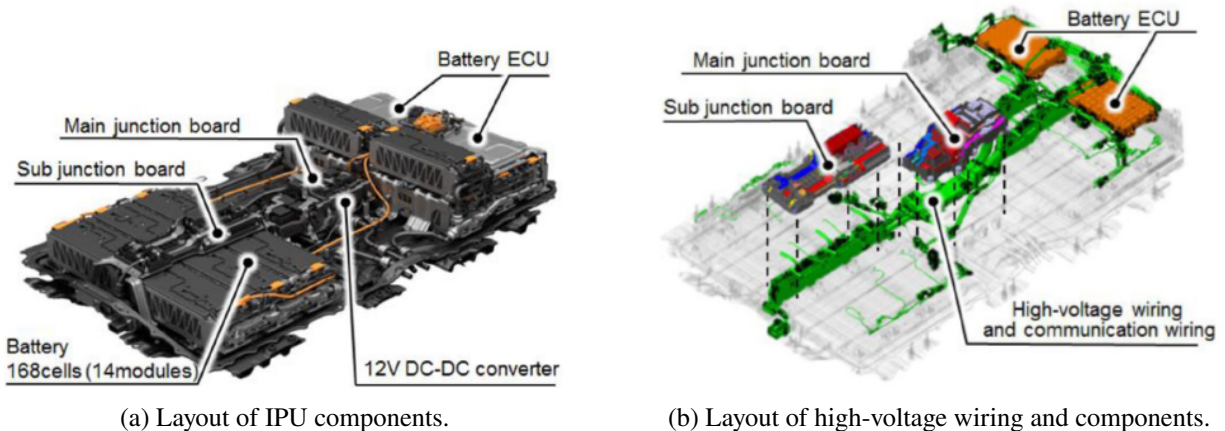


Figure 26: Typical battery SOC profile for a PHEV [125].

Figure 27a shows the position of the IPU in the vehicle. In order to offer adequate leg room in front and rear seats, and allow for rear seat trunk access, the battery modules were divided and positioned under the front and rear seats. Figure 27b shows the layout of the high-voltage wiring and components in the IPU. The high-voltage wiring and communications wiring were concentrated in the centre of the IPU between the battery modules, allowing for an integrated configuration.



(a) Layout of IPU components.

(b) Layout of high-voltage wiring and components.

Item	Unit	CLARITY PLUG-IN HYBRID
Capacity	kWh	17.0
Rated voltage	V	310.8
Cell (module)	-	168(14)
Cooling system	-	Coolant-cooled
Position	-	Under-floor

(c) IPU specifications.

Figure 27: IPU Technologies [125].

Figure 27c shows the pack IPU specifications: the battery pack was characterized

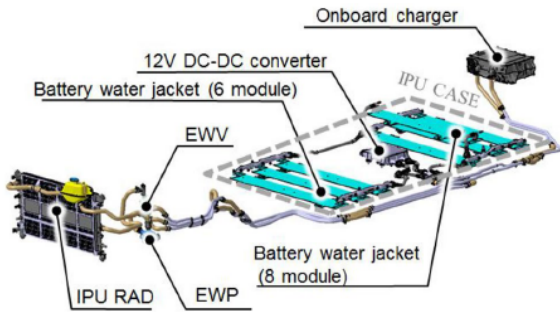
Table 2: Cell specifications [125].

Item	Unit	Value
Type	[-]	Lithium-Ion
Format	[-]	Prismatic
Nominal capacity	[Ah]	27
Nominal voltage	[V]	3.7
Voltage limits	[V]	2.5 / 4.2
Cathode material	[-]	NMC (Nickel Manganese Cobalt Oxide)
Anode material	[-]	Graphite
Arrangement	[-]	Flat wound cell
Packaging material	[-]	Metal can (aluminum)
Current	[A]	continuous 209 / peak 250
Current range	[A]	-465 discharge / 116 charge (-16C / 4C)
Energy	[Wh]	at C/10 103.8
Energy density (gravimetric)	[Wh/kg]	144
Energy density (volumetric)	[Wh/l]	282
Power	[W]	continuous 718 / peak 862
Power density (gravimetric)	[kW/kg]	1.19
Power density (volumetric)	[kW/l]	2.35
Temperature limits	[°C]	-20 / 60
Weight	[g]	722.0
Dimension	[mm]	148.5 x 90.9 x 27.2

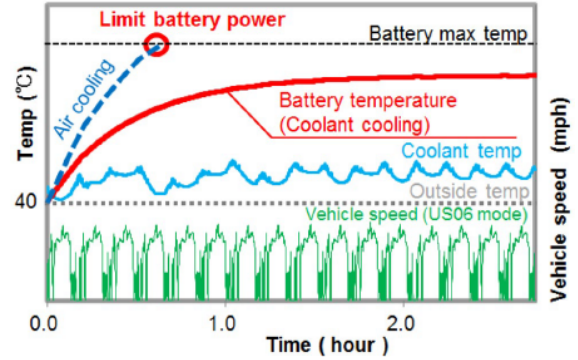
by 14 modules and 168 cells (12 cells for each module) with a 84s-2p configuration (84 in series and 2 in parallel). This arrangement allowed to obtain 17.0 kWh of capacity and 310.8 V of rated voltage.

In Table 2 are reported the specifications of the battery cells [125] [51].

For this kind of vehicle the cooling system was selected taking into consideration the amount of heat generated by the battery and the volume of the cooling system itself. Being a PHEV, the effort required to the battery system was comparable to a BEV, with a quite high heat generated by each cell. The bottom of the module was coolant-cooled by means of a cooling plate, realizing 3.5 times higher cooling performance than an air cooling system. Figure 28b shows changes in battery temperature in a high-temperature environment. The adoption of the coolant-cooling system helped to avoid limiting vehicle's driving performance due to high battery temperatures, even during high-load operation, like the US06 mode in a high-temperature environment.



(a) Components of IPU cooling circuit.



(b) Battery temperature during high-load operation.

Item	Unit	CLARITY PLUG-IN HYBRID
Dimensions	mm	1787/1076/315
Battery energy	kWh	17.0
Number of cells	-	168
Cooling system	-	Coolant-cooled
Cooling performance	W*	665

(c) Battery cooling performance.

Figure 28: IPU Cooling system [125].

2.6 Battery Models

In this study is imperative to evaluate thermal performance of cells encompassed in a module originally designed and employed in PHEVs, in order to choose an appropriate second life scenario. However, predicting the behavior of a battery is a complex task, as evidenced by Alipour et al. [5] and Barcellona et al. [11], which revealed substantial variability in Battery Energy Storage Systems (BESSs), especially when repurposed for applications beyond their intended first-life use.

Manufacturer-provided nominal data, typically found in data sheets, often proves insufficient and fails to accurately represent real-world battery behaviour, especially post the first complete cycle life. Metrics like power density, energy density, efficiency, and lifetime are influenced by diverse factors, including temperature, current profile, SOC, and Depth of Discharge (DoD).

Attempting to experimentally map out battery performance in all conceivable conditions is impractical due to the associated costs and time constraints. Given these challenges, precise battery modelling becomes crucial for this thesis.

A model is simply an abstract representation of an object or system. For batteries, these models usually take the form of mathematical equations, together

with appropriate boundary conditions [17]. Battery modelling operates at different technological levels:

1. Materials Level, investigating the individual electrodes/electrolyte structures and materials.
2. Cell Level, describing the fundamental element of any BESS as observed at its terminals.
3. Module Level, modeling the assembly of several cells along with the BMS as the primary unit within the BESS.
4. System Level, modeling the complete stack of modules, including the battery inverter [15].

For the purposes of this thesis, at least a system-level approach is deemed appropriate, as only one module from the Honda Clarity is available (Figure 7b). The module level approach is unsuitable due to the absence of the BMS and the need for a deep understanding of the functioning and performance of individual cells before forming the module.

The subsequent sections provide a concise literature review on battery modelling approaches, from the cell to material level.

2.6.1 Data-driven model (DDM)

Data-driven model (DDM) (Figure 29a) utilizes computational intelligence to approximate highly nonlinear battery characteristics, resulting in notably efficiency, but heavily dependent on data quantity and training methods. Various data-driven models describe batteries behaviour without prior knowledge of the internal structure:

- Artificial Neural Network (ANN): A powerful tool for modelling nonlinear functions with proper data training, demanding large quantities of high-quality data and ample training time for accuracy.
- Adaptive Neuro-Fuzzy Inference Systems (ANFIS): Combining flexibility, subjectivity, and learning capability, but its accuracy varies with the number and quality of rules.
- Deep Neural Network (DNN) and Feed Forward Neural Network (FFNN): Simple learning processes, non-intensive, and efficient computation, but they are one-way models, not considering data history, requiring offline training.

- Support Vector Machine (SVM): Computationally expensive and struggles with large data, making it challenging for SOC and SOH estimation.

Several examples are present in literature, where the use of such kind of model is really widespread.

Boujoundar et al. [14] proposed the SOC estimator system for Li-Ion batteries using ANN trained off-line. The simulation results showed good accuracy to the experimental data, for all different environmental conditions. Clearly the database used in the design of this model needed to contain all the possible operation scenarios. Khumprom et al. [74] presented the benchmark of data-driven model using machine learning for battery prognostic data. The study claimed success in aiding the benchmarking an real-time applicability, however interpretability challenge and computational time drawbacks of deep learning algorithms were not mentioned. Chemali et al. [22] used DNN for battery SOC estimation where battery measurements are directly mapped to SOC. The result was an accurate estimation, but obtained with large number of tests data, requiring huge economical and temporal resources.

The cited papers and all the above-mentioned models share a common limitation: wide data collection is crucial for model development, necessitating large amount of training data. Unbalanced data would cause model overfitting and underfitting in decision-making [83]. However, data collection is time-consuming and costly, making it challenging to implement in research fields [2]. Hence, the adoption of such battery modelling approaches in this thesis would be unpractical, considering the time-consuming and costly processes that cannot be afforded.

2.6.2 Bucket model

The primary benefit of the bucket model (Figure 29b) lies in its straightforward implementation. The SOC serves as an indicator of the energy state, with the control input being the power for battery charging and discharging, rather than the battery current. Consequently, the model associated with it is solely linked to the battery power or Ampere-hour throughput. The parameters requiring identification include the initial energy state and the coefficient corresponding to the equivalent operating cycles.

Consequently, in terms of accuracy when compared to other models, the bucket model exhibits the least favourable performance as expressed by Shuangqi et al. [79] and Balogun et al. [9]: it severely ignores the dynamics, operating voltage limits, and relaxation times of the battery. The lack of consideration for the voltage limits

can significantly overestimate the power delivery capability of the battery, leading to sub-optimal control trajectories, which can only be mitigated by expensively over-sizing the battery system. As a consequence, the bucket model generally finds application in offering a rudimentary assessment of the viability of secondary energy storage applications [64].

Therefore, it is clear why this approach could not be used for BESS modeling in this thesis.

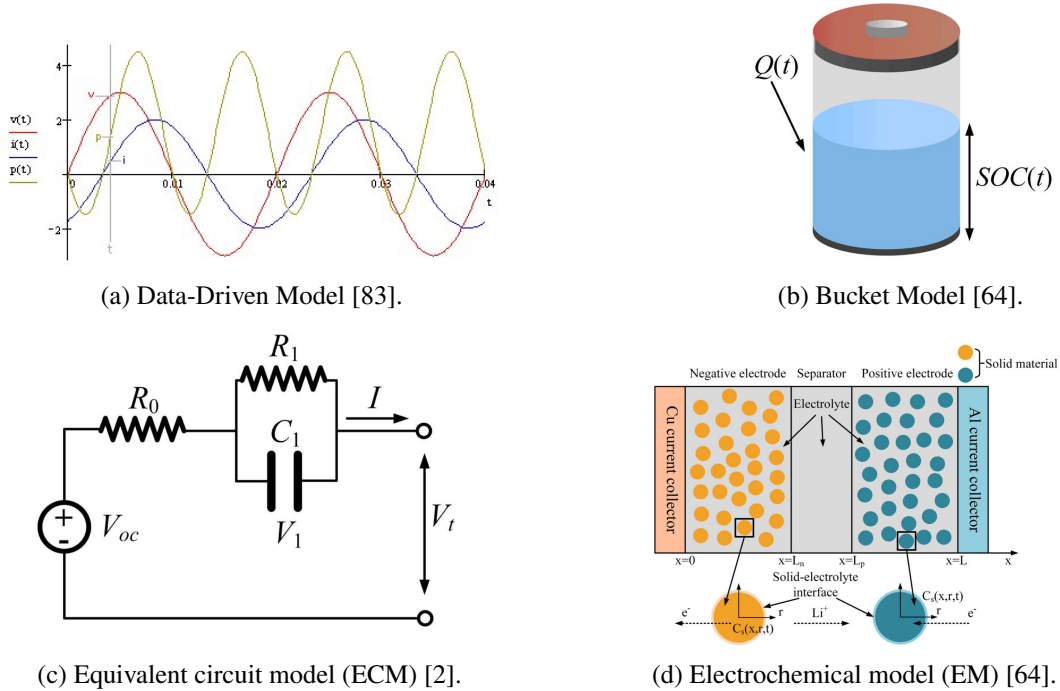


Figure 29: Battery modelling types

2.6.3 Equivalent circuit model (ECM)

The Equivalent Circuit Model (ECM) (Figure 29c) employs electrical components, such as a voltage source, resistors, and capacitors, to characterize the internal dynamics of a cell or battery. This model falls under the category of empirical models, addressing the external characteristics of the cell and it is built by fitting data of specific experiments [64].

The simplest ECM is the Rint model, conceptualizing the battery as a voltage source with series resistance. While straightforward in implementation, this model fails to accurately represent the characteristics of batteries used in EVs. Consequently, one or more resistance-capacitance (RC) parallel networks are

introduced to the Rint model, resulting in a Thevenin model.

Among the various ECM models found in the literature, RC network-based models are widely acknowledged for online applications and aging modeling. Since batteries exhibit nonlinear behavior, their dynamics vary under different operating conditions, such as SOC, temperature, and charging and discharging rates. The control inputs in this scenario are the battery charging and discharging currents. Consequently, the parametrization of the model is viewed as an "identification problem" or an "optimization problem" to align the model with measured data [2].

Liaw et al. [81] used a simple ECM to show that, with a sufficient amount of data collected and a acceptable understanding of the battery degradation process, it was possible to develop a highly reliable battery performance model to predict either calendar or cycle life. Mroz et al. [97] focused on health monitoring for predicting the lifetime of LIBs using a 2RC ECM. The model incorporated thermal influences and aging functions derived from experimental measurements. However, the determination of aging influence may lack accuracy for simulations outside the standard range, raising concerns about validation reliability. Bruch et al. [18] presented a fitting procedure for the identification of ECM parameters: it closely matched the relaxation after a pulse, deviating only by around 0.08 mV. Despite its advantages in aging studies, the model struggled to detect the high-frequency SEI growth, a crucial aspect of a cell's lifetime.

It is unquestionable that ECMs offer several advantages in battery modelling, especially for ease of implementation and use in online applications, with a corresponding high accuracy. However, since entirely based on phenomenological and non physical aspects, they cannot ensure reliability in untrained and unexplored working conditions, or be relied upon to predict long-term battery behaviour. [17].

2.6.4 Electrochemical model (EM)

In comparison to earlier models, the accuracy of electrochemical battery models (Figure 29d) is notably superior, primarily attributed to their reliance on physics-based modeling principles [64]. These models intricately characterize battery behaviour by considering factors such as electrolyte concentration, electrode sizes (both anode and cathode), transport phenomena, electrochemical kinetics, and thermal/stress/mechanical effects, employing partial differential equations (PDEs). Despite the EM delivering precise insights into battery performance, it demands substantial computational power and time to determine a multitude of parameters. Additionally, its implementation in real-time applications proves to be a challenging

endeavor [2].

Table 3: Battery models summary.

Model	Strengths	Weaknesses
Data-driven model (DDM)	<ul style="list-style-type: none"> • High nonlinear prediction capability. • Easy to implement. • Suitable for online applications. 	<ul style="list-style-type: none"> • High computational complexity. • Accuracy fully dependent on quality of training data. • Need high storage.
Bucket model	<ul style="list-style-type: none"> • Simplicity. • Minimum parameters required. 	<ul style="list-style-type: none"> • Minimum accuracy. • Ignores dynamics and relaxation times.
Equivalent circuit model (ECM)	<ul style="list-style-type: none"> • Moderate accuracy and complexity. • Able to identify parameters online. 	<ul style="list-style-type: none"> • Lack in describing internal cell phenomena. • Reliability not ensured in untested conditions.
Electrochemical model (EM)	<ul style="list-style-type: none"> • Highest accuracy. • Clear physical interpretation. 	<ul style="list-style-type: none"> • High nonlinearity and complexity. • Difficulty in parameter identification. • Difficult to apply online.

2.6.5 Modelling approach

After this short review, in order to decide a modelling approach compliant with the objectives of this thesis, it is fundamental to analyze which are requirements and available resources. They are listed as follows:

1. Limited time and resources, with the possibility of testing the cell only at two temperatures.

2. Required understanding of the physical phenomena within the cell.
3. Required deep knowledge of the battery in all the operating conditions.
4. High accuracy/fidelity of the model.
5. Off-line implementation.

From the previous review and carefully looking at the requirements/characteristics of the thesis, the chosen model is the electrochemical one. Indeed, Thiruvonasundari et al. [118] have demonstrated that electrochemical is the correct model to use in case a complete battery diagnosis is required.

Condition 1 clearly underlines the impossibility of using DDM in this thesis. Even if this model leads to decent levels of accuracy, data collection is crucial for model development, necessitating large amounts of training data obtained with time-consuming and costly processes. Hence the adoption of such battery modelling approaches is necessarily precluded.

As matter of fact EM is the only one capable of ensuring the satisfaction of conditions 2 and 3.

For what concerns requirement 4, there are several examples in literature in which the superiority of the EM is proven over both bucket model and ECM. Reniers et al. [108] have compared their accuracy on a Kokam 16 Ah NMC cell. The result was that the bucket model, only based on energy throughput and maximum power level, did not represent correctly the battery behaviour due absence of temperature dependency. The ECM, tested in limited boundary conditions, could not adequately predict the battery conduct. This clearly illustrated that empirical correlations are valid only for tested operating conditions. The predictions of electrochemical model, based on SEI-growth model coupled with single particle model, were decent but not fully accurate (this is the reason why in this thesis will be used a more complex model, see section 2.7.6). However, the major trends were better predicted than the other two models.

In a lithium-ion battery modelling overview, Meng et al. [91] demonstrated that, after the optimization of parameters for each model, the most accurate model was the EM, with better accuracy but also higher execution time. However, requirement 5 clearly elucidates the unnecessary on-line elaboration of the model, hence this is not a crucial disadvantage.

2.7 Overview of electrochemical models

The objective of this section is to give a brief overview of the existing electrochemical models, with all their peculiarities, advantages and drawbacks. This part is crucial for the choice of the proper approach to use for battery modelling. A very complete explanation about the electrochemical modelling is presented by Brosa [17], of which here is just reported a summary for the scope of this thesis study.

2.7.1 Single particle model (SPM)

The SPM represents the simplest among the electrochemical's. It encompasses three fundamental physical phenomena: transport of lithium within the particles, thermodynamic relationship linking lithium concentration and electrode potential, and overpotential necessary to drive lithium intercalation reactions. The terminal voltage excludes any contributions from the electrolyte or Ohmic losses in the electrodes, which are generally negligible when the cell operates at a low current.

When implemented numerically, the SPM's complexity aligns with that of ECMs. The simplicity of the SPM is evident not only in its numerical implementation but also in the minimal number of parameters needed for the characterization. Apart from the physical constants and the model inputs, only 17 parameters are required to fully describe the model: 8 for each electrode and one for the battery temperature. No electrolyte parameters are necessary.

Despite being a very useful and widely used model, SPM does not capture the effects of the electrolyte which becomes crucial for increased C-rates. In order to incorporate it, is necessary, at the very least, to consider the SPMe.

2.7.2 Single particle model with electrolyte (SPMe)

The SPM exhibits high performance at low C-rates, but its accuracy diminishes as the C-rate increases. To enhance the accuracy, the model is refined by introducing electrolyte dynamics, resulting in the creation of the SPMe. This model preserves much of the simplicity of the SPM, maintaining its one-dimensional spatial nature, while significantly improving performance (graphical model representation at Figure 30). The key concept involves solving PDEs for ion concentration in the electrolyte, in addition to the particle equations from the SPM. The electrolyte concentration enables the calculation of additional terms in the voltage expression, enhancing accuracy.

The SPMe's complexity is slightly higher than that of the SPM. Besides the PDEs for each particle, an additional quasi-linear PDE for electrolyte ion concentration

must be solved. However, the three spatially one-dimensional PDEs are decoupled, allowing for efficient solutions. This model necessitates of 30 parameters: 9 for each electrode, 11 for the electrolyte, and the battery temperature.

While SPMe models exhibit strong agreement with more complex models like the Doyle-Fuller-Newman model across various operating conditions, they do not capture the spatial distribution of lithium concentration across each electrode. Spatial variations become significant for materials like LiFePO_4 , with flat open-circuit potential curves. For materials like NMC, with a notable gradient in their open-circuit potential curve, particles across the electrode maintain nearly identical surface lithium-ion concentrations and discharge at nearly the same rate.

Several examples are present in literature that allow to demonstrate the absolute validity of this model. For an advanced BMS, Pozzi et al. [104] presented a comparison between an isothermal SPMe and standard identification profiles like CC and multistep discharging approaches. Results demonstrated that SPMe with optimal experimental design parameters identification methodology outperforms standard approaches in convergence time and accuracy. Lopetegi et al. [82] proposed a comparison between the P2D model and SPMe for battery aging prediction. The results showed that SPMe could predict capacity fade very accurately compared to the P2D model, but with a reduced computational cost. However, some internal variables cannot be modeled as accurately as with the P2D model, due to the single particle modeling. Guo et al. [35] conducted a constant current discharge experiment in order to evaluate the effectiveness of a SPMe combined with many-particle mesoscopic model. The root mean square errors (RMSE) between simulation and test results were showcasing a way better accuracy compared to other models, with the model meeting the accuracy requirements also across different discharging frequencies.

An evident weakness of the SPMe model emerges when the current becomes large enough to induce electrolyte depletion, leading to breakdowns in agreement with the DFN model. To address such effects, particularly at high C-rates involving electrolyte depletion or when incorporating degradation effects, the DFN model is necessary.

2.7.3 Doyle–Fuller–Newman (DFN) model

The DFN model, when appropriately parameterized, is capable of encapsulating essential features, making it applicable across a broad spectrum of operating

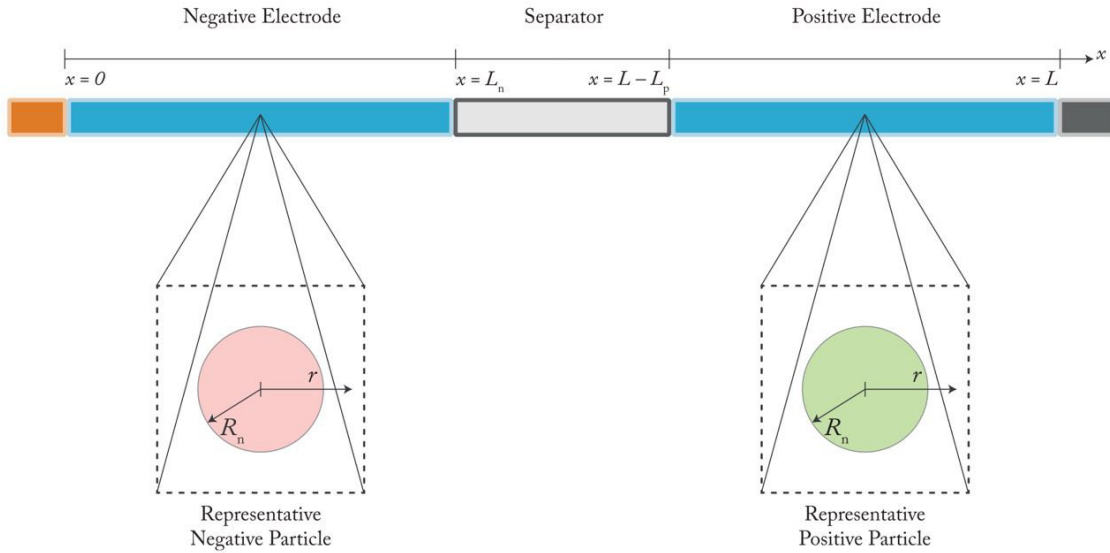


Figure 30: Sketch of the geometry of the SPMe model. There is only a single representative particle at each electrode, rather than infinitely many [17].

conditions and demonstrating remarkable accuracy in predicting experimental outcomes. Even if higher in complexity compared to SPM and SPMe, DFN model remains computationally feasible.

In contrast to the SPMe's, the DFN model incorporates electrode particles across the entire width of the electrodes, referring it as a P2D model. This inclusion enables an accurate modeling of the spatial distribution of lithium across the electrodes, a pivotal role in modeling non-homogeneous interfacial current density, leading to non-uniform degradation of the electrodes (graphical model representation at Figure 31). Despite sharing the same physics as the SPMe, the DFN model requires an equivalent number of parameters.

This kind of model is particularly widespread in literature and research field for its good balance between complexity and computational time. Castle et al. [20] proposed a DFN model for nano-structured lithium iron phosphate (LFP) cathodes, assuming fast transport within small particles. Numerical solutions reveal localized (de)intercalation regions propagating in LFP electrodes, especially compared to other cathode materials like NMC. Krachkovskiy et al. [77] proposed a combined magnetic and nuclear methodology which enabled real time visualization of lithiation/delithiation processes during operations, by means of DFN modeling techniques. The results demonstrated that polarization of the thick graphite electrode is correlated with appearance of energy barriers and resulting significant reduction of the lithium chemical diffusion, which must be addressed in any attempt at the fast

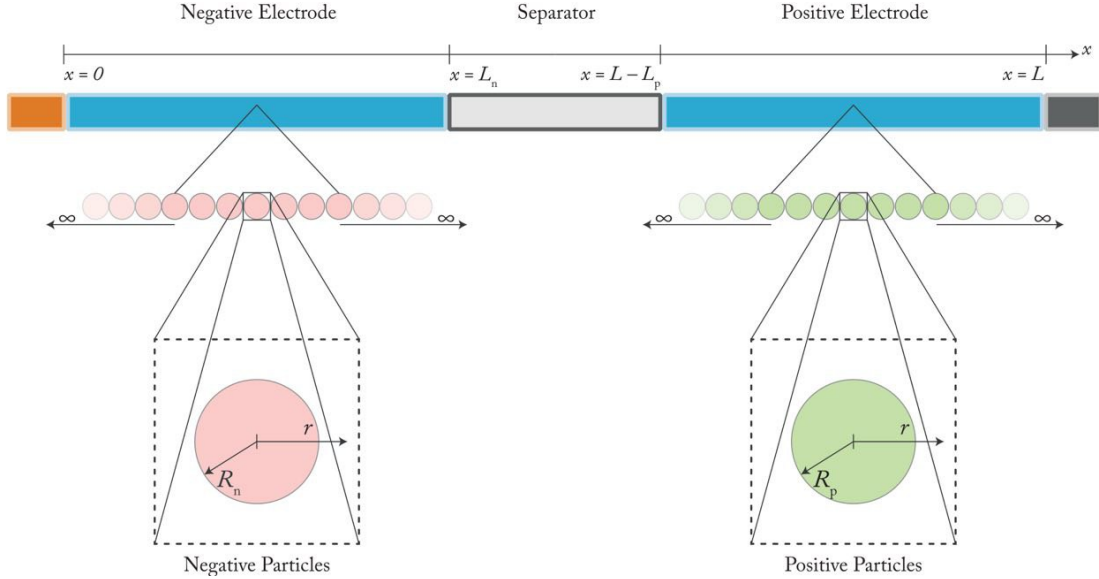


Figure 31: Sketch of the geometry of DFN model [17]. Electrodes and separator are one-dimensional domains, defined to be $x \in [0, L_n]$ for negative electrode, $x \in [L_n, L - L_p]$ for the separator and $x \in [L - L_p, L]$ for the positive electrode. The microstructure is assumed to be composed of isolated spherical particles with domains $r \in [0, R_k]$ for $k \in \{n, p\}$.

charging of Li-ion batteries. Zulke et al. [133] showed that a carefully parametrised DFN model is capable of accurately predicting the behaviour of a cell for both galvanostatic and drive cycles in a wide variety of situations. The model was also used to accurately compute the irreversible energy losses occurring within the cell, for different discharge patterns, and infer their location.

In summary, the DFN model is highly popular and effective, but it confines its consideration to a one-dimensional problem at the cell and particle scales. As a result, it does not encompass effects associated with non-spherical particles or the true three-dimensional geometry of the cell. To address these aspects, a more comprehensive homogenized model is necessary.

2.7.4 Homogenised model

Homogenized models can be viewed as an extension of the DFN model, with the employment of arbitrary and homogenized geometries for the porous electrodes, potentially reaching up to 3 + 3D (i.e., three dimensions at both the cell and particle levels). To simulate the homogenized model, apart from specifying parameters, the geometry of the cell and a representative microstructure must be provided. This geometry replaces certain model parameters, such as particle radius and electrode thicknesses. The complexity of the homogenized model surpasses that of the DFN

model due to the increased number of spatial dimensions and the intricate geometry (graphical model representation at Figure 32).

Several challenges arise in the homogenized model. Firstly, the computation of effective transport properties is a crucial issue: homogenized model must be calculated from imaging data or idealized geometries, introducing additional complexities. Another concern is the unclear separation of scales in a typical porous electrode geometry: this separation is not always evident in real batteries, potentially questioning the accuracy of estimated parameters. Furthermore, the homogenized model introduces new states, such as non-symmetric lithium distribution within particles, that cannot be directly observed, making the validation of many model outputs challenging.

Hunt et al. [66] proposed a thermal-electrochemical homogenized modelling for behaviour of porous electrodes. Using asymptotic homogenization and including thermal and capacitance effects, the model allowed simulation of complex microstructures. Compared to the DFN model, it was more versatile with capability of deriving mesoscopic parameters directly from microscopic properties, but clearly with improved complexity.

While homogenized models allows for the inclusion of effects arising from the complex geometry of a real cell that cannot be adequately addressed by the DFN model, they fall short of fully resolving a real geometry. To address this limitation, the consideration of a high-fidelity microscale model becomes imperative.

2.7.5 Microscale model

The high-fidelity microscale model represents the most intricate and realistic among the models discussed in this overview. This model captures the diverse materials and particles constituting the porous electrode, along with the spaces filled by the electrolyte, enabling the modeling of spatial distributions, such as ion flow around particles (graphical model representation at Figure 33).

Despite its realism, practical applications encounter two major challenges with the high-fidelity microscale model. Firstly, it demands extensive computational resources and presents the complex task of acquiring the complete microscale geometry through tomography. Secondly, similar to the homogenized model, many predictions regarding spatial distributions of quantities of interest cannot be validated, given the current absence of methods to observe them in operando.

While the microscale model holds theoretical value, its practical utility hinges on the reduction of solving times and the development of experimental techniques

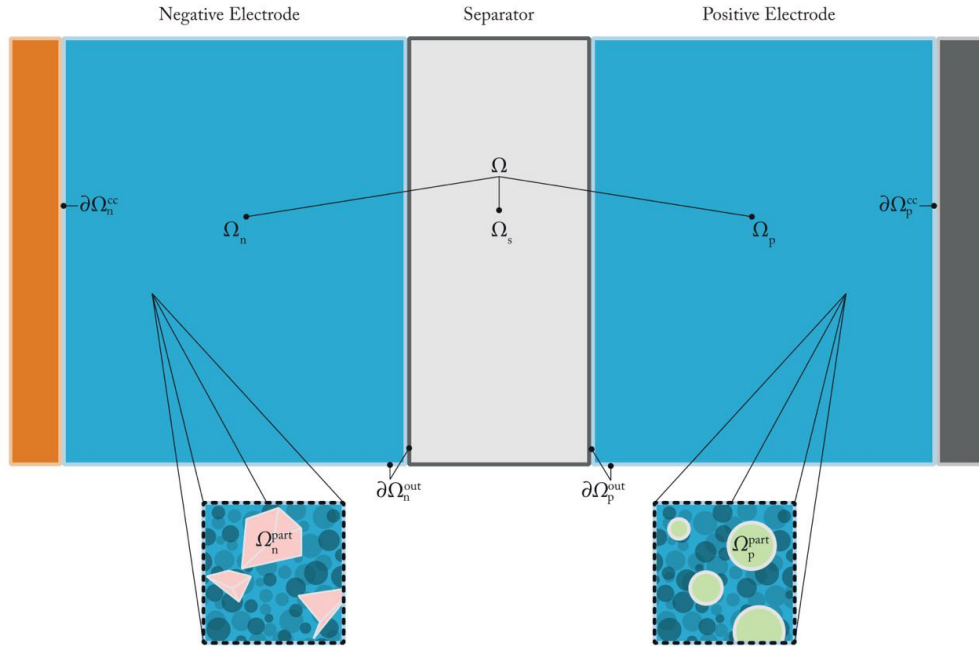


Figure 32: Sketch of the geometry of the homogenised model [17]. The macroscale domains (electrodes Ω_n and Ω_p , and separator Ω_s) are treated as continuous material. At each point in the electrodes, there is a representative microscale domain (electrode particles Ω_n^{part} and Ω_p^{part}). Ω is defined as $\Omega = \omega_n \cup \Omega_s \cup \Omega_p$

enabling the monitoring of internal battery states during operation. This serves as a reminder that complexity does not necessarily bring closer to the primary goal of battery modeling: highly accurate agreement with experimental results can be attained using less complex models.

Despite of that, there are some examples of its usage in literature, as done by Less et al. [78], where a microscale model was developed to fully resolve anode and cathode structures, while treating the separator as an effective electrolyte property. The microscopic simulation proved valuable for studying the influence of microstructure on cell performance. However, the model had limitations analogues to the previously mentioned ones: reaction coefficient/proportionality factor was assumed based on literature findings and electrode microstructure resolution would have required an imaging method, increasing simulation complexity.

2.7.6 Model decision

After the review of all the characteristics of the electrochemical models, well schematized in Table 4, it is possible to decide which is the proper model for the scopes of this project.

For sure accuracy, modelling and physical representation are great points in favour of the microscale and homogenised models, however the drawbacks are incompatible

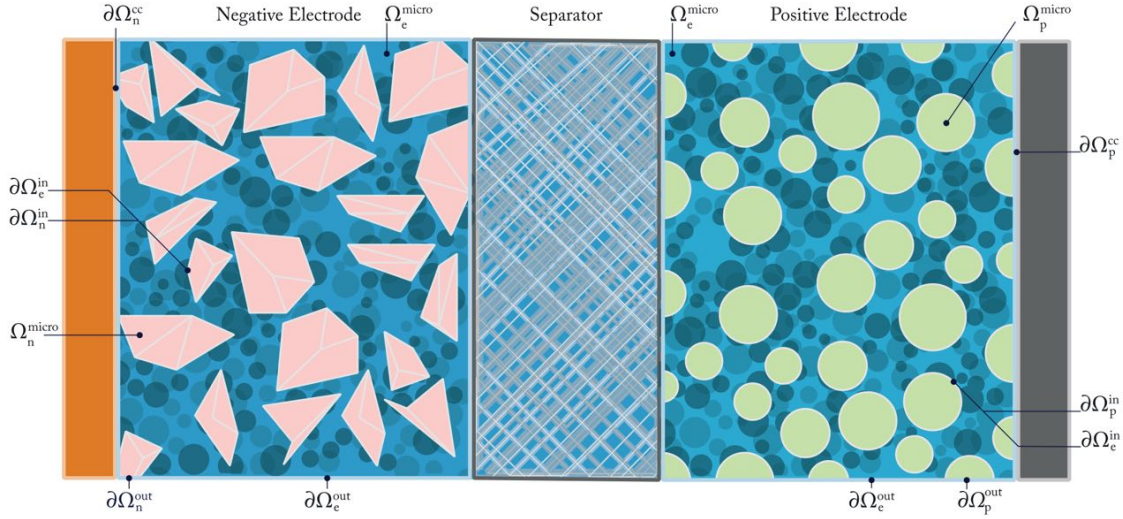


Figure 33: Sketch of the microscale model [17]. Each porous electrode (Ω_n^{micro} and Ω_p^{micro}) is composed of a matrix that includes both active and inactive materials. The voids in this porous structure Ω_e^{micro} are occupied by the electrolyte. The boundary of each domain is split into different subsets, therefore distinct boundary conditions can be imposed.

with the characteristics and needs of this thesis. The first problem is related to the huge complexity of such models that, for sure guarantees high fidelity of the cell, but is not worth for the purpose and would require enormous computational effort that it is not actually sustainable by this project's means. Furthermore the examples in literature are quite marginal, mostly related to theoretical dissertation not based on real cells. This is clearly due to the difficulties in identification of the actual geometry of the electrodes (with a challenging validation related to images analysis), the impossibility of validation of many characteristic parts of such models (i.e. non-symmetric lithium distribution within particles that cannot be directly observed) and several reaction coefficient/proportionality factors assumed based on literature findings. For these reasons the microscale and homogenised models will not be utilized for the modelling in this thesis.

At this point it is worth comparing the remaining feasible models: SPM, SPMe and DFN model, given that they all share the same simplified geometry which allows for direct comparison of their variables. Brosa [17] implemented the three models in PyBaMM software for a NMC cell. The results showed that the SPMe model closely captures all the spatially distributed effects of DFN, but the SPM did not, given that it does not include electrolyte dynamics. This resulted in turn in a poor prediction of the terminal voltage, especially at higher C-rates. This represents the main difference (and limitation) of SPM with respect to SPMe/DFN. As a consequence SPM cannot be taken as model for our purpose.

Table 4: Electrochemical model summary.

Model	Strengths	Weaknesses
SPM	<ul style="list-style-type: none"> • Highest simplicity. • Minimum parameters required. • Complexity aligned with ECM. 	<ul style="list-style-type: none"> • Electrolyte dynamics not included. • Good accuracy only for low C-rates.
SPMe	<ul style="list-style-type: none"> • Simplicity. • Electrolyte dynamics included. • Good accuracy at middle rates. 	<ul style="list-style-type: none"> • Higher number of parameters required compared to SPM. • Spatial distribution of lithium-ion not included. • Decreased accuracy at high C-rate.
DFN	<ul style="list-style-type: none"> • Remarkable accuracy across a broad spectrum of operating conditions. • Still computational feasible. • Included spatial distribution of lithium-ions across the electrodes. 	<ul style="list-style-type: none"> • Higher computation cost compared to simpler models. • Effect related to not spherical nature of electrodes not encompassed.
Homogenised	<ul style="list-style-type: none"> • High accuracy in all the operating conditions. • Three dimensional model. 	<ul style="list-style-type: none"> • Required representative microstructure in addition to parameters. • High complexity. • Challenging validation .
Microscale	<ul style="list-style-type: none"> • Highest theoretical accuracy. • The most complete model. 	<ul style="list-style-type: none"> • Highest complexity. • High computational effort. • Validation mainly done by means of literature.

The difference between the two remaining models is quite narrow (as previously demonstrated), however it has been chosen the SPMe over DFN for two main reasons: firstly because, since the performances are quite similar, it is preferred the simplest. Secondly the spatial distribution of lithium across the electrodes is not of interest, hence is not worth to include it in the model.

The choice is argued by Marquis et al. [86] study, where SPMe showed to give good agreement with the DFN model whilst providing dramatic decreases in computational complexity, with reduced memory requirements and computation time, both highly desirable features for parameter estimation and optimization procedures.

2.7.7 SPM_e Founding equations

In the literature, several models fit under the category of SPM_e. The main differences are in the methods and boundary/initial conditions used to calculate voltage and other derived quantities, not in the differential equations used to determine the concentrations in particles and electrolyte. In SPM-type models, the particles are assumed to (de)lithiate uniformly and therefore a representative particle can be solved for each electrode.

Table 5: Model variables.

c_k	Lithium concentration in the electrode particles	mol m^{-3}
c_e	Lithium concentration in the electrolyte	mol m^{-3}
N_k	Molar flux of lithium in the electrode particles	$\text{mol m}^{-2} \text{s}^{-1}$
N_e	Molar flux of ions in the electrolyte	$\text{mol m}^{-2} \text{s}^{-1}$
i_k	Current density in the electrodes	A m^{-2}
i_e	Current density in the electrolyte	A m^{-2}
j_k	Reaction current density	A m^{-2}
j_{k0}	Exchange current density	A m^{-2}
ϕ_k	Electrode potential	V
ϕ_e	Electrolyte potential	V
T	Temperature	K
η_k	Overpotential at the electrode-electrolyte interface	V

Table 6: Model parameters and functions.

a_k	Product of particle radius and surface area density	—
b_k	Particle surface area per unit of volume	m^{-1}
c_k^{max}	Maximum particle concentration	mol m^{-3}
c_{e0}	Initial/rest lithium ion concentration in the electrolyte	mol m^{-3}
c_{k0}	Electrode initial concentration	mol m^{-3}
c_p	Specific heat capacity	$\text{JK}^{-1}\text{kg}^{-1}$
D_k	Lithium diffusivity in particle	$\text{m}^2 \text{s}^{-1}$
D_e	Lithium ion diffusivity in electrolyte	$\text{m}^2 \text{s}^{-1}$
i_{app}	Applied current density	A m^{-2}
K_k	Normalized reaction rate	$\text{mol m}^{-2} \text{s}^{-1}$
L_k	Electrode and separator thicknesses	m
R_k	Particle radius	m
t^+	Cation transference number	—
U_k	Open-circuit potential (OCP)	V
B_k	Transport efficiency/inverse MacMullin number	—
ϵ	Electrolyte volume fraction (porosity)	—
σ_e	Conductivity (electrolyte)	S m^{-1}
σ_k	Conductivity (electrode)	S m^{-1}
γ_k	Ratio of maximum lithium concentrations in solid	—

Table 7: Model constants.

F	Faraday constant	C mol ⁻¹
R	Gas constant	J K ⁻¹ mol ⁻¹
b	Bruggeman coefficient	—

Table 8: List of symbols used in SPMe equations.

e	In electrolyte
n	In negative electrode/particle (anode)
s	In separator
p	In positive electrode/particle (cathode)
k	In domain $k \in \{n, s, p\}$
x	Spatial coordinate

The governing equations for the representative particles are [17]:

$$\frac{\partial c_k}{\partial t} = \frac{1}{r^2} \frac{\partial}{\partial r} \left(r^2 D_k(c_k) \frac{\partial C_k}{\partial r} \right), \quad \text{in } 0 < r < R_k, \quad (5)$$

$$\frac{\partial c_k}{\partial r} = 0, \quad \text{at } r = 0, \quad (6)$$

$$-D_k(c_k) \frac{\partial c_k}{\partial r} = \frac{j_k}{b_k F}, \quad \text{at } r = R_k, \quad (7)$$

$$c_k = c_{k0}, \quad \text{at } t = 0, \quad (8)$$

for $k \in \{n, p\}$ and where:

$$j_n = \frac{i_{app}(t)}{L_n}, \quad j_p = -\frac{i_{app}(t)}{L_p}. \quad (9)$$

The SPMe also accounts for electrolyte effects, so the governing equation for lithium

ions in the electrolyte are needed:

$$\epsilon(x) \frac{\partial c_e}{\partial t} = \frac{\partial}{\partial x} \left(D_e(c_e) B(x) \frac{\partial c_e}{\partial x} - \frac{t^+}{F} i_e \right) + \frac{b(x) j(x, t)}{F}, \quad \text{in } 0 < x < L, \quad (10)$$

$$\frac{\partial c_e}{\partial x} = 0, \quad \text{at } x = 0, L, \quad (11)$$

$$c_e = c_{e0}, \quad \text{at } t = 0, \quad (12)$$

where

$$\epsilon(x) = \begin{cases} \epsilon_n, & \text{in } 0 \leq x \leq L_n, \\ \epsilon_s, & \text{in } L_n \leq x \leq L - L_p, \\ \epsilon_p, & \text{in } L - L_p \leq x \leq L, \end{cases} \quad (13)$$

$$B(x) = \begin{cases} B_n, & \text{in } 0 \leq x \leq L_n, \\ B_s, & \text{in } L_n \leq x \leq L - L_p, \\ B_p, & \text{in } L - L_p \leq x \leq L, \end{cases} \quad (14)$$

$$b(x) = \begin{cases} b_n, & \text{in } 0 \leq x \leq L_n, \\ b_s, & \text{in } L_n \leq x \leq L - L_p, \\ b_p, & \text{in } L - L_p \leq x \leq L, \end{cases} \quad (15)$$

$$j(x, t) = \begin{cases} j_n(t), & \text{in } 0 \leq x \leq L_n, \\ 0, & \text{in } L_n \leq x \leq L - L_p, \\ j_p(t), & \text{in } L - L_p \leq x \leq L, \end{cases} \quad (16)$$

$$i_e(x, t) = \begin{cases} \frac{i_{app}(t)}{L_n}, & \text{in } 0 \leq x \leq L_n, \\ i_{app}(t), & \text{in } L_n \leq x \leq L - L_p, \\ \frac{i_{app}(t)}{L_p} (L - x), & \text{in } L - L_p \leq x \leq L. \end{cases} \quad (17)$$

The solution for $c_e(x, t)$ can then be used to compute the electrolyte potential ϕ_e a

posteriori, by integrating the expression:

$$i_e(x, t) = \sigma_e(c_e)B(x) \left(-\frac{\partial\phi_e}{\partial x} + \frac{2RT}{F}(1 - t^+) \frac{1}{c_e} \frac{\partial c_e}{\partial x} \right) \quad \text{in } 0 < x < L. \quad (18)$$

Here it is assumed the electrolyte is ideal such that $\mu_e = RT \log(c/c_{e0})$.

Multiple methods have been suggested in the literature to compute the terminal voltage of the cell. In any case the terminal voltage $V(t)$ can be written in the form:

$$V(t) = U_{eq} - \eta_r - \eta_c - \Delta\phi_e - \Delta\phi_s \quad (19)$$

where U_{eq} is the open-circuit potential of the cell, η_r and η_c are the potential drops due to the reaction and concentration overpotentials, respectively; and $\Delta\phi_e$ and $\Delta\phi_s$ are the Ohmic losses in the electrolyte and the electrodes, respectively. During discharge ($i_{app} > 0$), as lithium ions flow from the negative to positive electrode, the quantities $\eta_r, \eta_c, \Delta\phi_e$ and $\Delta\phi_s$ are all positive, and represent the reduction in the open circuit cell potential resulting from these loss mechanisms. During charge ($i_{app} < 0$) these quantities are all negative and therefore represent the extra potential, above the open-circuit potential, required to overcome the internal resistances in the cell.

The exchange current densities are defined as:

$$j_{k0}(x, t) = FK_k \sqrt{\frac{c_e(x, t)}{c_{e0}} \frac{c_k(r, t)}{c_k^{max}} \left(1 - \frac{c_k(r, t)}{c_k^{max}} \right)} \Bigg|_{r=R_k} \quad \text{for } k \in \{n, p\}. \quad (20)$$

In turn, $j_{k0}(t)$ is defined as the exchange current density averaged over the corresponding electrode.

2.8 Battery second life

As previously mentioned, the final target of this study is the identification and thermal performance testing of second life scenarios for the HONDA CLARITY's battery pack. However, the decision and, successively, the design process, is not an easy task and cannot be taken as granted. Indeed several stages and factors must be considered in order to obtain the best possible result. The scope of this paragraph is to give a brief and clear idea of the repurposing procedure that allows to achieve such optimal results.

2.8.1 Repurposing procedure

The repurposing procedure must be really well defined and schematized, with a logical flow constituted of different steps:

1. **Collection:** PHEVs and EVs equipped with batteries are collected by authorized treatment centers, battery manufacturers or third-party integrated management companies [64].
2. **Disassembly:** After dismantling from the vehicle, the battery is visually checked. Successively the pack can be further disassembled, with removal of casing, electrical and mechanical connections between the cells, cooling system, BMS and even of the cells themselves. Procedure and components to be removed depends to the configuration in which the battery will be re-used: stacking battery packs, refurbishing battery made from used modules and refurbishing modules from used cells are the possible options, depending on several factors. This choice is really delicate and crucial, for this reason is further discussed in section 2.8.2.
3. **Screening:** In this step the battery is analyzed to detect damages of the system and classified by several factors. After that, it is necessary evaluate status and aging (SOH or RUL) of the retired batteries by means of direct measurement or analysis: open-circuit voltage (OCV), internal resistance, temperature performance, capacity tests, hybrid pulse power characterization (HPPC), incremental capacity analysis, electrochemical spectroscopy, are just some of the available possibilities that, however, require time [64] [113]. After further safety tests and performance evaluation (also combined with data collected by BMS), batteries with similar first life-cycle profiles and health statuses can be clustered to achieve better consistency [64].
4. **Technical viability of different solutions:** This step is the core of the repurposing procedure. Firstly is fundamental to analyze all the requirements in second life application decision, including: capacity, max power, weight, volume , BMS, EMS and thermal management. All this aspect are widely discussed in section 2.8.4.
5. **Economic evaluation:** After the emergence of several eligible second life scenarios, this step is based on the estimation of cost and potential revenues of each solution [96].

6. **Reassembly and/or Remanufacturing:** Depending on the chosen configuration approach and second life scenario, the pack is reassembled in a way that is somehow inverse to the disassembly procedure, with the electrical and mechanical connection of the modules, followed by mounting of BMS, EMS and TMS.

2.8.2 Potential configurations

The review of different configurations is an important part of the battery assessment process. In this section, the possible configurations are analyzed, including the advantages and disadvantages reported in Table 9.

- **Stacking used EV battery packs:** in this configuration multiple battery packs are connected with the least possible modifications. The connection can be done in parallel (more common considered the high voltages of the EV battery packs), allowing disconnection of one battery pack in case of failure, while maintaining system operation (but with reduced capacity and power capabilities). Also connection in series can be employed, with critical issues related to potential unexpected currents flows that may develop between batteries with different voltages. For this reason EV battery packs with similar characteristics facilitate the implementation of this type of configuration.
- **Refurbished battery made from used modules:** this configuration requires disassembly of the battery pack to the module level, in order to form a new battery pack that fits the new application (commonly characterized by high energy demand). Modules with similar characteristics that are able to communicate with a superior BMS should be used in this type of configuration.
- **Refurbished modules made from used cells:** in this configurations battery pack is disassembled to the cell level. The cells are then packed into new modules and new battery systems. This is particularly valuable when pack or module dimensions are not suitable for the application.

2.8.3 Configuration decision

Discussing the configuration for this thesis work, the choice is inevitably dictated by the characteristics of HONDA CLARITY's battery pack. Being a PHEV subjected to more room requirements, the 14 modules are not huddled-up in an unique battery pack (like a classical EV where modules are collocated under the floor in an unique battery pack), but rather they are allocated partially under front seats and partially

Table 9: Summary of main advantages and drawbacks of the second life application configuration [96].

Second life configuration	Advantaged	Disadvantages
Stacking battery packs	<ul style="list-style-type: none"> • Thermal control can use the internal heating and cooling of the battery packs. • Lower cost and complexity since disassembly steps are removed and internal components of the pack are used. • Reduced waste generated by new battery that would otherwise be used in this application. • Less manipulation, implying reduced risk of failure since original BMS from the OEM could be leveraged. 	<ul style="list-style-type: none"> • Performance affected by worst performing modules/cells. • Shape of the pack cannot be modified without additional costs. • Required modification of thermal management system if it was based on vehicle radiators. • Limited flexibility in sourcing components for repair and periodic maintenance. • If parallel connected, unexpected current flows may develop between the packs.
Refurbished battery made from used modules	<ul style="list-style-type: none"> • Best module(s) of the pack can be selected and the worst discarded. • Greater dimension flexibility with respect of stacking full packs. • BMS is designed for the new application, with direct communication with power converter. • Simpler to repair, if one modules fails, it can be replaced. 	<ul style="list-style-type: none"> • Performance affected by worst performing cells. • Modification or even re-design of thermal management system is required. • Not feasible if the architecture is cell to pack typology. • Higher cost and complexity due to scraps/recycled components of the EV battery pack and employment of new components.
Refurbished modules made from used cells	<ul style="list-style-type: none"> • Best cell(s) of the pack can be selected and worst discarded. • Highest flexibility in designing size and shape of the remanufactured system. 	<ul style="list-style-type: none"> • Higher cost to disassemble the pack at cell level. • More challenging disassemble due to potential damage of the cells. • Highest waste of components that are unable to be re-used. • Highest cost for provision of new housing, busbars, sensors, BMS and re-assembly process.

under rear seats (look at Figure 25b). Designing and realizing a battery with such shape is impractical. For this reason the "stacking battery packs" configuration must be discarded.

The choice between the last two configurations is forced by the inherent characteristics of the prismatic cells, constituting the reference module. Indeed, Table 1 highlights the requirement of compression to avoid electrodes delamination. This compression is provided by structural cases and plate well visible in Figure 7b. If this pressure failed during dismantling procedure, the consequences would be really severe, with an abnormal expansion of the cell (visible in Figure 38) and a corresponding loss of capacity (as expressed in section 2.4.2). Consequently, the "refurbished modules made from used cells" configuration cannot be taken into account for this study.

Therefore, the choice falls on the "refurbished battery made from used modules" configuration, which represents a really good compromise between modularity (in terms of shape and performance), disassemble procedures and additional components. For this kind of approach, in fact, it would be necessary to implement a completely new BMS, EMS and TMS. However, as previously mentioned, the focus of this thesis will be only on the implementation of the last system for the different secondary life applications.

2.8.4 Second usage requirements

Lithium-ion batteries can be re-used in a broad number of applications which clearly require different characteristics. This is the reason why, for each specific case, the following requirements are usually analyzed:

- **Capacity:** the maximum energy storage capacity to be installed in each application is determined by several factors such as the available capital, energy or/and power demand, weight and volume requirements, future forecast degradation.
- **Max power:** this depends on the maximum C-rate the battery can deliver. For lithium-ion batteries, it typically varies from 0.1C up to few C, with higher rates that can be delivered in small pulses (few seconds). Despite that, discussing about a second life application, C-rate may be limited to values around 1. Because of the battery design, the power requirements is often interrelated with choosing the most suitable capacity.
- **Weight:** to obtain the same capacity with second life cells (SOH<80%) as with

first life cells, 25% more cells/modules/batteries are needed, consequently 25% more net weight of cells will be installed. Depending on the application this aspect can be prohibitive, restrictive or irrelevant.

- **Volume:** the same discussion done for the weight is valid also for the volume, with importance highly dependent on the considered application.
- **Battery management system (BMS):** it ensures safe battery operation in all the charge and discharge phase. Depending on the new second life application, a new BMS, has to be implemented.
- **Energy Management system (EMS):** the EMS is in charge of controlling the flow of energy in the installations between different components. Depending on the new second life application, a new EMS, coupled with the battery components, has to be implemented.
- **Thermal management:** its role has been widely discussed in section 2.2 and 2.3. Depending on the ambient temperature and working conditions, the decision of the second life application must consider a proper TMS that can maintain temperatures in optimal range avoiding further aging of the battery [96].
- **Economic feasibility**

In Table 10 are summarized the requirements that, in this thesis, will be observed in the decision and design of the second life scenarios for the HONDA CLARITY's battery.

Table 10: Requirements observed in this thesis for second life application decision and design.

Capacity	Max power	Weight	Volume	BMS	EMS	Thermal management	Economic feasibility
✓	✓	+/-	+/-	×	×	✓	×

2.8.5 Second life scenarios

Potential second-life applications are those where capacity and density are not critical and fast and continuous charging/discharging are not expected. A significant number of potential second-life applications were found and, for simplicity's sake, they have been categorized into three main groups, according to their degree of mobility: mobile, semi-stationary or stationary [93].

The first major category is “mobile applications”, i.e., applications where the battery is expected to move during usage. The possibility in this field are several since the EOFL is commonly experienced when the battery reaches 70–80% capacity retention. Consequently, the energy provided by the battery is sufficient to satisfy most of the daily trip of a short-range EV. Similarly, SLBs can be installed in hybrid trucks operating in urban areas to provide power at low speeds before the internal combustion engine (ICE) starts up. Another possibility is to use the batteries for the propulsion of micro-mobility vehicles (e.g., e-bikes, e-scooters, electric wheelchairs), lightweight vehicles (e.g., golf carts, three-wheel vehicles) and industrial vehicles (e.g., forklifts, pallet trucks, tractors) or for the internal energy management of some vehicles (e.g., food trucks) [4]. Other examples of mobile second-life applications include the use of SLBs as buffer storage in fuel cell (FC) vehicles or different types of transportation technologies, including rail or marine applications. The higher energy density and consequently the better weight and volume characteristic, results in LIBs being more appealing than conventional lead–acid batteries not only in all the above-mentioned applications, but also in such applications where lead-acid batteries are dominant (e.g, in automotive starting, lighting and ignition). The main obstacle in using LIBs rather than lead–acid batteries is the difference in cost, which makes the use of lead–acid batteries more widespread than LIBs for certain types of applications. However, when considering the case of SLBs, the price difference flattens out, leaving room for the emergence of new second-life applications linked to the replacement of lead–acid batteries [37].

In the second category defined as "semi-stationary", the batteries are not intended to operate while moving but are expected to be relocated frequently. Relevant examples are represented by power-stations for construction site, major events, outdoor camping and emergency. Furthermore SLBs can serve as really valid option for automotive charging stations [101] [87].

The last major category of second-life applications includes stationary use cases, i.e., the battery is not expected to move during its operational cycle. Consequently, less stringent weight and volume requirements are needed to be taken into account. Moreover, batteries have a reduced possibility of being mechanically abused, which could allow for less stringent safety requirements than those applied in the case of mobile applications. In this scenario, the employment of SLBs as energy storage system (ESSs) is dominant. ESSs are branched depending on the consumer types.

The first type of consumer is at the residential level and therefore concerns individual households. This scenario is particularly suitable for former EV/PHEV's

batteries since they can count on optimal performance to satisfy power and capacity requirements. In any case it must be mentioned that, in this case, SLB undergoes wider DOD and larger SOC swing window if compared to other applications of the same category [88]. Residential ESSs can store energy when consumption is low and release energy in the opposite case, resulting in smoothing the load and participating in the energy arbitrage business. This not only provides economic benefit but also a more environmentally sustainable solution, reducing the strain on the electric grid. Furthermore, SLBESSs can be used in combination with photovoltaics (PV), encouraging RES usage and promoting the decentralisation of the electricity production system. The SLBESSs can also act as an energy backup in the event of a power failure or blackout. The use of SLBs also tackles the problem of the high costs of using new batteries, which is the main limitation for the installation of domestic ESSs [73].

The repurposed energy storage systems represents an efficient and advantageous solution also in commercial and industrial field. Demand charges are additional fees that utilities charge commercial or industrial customers for the highest power demand recorded by the meters. SLBESSs can be employed to reduce demand charges and energy consumption by shifting energy usage from high to low cost and maintaining a constant supply of electricity. Especially if connected to renewable sources, economic benefits can be maximized [64].

Another important field of application of SLBEEs is in renewable energy, such as wind and solar energy, which has increased significantly in the past decade [27]. However, these systems are not stable, due to their functioning principle based on unstable natural phenomena. Consequently, the need ESSs capable of regularizing and smoothing the output power of a plant has become compelling. SLBESSs represent a promising solution due their scalability, flexibility, fast dynamics, and, more importantly, low cost. In these kind of applications, SLBESSs usually operate at low/middle DOD, leading the battery to less aging and extending the second life service. Moreover, the energy access issues in remote areas, where the grid is not economically viable, need to be solved, especially for communities in developing countries. Renewable energy generation technologies, coupled with repurposed lithium-ion batteries as ESSs, are a really appealing solution to provide reliable electricity to inhabitants in such remote and isolated minigrids [6].

The last field of the stationary application can be defined as backup power. In power plants, fault and temporary maintenance will inevitably lead to the interruption of power generation. In addition, the black-start of a power plant requires some

initial power input to start the plant after a sudden outage. Thus, the backup energy sources are used to provide energy during these moments. The battery power requirements are certainly high but the usage is occasionally (10-20 annual cycles with a duration between 15 and 60 minutes [84]). SLBESSs are the ideal choice for lower energy storage cost, fast response, and power capacity. Furthermore they can be used to help end-users respond to the emergency of power supply interruption, quickly providing backup power. Besides that, the battery storage system can be used in telecommunications and data centres as the uninterruptible power supply (UPS) [19].

Table 11: Mobile second-life applications [93].

Category	Application
Commercial EVs	Short-range EVs Hybrid trucks
Industrial vehicles	Forklifts Pallet trucks Tractors Sweepers Telescopic handlers
Micro-mobility	E-bikes E-scooters Electric wheelchairs
Automotive lead-acid replacement	Starting Lighting Ignition Electric devices
Lightweight vehicles	Golf carts Three-wheel vehicles
Marine applications	Hybrid propulsion Load-levelling Peak shaving
Rail transport	Trams power supply Trams backup system Trains power supply Trains backup system
FC-based transportation	Energy buffer for H2FC

Table 12: Stationary second-life applications [93].

Category	Application
Mobile power supplies	Construction sites Major events Outdoor camping EV Charging stations
Lead-acid replacement	Communication backup power UPS
EV charges	On-grid buffer storage Off-grid buffer storage
Special grids	Micro-grids Smart grids
Residential ESS	Load following RES connection Backup power
Commercial ESS	Peak shaving Load following Backup power
Industrial ESS	Load levelling Peak shaving Transmission stabilization Spinning reserve
Renewable ESS	Power smoothing Volt/Var assistance Firming Power quality Frequency control

2.9 Existing literature

In the preceding sections of this comprehensive literature review, all facets related to the interdisciplinary nature of this thesis have been explored, encompassing battery modeling, thermal modeling, and the second life of automotive battery packs. An effective literature review must address not only the theoretical underpinnings of the project, as done in the earlier sections, but also critically evaluate the existing accredited literature. This is essential to gauge the utility, novelty, and contribution of the new study to the research field.

Table 13 serves this purpose by categorizing all the elements discussed in this thesis. Several papers have been meticulously reviewed, indicating whether each aspect is addressed in the respective studies.

The analysis reveals a comprehensive collection of papers tackling similar challenges as this thesis. However, none of these papers encompass all the fields involved in this work. Most focus solely on one area—battery modeling, thermal modeling, or second life applications. Some address two fields, combining battery and thermal modeling or thermal modeling and second life applications. Consequently, it becomes evident that the literature lacks a study that integrates all these fields. This thesis, therefore, represents a breakthrough and innovative study, uniquely addressing these challenges in a single project. This comprehensive approach makes the thesis particularly valuable from an engineering perspective, as it covers the entire process of repurposing a battery pack—from battery modeling through thermal modeling to the evaluation and assessment of second life applications.

Table 13: Literature analysis

Author	Reference	Cell modeling	Cell model test	Thermal model	3D modelling	Thermal simulation	Thermal test	Cooling analysis	Second usage definition	Application assessment
Yuan et al.	[130]	DFN/ECM	✓	✓	×	×	✓	×	×	×
He et al.	[39]	DFN	✓	✓	×	×	✓	×	×	×
Iraola et al.	[68]	ECM	✓	✓	×	×	✓	×	×	×
Hosseinzadeh et al.	[40]	SPM	✓	✓	×	×	✓	×	×	×
Wu et al.	[123]	DFN	✓	✓	×	×	✓	×	×	×
Xu et al.	[124]	SPM	✓	✓	×	×	✓	×	×	×
Darcovich et al.	[26]	SPM	✓	✓	✓	✓	✓	✓	×	×
Jiang et al.	[72]	SPM	✓	✓	×	×	✓	✓	×	×
Bahraei et al.	[8]	DFN	✓	✓	✓	✓	✓	✓	×	×
Murashko et al.	[98]	ECM	✓	✓	×	×	✓	✓	×	×
Akbarzadeh et al.	[3]	×	×	✓	✓	✓	✓	×	×	×
Kleiner et al.	[76]	×	×	✓	✓	✓	✓	×	×	×
Youssef et al.	[128]	×	×	✓	×	✓	✓	×	×	×
Tang et al.	[117]	×	×	✓	✓	✓	✓	×	×	×
Smith et al.	[114]	×	×	✓	✓	✓	✓	×	×	×
Zhu et al.	[132]	×	×	✓	✓	✓	✓	×	×	×
Guo et al.	[36]	×	×	×	✓	✓	✓	✓	×	✓
Thompson et al.	[119]	×	×	×	×	×	✓	✓	✓	✓
White et al.	[122]	×	×	×	×	×	✓	×	✓	✓
Abdel et al.	[1]	×	×	×	×	×	✓	✓	✓	✓
Haram et al.	[37]	×	×	×	×	×	×	×	✓	✓
Kamath et al.	[73]	×	×	×	×	×	×	×	✓	✓
Martinez et al.	[88]	×	×	×	×	×	×	×	✓	✓
Michelini et al.	[93]	×	×	×	×	×	×	×	✓	✓
Gohla et al.	[34]	×	×	×	×	×	×	×	✓	✓
Montes et al.	[96]	×	×	×	×	×	×	×	✓	✓
Thesis		SPMe	✓	✓	✓	✓	✓	✓	✓	✓

Battery modeling field.
 Battery modeling + Thermal modeling fields.
 Thermal Modeling fields.
 Thermal modeling + Second life fields.
 Second life field.

3 Methodology

This section concerning the methodology will strictly follow the flow chart previously presented in Figure 9.

3.1 Electrochemical model

First step is development of the cell electrochemical model. The implementation of a complete SPMe would require enormous amount of time and effort. For this reason it is decided to use the software PyBaMM (Python Battery Mathematical Modelling). PyBaMM is an open-source battery modeling software developed in Python, designed to implement several physics-based models and capable of running efficient simulations of battery performances, correlated with fast data visualization tools [47]. Furthermore the software offers modular framework (by separating models, discretisation, and solver) and ultimate flexibility to the end user, providing a unified interface through which to incorporate new models, alternative spatial discretisations, or new time-stepping algorithms. PyBaMM's architecture is based around two core components.

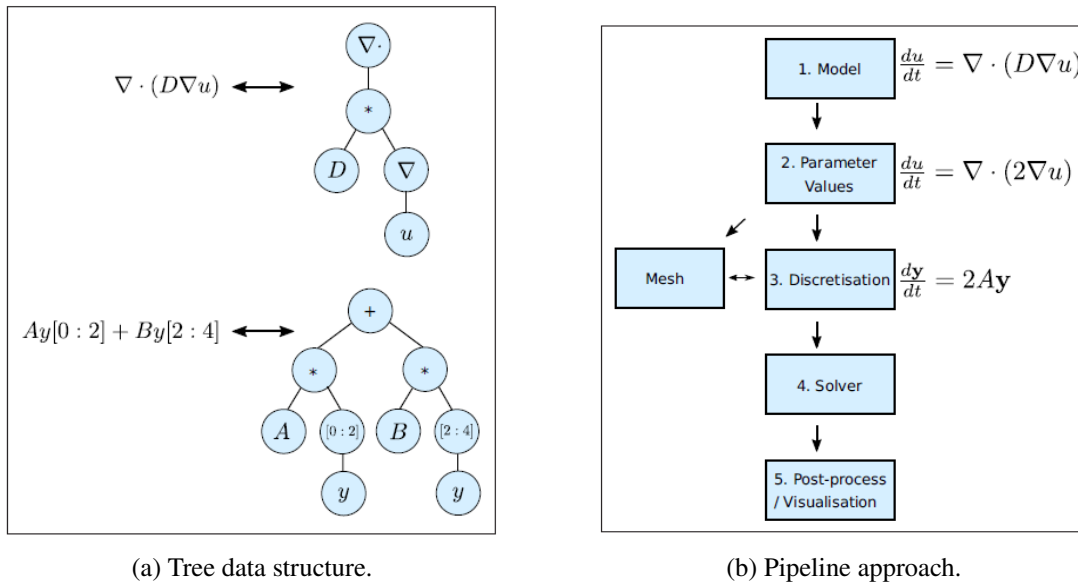


Figure 34: PyBaMM architecture [115].

The first is the expression tree (Figure 34a), which encodes mathematical equations symbolically. Each expression tree consists of a set of symbol which represents either a variable, parameter, mathematical operation, matrix, or vector. The expression trees in each model are organised within Python dictionaries

representing the governing equations, boundary equations, and initial conditions of the model.

The second core component is the pipeline process (Figure 34b) that, constructed in Python using PyBaMM classes, allows the users to have a full control over the entire process, with the possibility of inserting specific components at any stage. The approach is constituted by 5 steps:

1. Define a battery model and geometry using PyBaMM's syntax. This generates a collection of expression trees representing the model.
2. Parse the expression trees for the battery model and geometry, replacing any parameters with their provided numerical values.
3. the geometry and discretise the model on this mesh with user-defined spatial methods.
4. Solve the model using a time-stepping algorithm.
5. Post-processes the solution. Built-in post processing utilities provided access to any user-defined output variables at any solution time and state. Additionally, PyBaMM includes a number of visualizations utilities which allow for easy plotting and comparison of any of the model variables [115].

The effectiveness of this software has been demonstrated by Schmidt et al.[111], Chen et al. [23], Gaehring et al. [33] and in many other studies.

PyBaMM offers a complete SPMe, based on equations presented in section 2.7.7 coupled with boundary conditions, initial conditions and terminal voltage formulation from Marquis et al [86], partially reported below.

Governing equations

$$C_k \frac{\partial c_{s,k}^0}{\partial t} = -\frac{1}{r_k^2} \frac{\partial}{\partial r_k} \left(r_k^2 \frac{\partial c_{s,k}^0}{\partial r_k} \right), \quad k \in \{n, p\}, \quad (21)$$

$$C_e \epsilon_k \gamma_e \frac{\partial c_{e,k}^1}{\partial t} = -\gamma_e \frac{\partial N_{e,k}^1}{\partial x} + \begin{cases} \frac{i_{app}}{L_n}, & k = n, \\ 0, & k = s, \\ -\frac{i_{app}}{L_p}, & k = p, \end{cases} \quad k \in \{n, s, p\}, \quad (22)$$

$$N_{e,k}^1 = -\epsilon_k^b D_e(1) \frac{\partial c_{e,k}^1}{\partial x} + \begin{cases} \frac{xt^+ i_{app}}{\gamma_e L_n}, & k = n, \\ \frac{t^+ i_{app}}{\gamma_e}, & k = s, \quad k \in \{n, s, p\}. \\ \frac{(1-x)t^+ i_{app}}{\gamma_e L_p}, & k = p, \end{cases} \quad (23)$$

Boundary conditions

$$\left. \frac{\partial c_{s,k}^0}{\partial r_k} \right|_{r_k=0} = 0, \quad -\frac{a_k \gamma_k}{C_k} \left. \frac{\partial c_{s,k}^0}{\partial r_k} \right|_{r_k=1} = \begin{cases} \frac{i_{app}}{L_n}, & k = n, \\ -\frac{i_{app}}{L_p}, & k = p, \end{cases} \quad k \in \{n, p\}, \quad (24)$$

$$N_{e,n}^1 \Big|_{x=0} = 0, \quad N_{e,p}^1 \Big|_{x=1} = 0, \quad (25)$$

$$c_{e,n}^1 \Big|_{x=L_n} = c_{e,s}^1 \Big|_{x=L_n}, \quad N_{e,n}^1 \Big|_{x=L_n} = N_{e,s}^1 \Big|_{x=L_n}, \quad (26)$$

$$c_{e,s}^1 \Big|_{x=1-L_p} = c_{e,p}^1 \Big|_{x=1-L_p}, \quad N_{e,s}^1 \Big|_{x=1-L_p} = N_{e,p}^1 \Big|_{x=1-L_p}. \quad (27)$$

Initial conditions

$$c_{s,k}^0(r_k, 0) = c_{k,0}, \quad k \in \{n, p\}, \quad (28)$$

$$c_{e,k}^1(x, 0) = 0, \quad k \in \{n, s, p\}. \quad (29)$$

Terminal voltage

$$V = \bar{U}_{eq} + \bar{\eta}_r + \bar{\eta}_c + \bar{\Delta\Phi}_{Elec} + \bar{\Delta\Phi}_{Solid}, \quad (30)$$

where

$$\bar{U}_{eq} = U_p \left(c_{s,p}^0 \Big|_{r_p=1} \right) - U_n \left(c_{s,n}^0 \Big|_{r_n=1} \right), \quad (31)$$

$$\bar{\eta}_r = -2 \sinh^{-1} \left(\frac{i_{app}}{\bar{j}_{0,p} L_p} \right) - 2 \sinh^{-1} \left(\frac{i_{app}}{\bar{j}_{0,n} L_n} \right) \quad (32)$$

$$\bar{\eta}_c = 2C_e(1 - t^+)(c_{e,p}^{-1} - c_{e,n}^{-1}), \quad (33)$$

$$\bar{j}_{0,n} = \frac{1}{L_n} \int_0^{L_n} \frac{\gamma_n}{C_{r,n}} (c_{s,n}^0)^{1/2} (1 - c_{s,n}^0)^{1/2} (1 + C_e c_{e,n}^1)^{1/2} dx, \quad (34)$$

$$\bar{j}_{0,p} = \frac{1}{L_p} \int_{1-L_p}^1 \frac{\gamma_p}{C_{r,p}} (c_{s,p}^0)^{1/2} (1 - c_{s,p}^0)^{1/2} (1 + C_e c_{e,p}^1)^{1/2} dx, \quad (35)$$

$$\overline{\Delta\Phi}_{Elec} = -\frac{i_{app}}{\hat{\sigma}_e \sigma_e (1)} \left(\frac{L_n}{3\epsilon_n^b} + \frac{L_s}{\epsilon_s^b} + \frac{L_p}{3\epsilon_p^b} \right) \quad (36)$$

3.1.1 SPMe Generation

As expressed in section 2.7.2, the implementation of a complete SPMe requires 30 parameters: 9 for each electrode, 11 for the electrolyte and the battery temperature. Furthermore, in order to count on a model capable of performing simulations with different boundary conditions, PyBaMM requires numerous additional parameters. Fortunately, the software makes available several data sets, extrapolated from accredited literature, that can be used as starting point for an electrochemical model build up.

Therefore, after SPMe creation, parameter set of the graphite/NMC532 pouch cell of Mohtat et al. [95] is chosen, since it presents the same chemistry of the HONDA CLARITY's cell. The resultant model is capable of simulating any type of cycle, as visible in the example presented in Figures 35 and 36. In despite of that, the implemented SPMe does not represent yet, except for the chemistry, characteristics and behaviour of the HONDA CLARITY's cell.

```
# Model creation and parameter set population
model=pybamm.lithium_ion.SPMc()
parameter_values_Mohtat2020 = pybamm.ParameterValues("Mohtat2020")
# Experiment set-up
experiment = pybamm.Experiment(["Discharge at 10A for 8 minutes",
                                "Rest for 5 minutes",
                                "Charge at 9 A for 5 minutes",
                                "Rest for 10 minutes",
                                "Discharge at 10W for 20 minutes",
                                "Rest for 10 minutes"])
# Simulation run
sim=pybamm.Simulation(model,experiment=experiment, parameter_values=parameter_values_Mohtat2020)
solution=sim.solve(initial_soc=1)
```

Figure 35: PyBaMM code for SPMe creation, data set population and example of a simulation set-up.

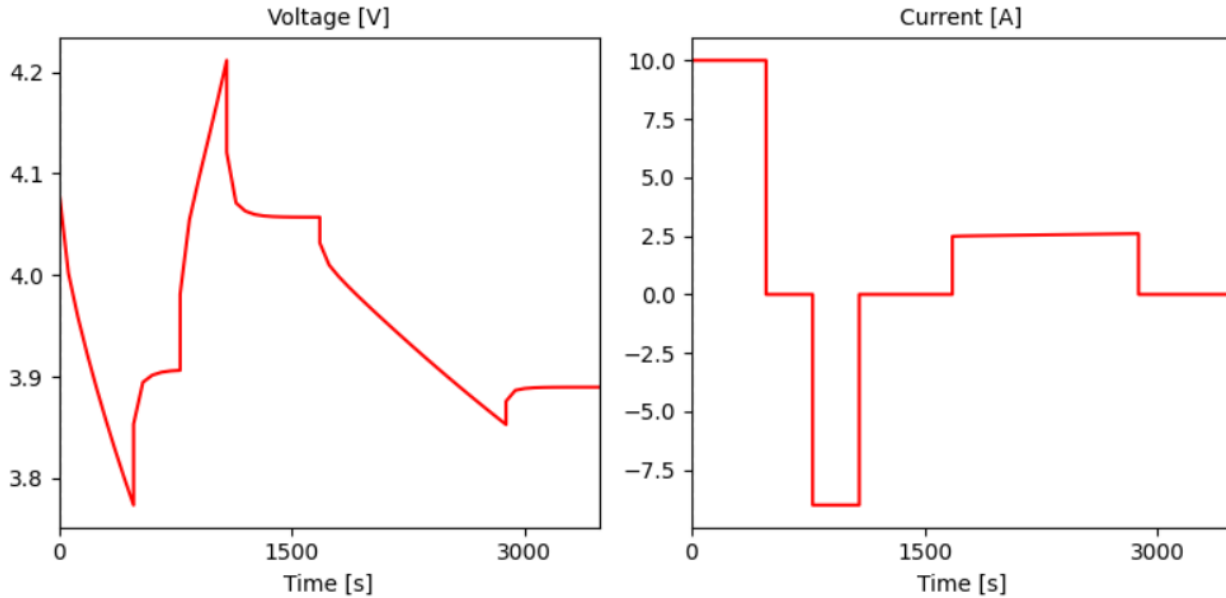


Figure 36: Result of the simulation example.

PyBaMM allows to replace singular parameters of the data set with values belonging to the cell for which is intended to build a faithful model. Obviously, this is not an easy task, especially for this thesis, in which the information about cell is really limited. The data-set update is realized into three steps:

1. Update of the parameters available from data-sheets.
2. Update of the parameters obtained by means of direct measurements done during a teardown procedure.
3. Update of the parameters decisive in matching cell experimental tests, by means of an optimization algorithm.

The first step just requires the update of information contained in the data sheets (reported in Table 2). Figure 37 shows the code for the updating procedure: each parameter of the data set, identified by a specific name and unite of measurement, is updated with the new value referred to the battery of interest.

```

# parameters from data set
parameter_values_Mohtat2020["Cell volume [m3]" ] = 3.67163e-4
parameter_values_Mohtat2020["Lower voltage cut-off [V]" ] = 2.5
parameter_values_Mohtat2020["Upper voltage cut-off [V]" ] = 4.2
parameter_values_Mohtat2020["Nominal cell capacity [A.h]" ] = 27.0
parameter_values_Mohtat2020["Open-circuit voltage at 0% SOC [V]" ] = 2.5
parameter_values_Mohtat2020["Open-circuit voltage at 100% SOC [V]" ] = 4.2
parameter_values_Mohtat2020["Number of cells connected in series to make a battery" ] = 1
parameter_values_Mohtat2020["Number of electrodes connected in parallel to make a cell" ] = 1

```

Figure 37: Data set update with cell specifications.

Since the implementation of second and third steps require detailed explanation, they are discussed in two dedicated paragraphs.

3.1.2 Cell teardown and geometrical parameters measurement

The second step of data set update focuses on all those geometrical macroscopic parameters the value can be measured empirically. Obviously this is not an immediate operation, but it is required prior the cell teardown, conducted in safe and standardize conditions. The procedure was held at Accullon Energy™'s laboratory, Columbus, OH. The objective was to measure the following geometrical parameters of the cell:

- Positive electrode thickness.
- Negative electrode thickness.
- Separator thickness.
- Positive electrode height / length.
- Negative electrode height / length.
- Positive electrode width.
- Negative electrode width.

In addition, it was possible to evaluate the electrodes arrangement within the case, unknown before the teardown.

As is possible to observe from Figure 38, the cell was slightly "puffed" due to its extraction from the module, with the consequent depressurization and delamination of the electrodes (as previously predicted in section 2.8.3).



Figure 38: Disassembled cell.

The equipment was composed of:

- * Circular saw drill.
- * Insulated screwdriver
- * Insulated pliers.
- * Digital micrometer (resolution 1 μm).
- * Ruler (resolution 1 mm).
- * Tape measure (resolution sixteenth of an inch).
- * Voltmeter.
- * Measurement cables.
- * Cell holder.
- * PC.
- * Battery cycle testers.
- * PPE (Personal Protection Equipment):
 - Insulating rubber gloves.
 - Welding face shield.
 - Flame resistant coat.

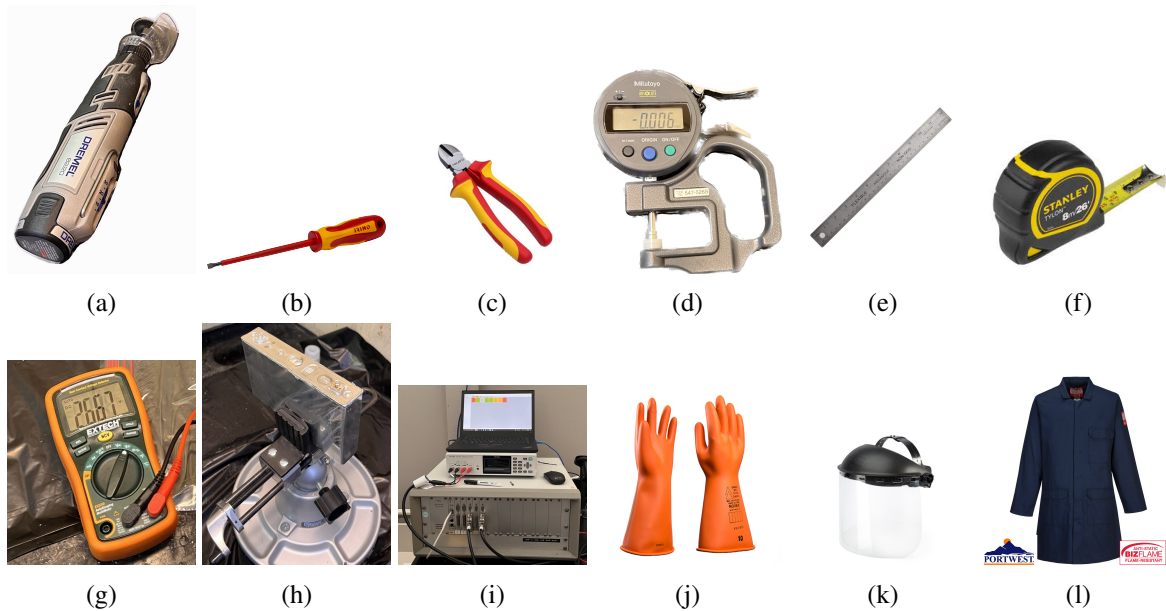
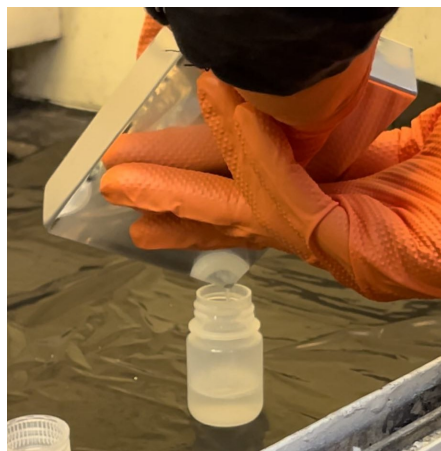


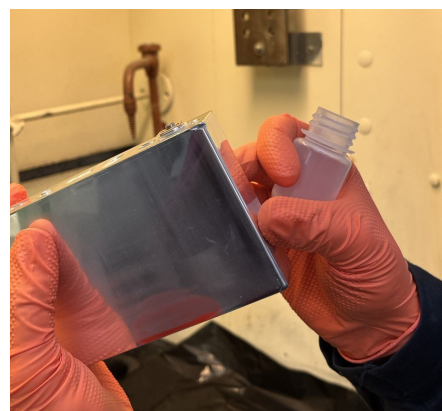
Figure 39: Extraction equipment

The procedure was composed of the following steps:

1. The cell was discharged using the battery cycle tester until 2.5V , the lowest nominal cell voltage corresponding to SOC=0%.
2. The cell was punctured on one of its corners using the circular saw drill. In this way it has been possible to draw the excess of electrolyte (almost 20 mL) not absorbed by the electrodes.



(a) Excess electrolyte removal (20 mL).



(b) Puncture in cell case.

Figure 40: Cell case puncture and draw of the electrolyte not absorbed by electrodes.

3. The cell was fixed on the holder to allow a safe and precise case cut. By means

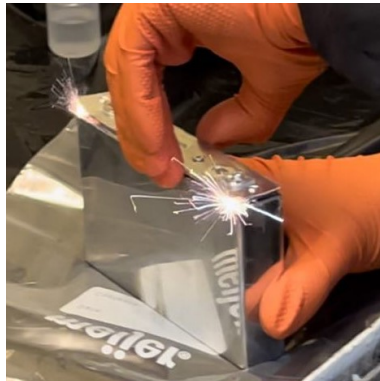
of the saw drill, the cut was performed along the whole edge in correspondence of the cell terminals (Figure 41a). Successively the screwdriver was used to separate the cell "lid" from the case (Figure 41b). As can be seen from Figure 41c, during electrodes extraction from the metal case, there was an emission of sparks. This phenomena was clearly due to the fact that, even if the cell had been discharged up to 0% of SOC, a residual voltage was still present between positive and negative electrode. As a consequence, the attempt to extract the electrodes from the case caused short circuits and sparks emission. In Figure 41d is evident the wound arrangement of the electrodes and aluminum / copper foil used as current collectors, respectively for positive and negative electrode.



(a) Case cut.



(b) Cell lid opening.



(c) Sparks emission.



(d) Electrodes arrangement.

Figure 41: Electrodes extraction.

4. In order to make the proper measurement, it was necessary to remove every element that was not part of electrodes or separator (Figures 42a and 42b).
5. Using the voltmeter it was possible to measure the actual voltage of the cell. The measured value was equal to 2.667 V (Figure 42c), even if the discharge had been done until 2.5 V (corresponding to the condition SOC=0%). This behaviour is appropriate since the cell underwent relaxation. Using the battery

cycle tester, a current was drawn from the cell in order to discharge it completely and allow safe operations. The resultant capacity (obtained multiplying the drawn current by the time to reach 0 V) was equal to 3 Ah. It is a decent amount of energy corresponding to more than 10% of the nominal capacity (equal to 27 Ah), that, however, cannot be used since the process would cause irreversible cycle life reduction, capacity fade and obviously damage of the cell.

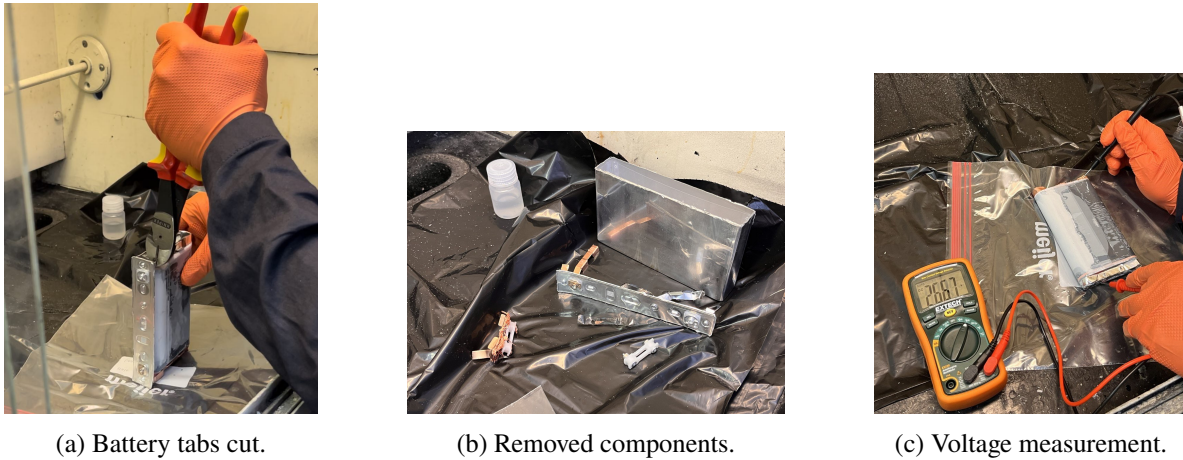


Figure 42: Stripped electrodes/separator and voltage measurement.

6. Once the cell was completely discharged, it was possible, by means of the digital micrometer, to measure the thicknesses of the electrodes (Figures 43a and 43b), of the separator (Figure 43c) and of the current collectors (Figures 43d and 43e). The corresponding measures are presented in Table 14.

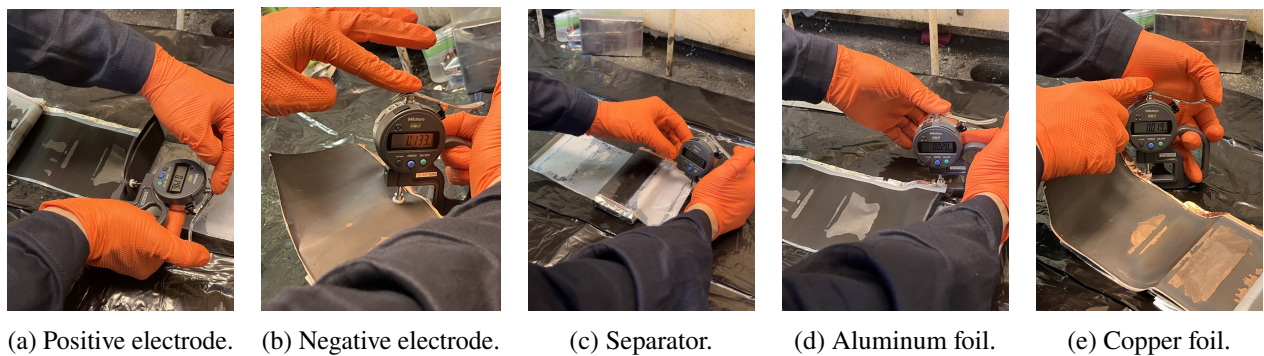
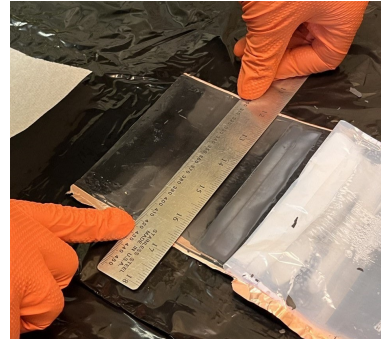


Figure 43: Thickness measurements.

7. The width of the electrodes (Figures 44a and 44b) was measured using a simple ruler. The corresponding measures are presented in Table 14.



(a) Positive electrode.



(b) Negative electrode.

Figure 44: Width measurements.

8. After those measurements, the electrodes were unrolled and separated, as visible Figure 45a. The electrodes were then spread out on the floor (Figure 45b), in order to measure their length by means of a tape measure (Figures 45c and 45d). The corresponding measures are presented in Table 14.



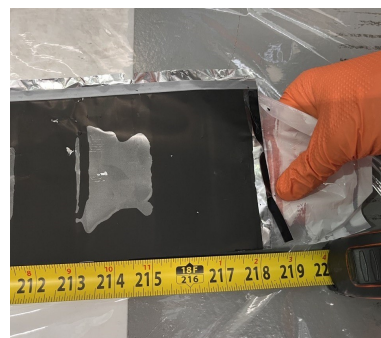
(a) Electrodes unrolling.



(b) Electrodes spreading.



(c) Negative electrode.



(d) Positive electrode.

Figure 45: Electrodes unrolling, spreading and electrodes length measurement.

Table 14: Measured geometrical parameters of the cell

Element measured	Unit	Value
Positive electrode thickness	μm	142 - 146
Negative electrode thickness	μm	133 - 139
Separator thickness	μm	20 - 22
Aluminum current collector	μm	20 -21
Copper current collector	μm	18 -19
Positive electrode width	mm	117
Negative electrode width	mm	121
Separator width	mm	127
Positive electrode length	" (m)	218 (5.537)
Negative electrode length	" (m)	226 (5.74)

Note: With caption "Positive/Negative electrode thickness" is meant the measure obtained with digital micrometer when the objective was to measure the electrode thickness. However the thickness necessary for the employed model is not the measured one. Actually the measure includes two layer of active material and one layer of foil thickness. Therefore, in order to obtain the real thickness of the active layers of the model (Figure 30), it is necessary to subtract the foil thickness from the electrode thickness values and then divide the result by two, as the foils are double-size coated. In particular the resulting values are 62 [μm] for positive and 58 [μm] for negative (using averaged thickness values).

With all the measurements obtained during battery teardown contained in Table 14, it is possible to update the parameter set of the electrochemical model. Figure 46 shows the code to do that, as previously done for the first step.

```
# measured parameters
parameter_values_Mohtat2020['Electrode height [m]'] = 5.537
parameter_values_Mohtat2020['Electrode width [m]'] = 0.117
parameter_values_Mohtat2020['Positive electrode thickness [m]'] = ((142e-6+146e-6)/2-(20e-6+21e-6)/2)/2
parameter_values_Mohtat2020['Negative electrode thickness [m]'] = ((133e-6+139e-6)/2-(18e-6+19e-6)/2)/2
parameter_values_Mohtat2020['Separator thickness [m]'] = 2.1e-05
parameter_values_Mohtat2020['Positive current collector thickness [m]'] = 2.05e-05
parameter_values_Mohtat2020['Negative current collector thickness [m]'] = 1.85e-05
parameter_values_Mohtat2020['Separator thickness [m]'] = 20e-6
```

Figure 46: Data set update with measured parameters.

3.1.3 Parameters optimization based on cell tests

Unfortunately, most of the key parameters necessary for the implementation of a representative electrochemical model are not provided in battery datasheets and cannot be directly evaluated without specific micro-scale measurement tools, which

are not available in this case. Consequently, the only way to obtain an accurate model is through the identification and optimization of those parameters that most significantly affect the model's response and behavior. As imaginable, this procedure requires experimental data (charge/discharge cycles) obtained from tests conducted on the cell, in order to determine which model parameters have the greatest impact and to effectively optimize them. This is undoubtedly the most challenging part of this thesis work, as it requires the simultaneous tuning of several parameters across different test data, with considerable uncertainty about how much each parameter might affect the response and behavior of the SPM_e.

The initial step involves testing the cells. However, as previously mentioned, resources for cell characterization were very limited. To address this, literature with a wealth of experimental tests was relied upon to glean essential insights on properly characterizing a cell with minimal tests. Notably, the studies by Broatch et al. [16] and Sangwan et al. [109] provided valuable guidance on effective cell testing to build a representative model, whether electrochemical or equivalent circuit-based.

The tests, like the cell teardown, were conducted at Accullon Energy™'s laboratory, on a cell still inserted in the battery module. This choice was done to not alter the mechanical properties and avoid the "puffing" of the cell, as observed during the teardown procedure, ensuring the record of meaningful data. Two distinct testing procedures were employed:

1. **CC-CV Charge/CC Discharge Cycles:** This test involves alternating charging and discharging cycles. The cell is charged with a constant current (CC) until it reaches the maximum voltage specified in the datasheet. This phase ensures a uniform and controlled charge, preventing overheating and overvoltage conditions. Once the cell reaches the predetermined voltage, the charging method switches to constant voltage (CV). The voltage is maintained constant, and the current gradually decreases until it drops to a very low value, ensuring the cell is fully charged as it allows for a complete reaction of active materials. This is followed by a CC (Constant Current) discharge: the cell is discharged at a constant current until it reaches its cutoff voltage (the cell's minimum safe voltage provided in the datasheet).

This test is straightforward in evaluating the cell's charge and discharge capacity, crucial for understanding the energy storage capability, which is highly dependent on current intensity. It also provides valuable insights into the Coulombic efficiency of the cell.

Due to the aforementioned limited resources, the cell was not tested across all its C-rates. Instead, considering the future field applications of this cell, the tests were limited to middle C-rates. Specifically, all cycles were characterized by common CC-CV charging phase, with CC performed at 0.3C until 4.2V, followed by CV until reaching 1.4A. After a 30-minute rest period, the cell was discharged from 100% to 0% SOC with CC discharge ranging from 0.1C to 1.5C, to explore the entire capacity spectrum. All the cycles were performed at room temperature (25°C).

2. **GITT (Galvanostatic Intermittent Titration Technique):** In this test, the cell is subjected to a series of current pulses (either charge or discharge) of a defined duration. Between each pulse, the cell is allowed to rest, during which no current is applied, enabling the cell to reach equilibrium.

This test is particularly effective for evaluating various aspects, including diffusion and kinetic dynamics. It also provides important information on the cell's behavior under different temperature conditions by assessing the equilibrium potential, which is related to the thermodynamics of the cell reactions.

Specifically, the GITT performed in the laboratory consisted of 80 discharge pulses, each at 1.5C for 31 seconds, followed by 5 minutes of rest. These tests were conducted at room temperature and at 45°C. Due to limited resources, the latter test is the only one performed in a high-temperature environment, serving as the sole reference for the cell's behavior dependency on temperature.

After testing the cell, it is necessary to identify the parameters that most significantly affect the model behaviour. Initially, specific studies focusing on parameter sensitivity analysis are accurately reviewed. Weihan Li et al. [80] present a comprehensive sensitivity analysis of the parameters mostly impacting on the electrochemical model response of a NMC lithium-ion cell. The results, shown in Figure 47, allow for the creation of a preliminary set of candidate parameters for the optimization process.

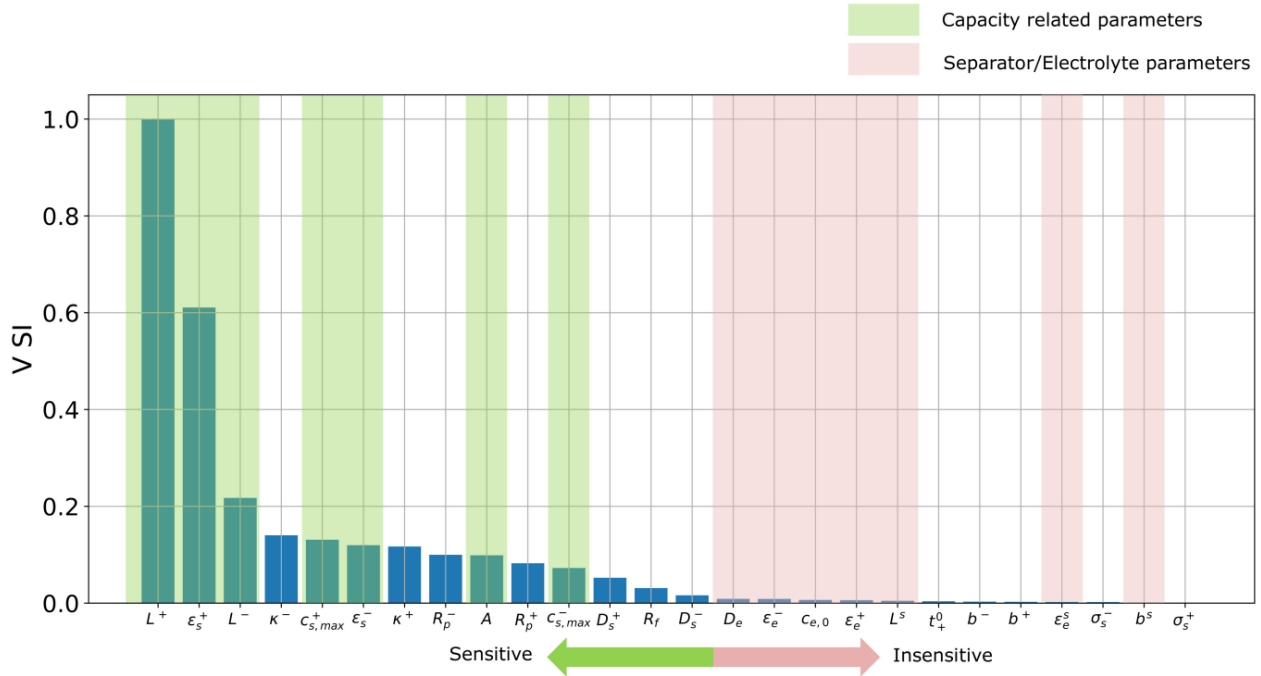


Figure 47: Ranking of the normalized parameter sensitivity for terminal voltage [80].

It is crucial to determine whether these results are also key factors for the model central to this study. Consequently, charging and discharging experiments are simulated in PyBaMM, during which a broad set of parameters (including those selected by Weihaan et al.) are individually varied over a wide range of values. Clearly, all the geometrical parameters measured and previously used to update the model are not modified. It is evident which parameters require optimization due to their significant impact on the model response and which could remain unchanged. Parameters with minimal or no impact retained their initial values from the data set of Mohtat et al., thereby saving computational time by focusing only on the key values.

The key model parameters for which is require optimization are:

- Electrodes active volume fraction.
- Electrodes porosity.
- Electrodes particle radius.
- Electrodes diffusion coefficient.
- Electrodes maximum ion concentration.
- Initial electrolyte concentration.

At this point, the next step is the optimization of the parameters. PyBOP, an innovative open-source package for the parameterization and optimization of battery models, with a particular focus on classes built around PyBaMM models and structures, can effectively serve this purpose.

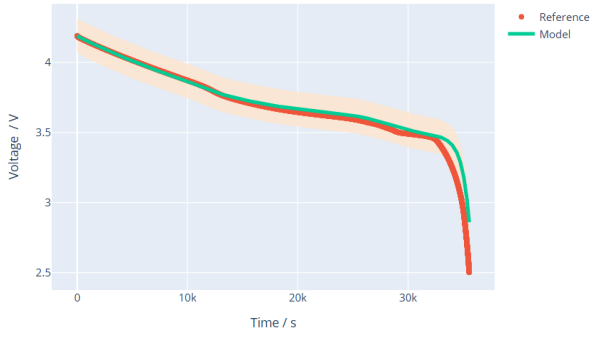
PyBOP presents different optimization algorithms that operate on the same principle: starting from an initial guess of the value of one or more model parameters, the algorithm explores the values within a determined interval to minimize the objective function calculated as the difference between simulated and experimental data. Choosing an optimization algorithm capable of providing the best results is crucial. Consequently, a preliminary optimization process is performed with each algorithm to evaluate their performance in optimizing the parameter values for the intended model, using the available experimental curve as a reference.

For this preliminary optimization, a discharge curve performed at 0.1C is chosen as reference experimental data. The parameters optimized in the process are the electrodes' active volume fraction, with the objective function evaluated as voltage difference between experimental and simulated data.

The results are presented in Figures 48 and 49. As shown, the "*SCiPyMinimize*" method provides the best result in matching the experimental data, minimizing the voltage difference between experimental and simulated data and demonstrating effective convergence of the results to optimal values. Consequently, it is chosen as the optimization method for tuning the model parameters.

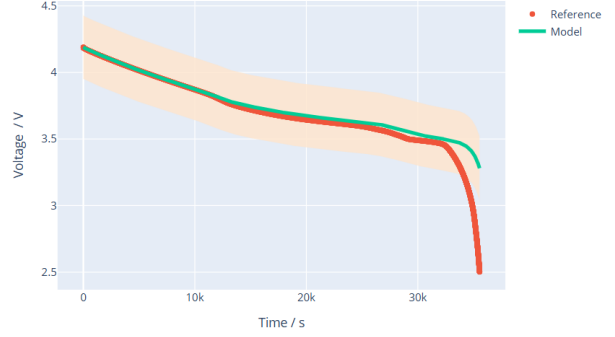
Beyond choosing the best optimization algorithm, there remains an open point that requires investigation. The "ingredients" for a correct optimization procedure are good experimental data, an initial guess of the values, and the range within which to vary the parameter values. The experimental data are available, as well as the initial guess values from the starting literature data set. For the last point, that instead is missing, the study by Weihan et al. [80] is again used as a reference, since it collects the range of values for the parameters intended to optimize. The results, presented in Table 15, are used as a reference for the optimization algorithm.

AdamW



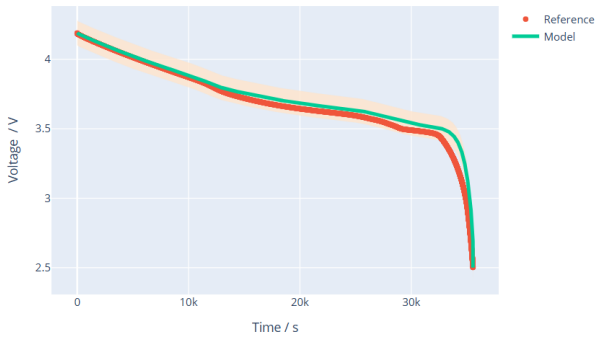
(a) AdamW Method.

iRprop-



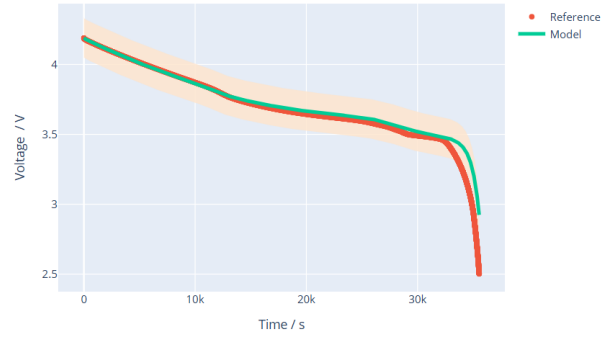
(b) iRprop- Method.

Covariance Matrix Adaptation Evolution Strategy (CMA-ES)



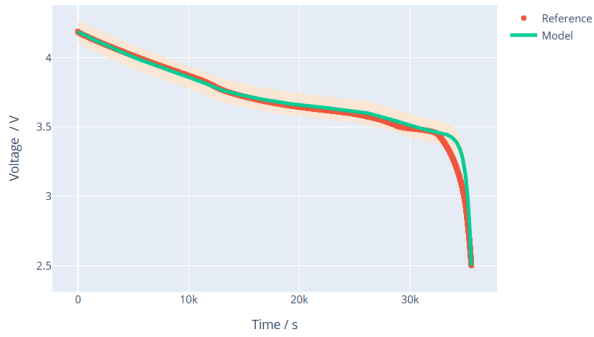
(c) CMA-ES Method.

Particle Swarm Optimisation (PSO)



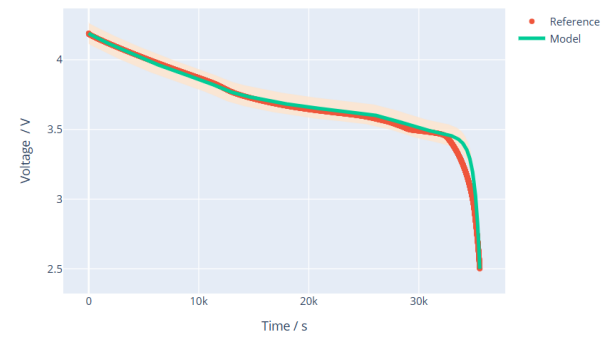
(d) PSO Method.

Nelder-Mead



(e) Nelder-Mead Method.

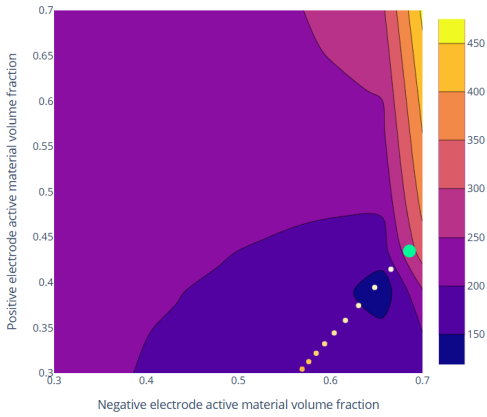
SciPyMinimize



(f) SciPyMinimize Method.

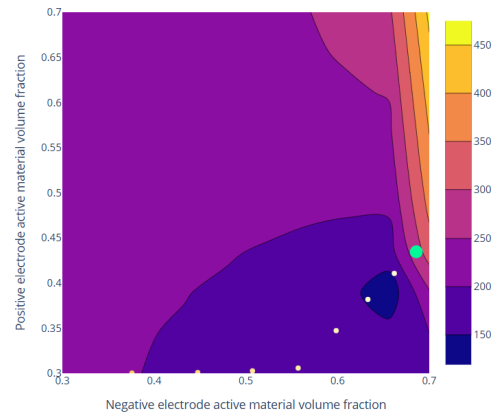
Figure 48: Results of preliminary optimization.

AdamW



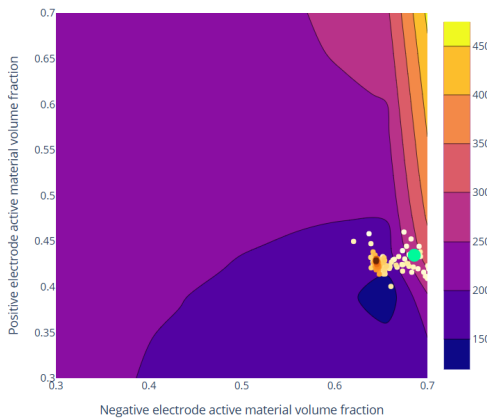
(a) AdamW method.

iRprop-



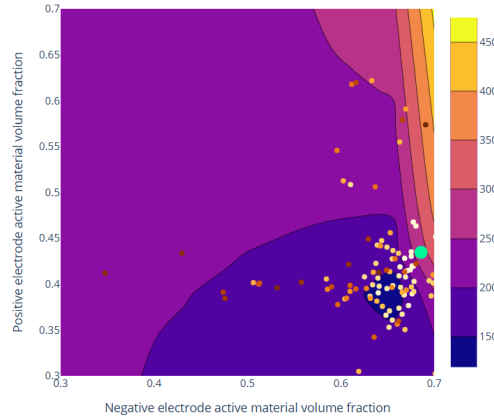
(b) iRprop- method.

Covariance Matrix Adaptation Evolution Strategy (CMA-ES)



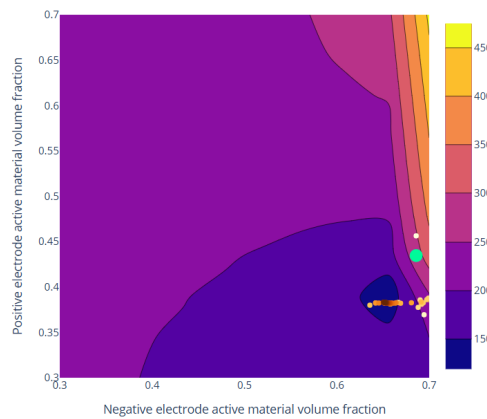
(c) CMA-ES Method.

Particle Swarm Optimisation (PSO)



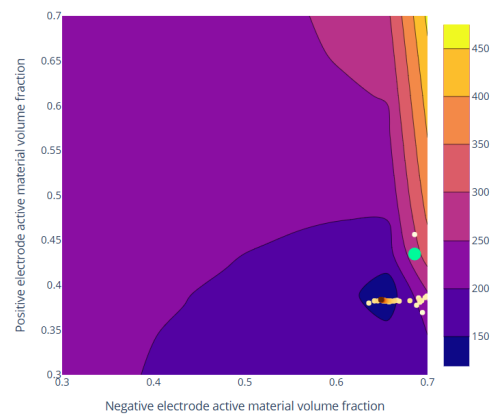
(d) PSO Method.

Nelder-Mead



(e) Nelder-Mead Method.

SciPyMinimize



(f) SciPyMinimize Method.

Figure 49: Objective function cost landscape of preliminary optimization.

Table 15: Range of optimization for the parameter values [80].

Parameter	Unit	Description	Boundaries
ϵ_s^+	-	Cathode active material volume fraction	0.35 - 0.5
ϵ_s^-	-	Anode active material volume fraction	0.4 - 0.7
ϕ_s^+	-	Cathode porosity	0.3 - 0.5
ϕ_s^-	-	Anode porosity	0.3 - 0.8
R_p^+	μm	Cathode particle radius	1 - 11
R_p^-	μm	Anode particle radius	1 - 11
D_s^+	$m^2 s^{-1}$	Cathode solid diffusion coefficient	$1 \cdot 10^{-14}$ - $1 \cdot 10^{-13}$
D_s^-	$m^2 s^{-1}$	Anode solid diffusion coefficient	$1 \cdot 10^{-14}$ - $1 \cdot 10^{-13}$
$c_{s,max}^+$	$mol m^{-3}$	Cathode maximum ion concentration	$2.8 \cdot 10^4$ - $5.2 \cdot 10^4$
$c_{s,max}^-$	$mol m^{-3}$	Anode maximum ion concentration	$2 \cdot 10^4$ - $3.3 \cdot 10^4$
$c_{e,0}^+$	$mol m^{-3}$	Initial electrolyte concentration	$1 \cdot 10^4$ - $1.2 \cdot 10^4$

The optimization process, while seemingly straightforward, is more complex than simply providing experimental data, parameters to optimize, and their initial guesses and ranges. First of all, not all parameters can be optimized simultaneously, as doing so can significantly prolong the process. Optimizing more than three or four parameters at once can cause the algorithm to run for hours without guaranteeing an optimal result. Therefore, a step-by-step approach is necessary, carefully selecting which parameters to optimize together, the sequence of optimization, and the specific experimental data used for each step. Furthermore, even as the optimization process progresses and the data set is updated with optimized parameters, there is no assurance that the model's fidelity will improve; in some cases, it may even degrade.

Consequently, the process of optimization can be defined as an iterative multi-stage algorithm with conditional verification and rollback. In particular:

1. Block-wise iterative optimization: the data set of 10 parameters is divided into blocks of one or two parameters at time. In each stage, one block is optimized by means of SciPyMinimize.
2. Quality verification: after optimizing each block of parameters, it is verified whether the overall system quality has improved according to the voltage difference between simulation and experimental data.
3. Conditional rollback: if the quality has not improved, it is performed a rollback, i.e., it is repeated the optimization (this time an empirical process consisting of varying the optimized parameters in a small range) for the previous blocks, trying to achieve an improvement.

4. Repetition: The optimization process is repeated for the subsequent blocks, always with the possibility of going back if the quality does not meet the desired criteria.

This approach combines sequential optimization with control and correction mechanisms, ensuring that each step forward in the optimization process does not compromise the overall system quality.

Delving deeper into the optimization process, the initial focus is on parameters related to capacity, such as the volume fraction of electrodes, porosity, and initial concentration in the electrolyte. These parameters are primarily optimized using CC-CV charge/discharge curves, which provide a straightforward approach compared to GITT. Following this, the particle radius and maximum concentrations of the electrodes are optimized. This step references both CC-CV charge/discharge curves and GITT to ensure a comprehensive fit. Lastly, transport parameters, including the diffusivity, are optimized with particular emphasis on GITT, due to its sensitivity in detecting transport-related properties.

Figure 50 shows the code for updating the model data set with final optimized parameters values.

```
# optimized parameters
parameter_values_Mohtat2020['Initial concentration in electrolyte [mol.m-3]'] = 1150
parameter_values_Mohtat2020['Positive electrode active material volume fraction'] = 0.4205
parameter_values_Mohtat2020['Negative electrode active material volume fraction'] = 0.64
parameter_values_Mohtat2020['Negative particle radius [m]'] = 6.7e-06
parameter_values_Mohtat2020['Positive particle radius [m]'] = 4.55e-06
parameter_values_Mohtat2020['Positive electrode diffusivity [m2.s-1]'] = 2e-14
parameter_values_Mohtat2020['Negative electrode diffusivity [m2.s-1]'] = 3e-13
parameter_values_Mohtat2020['Maximum concentration in negative electrode [mol.m-3]'] = 21000
parameter_values_Mohtat2020['Maximum concentration in positive electrode [mol.m-3]'] = 33500
parameter_values_Mohtat2020['Negative electrode porosity'] = 0.3
parameter_values_Mohtat2020['Positive electrode porosity'] = 0.45
```

Figure 50: Data set update with optimized parameters.

3.2 Heat production within the cell

After developing an accurate cell model that effectively represents the cell's behavior during charging, discharging, and resting, it becomes essential to evaluate the heat generated under these conditions. PyBaMM offers several thermal sub-models. At present, it includes an isothermal and a lumped thermal model, both of which can be used with any cell geometry, as well as a 1D thermal model which accounts for the through-cell variation in temperature in a pouch cell, and “1+1D” and “2+1D”

pouch cell models which assumed the temperature is uniform through the thickness of the pouch, but accounts for variations in temperature in the remaining dimensions.

Since the cell is be modelled as unique heat power source, it is chosen to use the lumped model, that solves the differential equation for the average temperature. In particular, the sub-model equations, taken from the study of Timms et al. [120], are reported below:

$$\rho_{eff} \frac{\partial T}{\partial t} = \bar{Q} - \frac{hA}{V}(T - T_{\infty}) \quad (37)$$

where ρ_{eff} is effective volumetric heat capacity, T is the temperature, t is time, \bar{Q} is the averaged heat source term, h is the heat transfer coefficient, A is the surface area (available for cooling), V is the cell volume, and T_{∞} is the ambient temperature. An initial temperature T_0 must be prescribed.

The effective volumetric heat capacity is computed as:

$$\rho_{eff} = \frac{\sum_k \rho_k c_{p,k} L_k}{\sum_k L_k} \quad (38)$$

where ρ_k is the density, $c_{k,p}$ is the specific heat, and L_k is the thickness of each component. The subscript $k \in \{cn, n, s, p, cp\}$ is used to refer to the components negative current collector, negative electrode, separator, positive electrode, and positive current collector.

The heat source term is evaluated following what expressed in section 2.2 by Bernardi et al. [12] and accounting for Ohmic heating $Q_{Ohm,k}$ due to resistance in the solid and electrolyte, irreversible heating $Q_{rxn,k}$ due to electrochemical reactions, and reversible heating $Q_{rev,k}$ due to entropic changes in the the electrode :

$$Q = Q_{Ohm,k} + Q_{rxn,k} + Q_{rev,k} \quad (39)$$

with

$$Q_{Ohm,k} = -i_k \Delta \phi_k, \quad Q_{rxn,k} = a_k j_k \eta_k, \quad Q_{rev,k} = a_k j_k T_k \frac{\partial U}{\partial T} \Big|_{T=T_{\infty}}. \quad (40)$$

Here i_k is the current, ϕ_k the potential, a_k the surface area to volume ratio, j_k the interfacial current density, η_k the overpotential, and U the open-circuit potential. The averaged heat source term \bar{Q} is computed by taking the volume-average of Q .

The relevant parameters to specify the cooling conditions are:

1. “Total heat transfer coefficient [$Wm^{-2}K^{-1}$]”
2. “Cell cooling surface area [m^2]”
3. “Cell volume [m^3]”

which correspond directly to the parameters h , A and V in the governing equation.

```
# Thermal sub-model and parameters set-up
options={"thermal":"lumped"}
model=pybamm.lithium_ion.SPMe(options=options)
parameter_values_Mohtat2020 = pybamm.ParameterValues("Mohtat2020")
parameter_values_Mohtat2020["Cell volume [m3]"]=3.67163e-4
parameter_values_Mohtat2020["Cell cooling surface area [m2]"]=4.002066e-2
parameter_values_Mohtat2020['Total heat transfer coefficient [W.m-2.K-1]']=5
parameter_values_Mohtat2020["Initial temperature [K]"]=298.15
# Experiment set-up
experiment = pybamm.Experiment(["Discharge at 10A for 10 minutes",
                                "Rest for 20 minutes",
                                "Discharge at 10A for 15 minutes"])
# Simulation run
sim=pybamm.Simulation(model,experiment=experiment, parameter_values=parameter_values_Mohtat2020)
solution=sim.solve(initial_soc=1)
```

Figure 51: PyBaMM code for SPMe with lumped thermal sub-model creation, data set population and example of a simulation set-up.

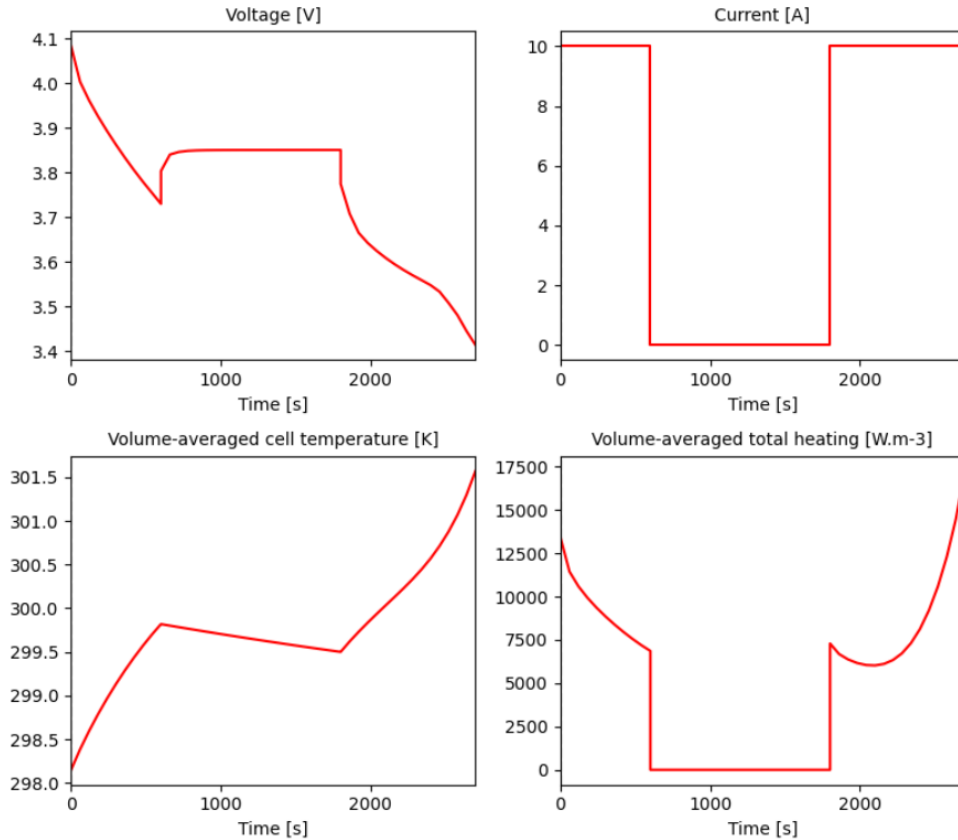


Figure 52: Result of the simulation example.

Figure 52 shows the output of the thermal sub-model for an illustrative example (set up in Figure 51). Beyond voltage and current, the model elaborates, for the given cooling condition expressed by heat transfer coefficient and cooling surface, the resultant temperature evolution and volume-average total heating. This last output is crucial for the implementation of the complete model, since it allows the modelling of the cell as unique absolute power source. However not all the cell volume produces heat, consequently it is necessary to evaluate the volume fraction of the cell effectively involved in the production. This passage will be explained in detail in the model validation, section 4.2.

With a model of this type, capable of applying cooling conditions to calculate cell temperature, implementing a CAD model followed by thermal simulation in specialized software may seem redundant. However, the presented sub-model can only function correctly for a single cell with uniform cooling. Evaluating temperature distribution and heat dissipation in a more complex system, such as the module central to this project, is impractical with this approach. Therefore, it is evident that creating a CAD model of the module itself is necessary. This CAD

model can then be subjected to thermal simulations to assess the module's response to varying heat production and cooling conditions under different scenarios.

3.3 CAD Development

The reproduction of the battery module is carried out in the *Onshape*[®] environment, an open-source software that allows ease CAD implementation and offers high compatibility with the software intended for thermal simulations. The entire module design, particularly the cell and its components, is developed with a focus on feasibility and ability to implement it in thermal simulation environment.

The cell, depicted in Figure 53, is modeled based on the dimensions provided in Table 2 and measurements obtained during the teardown procedure, as reported in Table 14. As evident, if compared to Figure 7a, the cell has undergone several simplifications: a highly detailed CAD model would result in an excessive number of meshes, leading to significantly increased computational time for thermal simulations.

A highly effective, CAD modeling approach was employed by Kleiner et al. [76], yielding successful results in the final thermal simulation. This study adopts a similar methodology while also incorporating the electrolyte, which was not included in Kleiner's research. The specific modeling choices are as follows:

- Electrodes and separator are modeled as a single "jelly roll" body, which serves as the sole heat power source in the thermal simulation.
- Both positive and negative current collectors/tabs are modeled as bodies attached to the jelly roll, simulating the real configuration within the cell. This ensures direct contact between the elements, facilitating efficient heat conduction.
- The remaining space within the case, not occupied by the jelly roll and current collectors, is filled with a volume of electrolyte equivalent to the quantity extracted during the teardown, amounting to 20 mL.

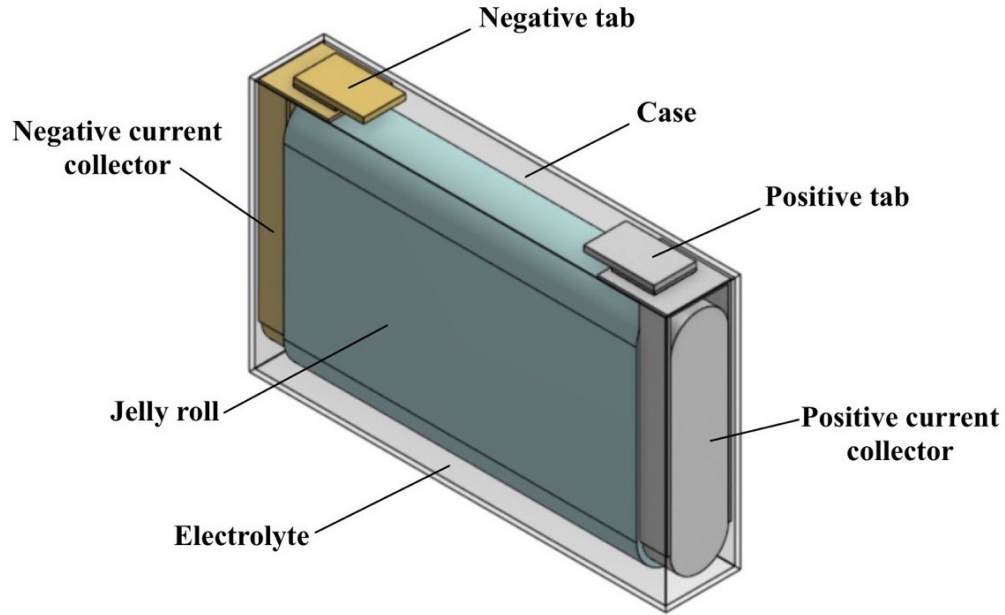
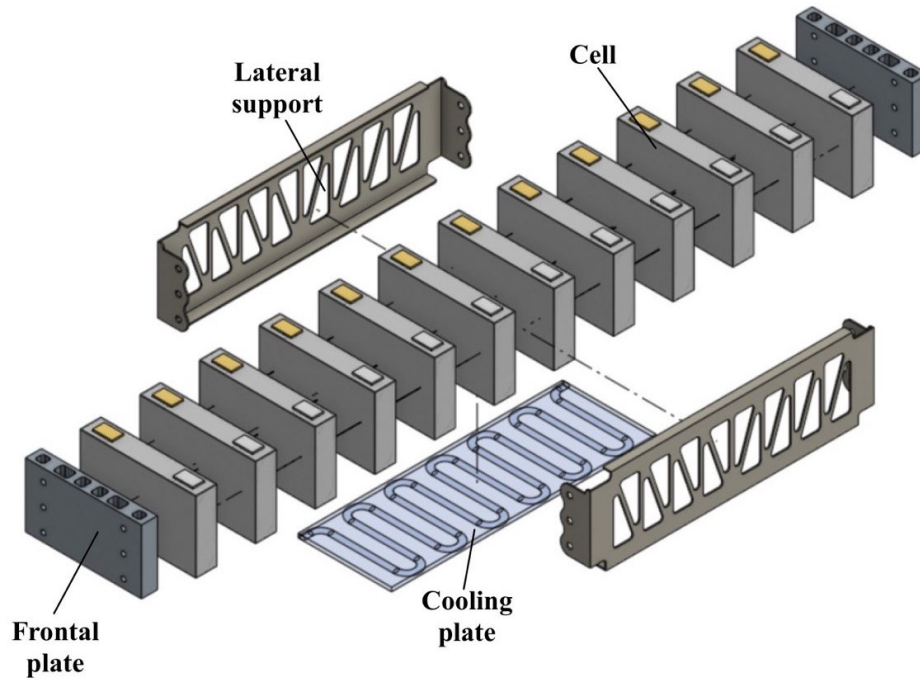


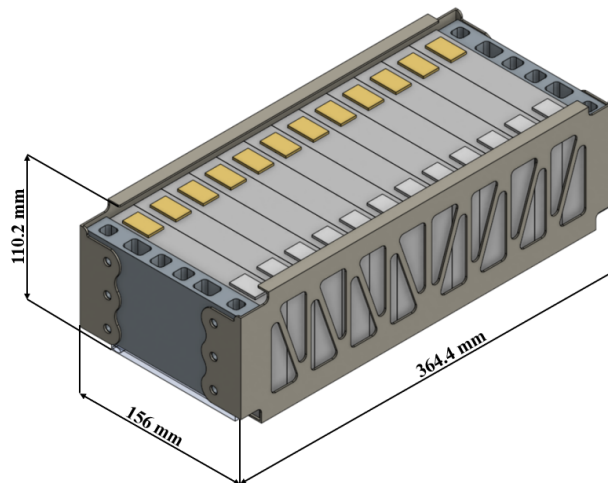
Figure 53: CAD Model of the cell.

The complete battery module, illustrated in Figure 54, is designed based on dimensions empirically derived from the actual module. The CAD model of the cell strikes a balance between fidelity and computational efficiency for thermal simulations. The module is developed with the following considerations:

- The module's core consists of 12 cells.
- Lateral supports and frontal plates serve as the structural components. These components are closely modeled after the real ones, with some non-thermal-relevant details simplified.



(a) Exploded view.



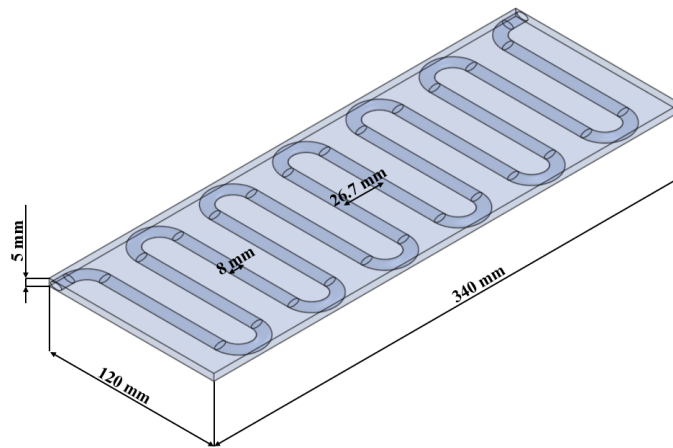
(b) Module size.

Figure 54: CAD Model of the module.

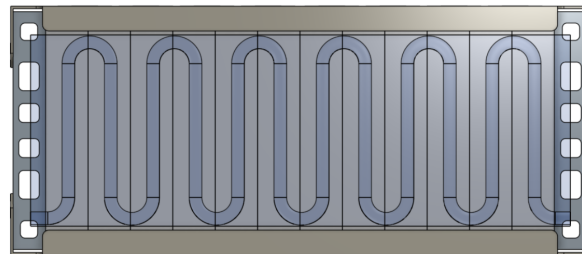
- Depending on the second-life scenario and heat generation, the module may require different cooling systems. Among the presented alternatives in section 2.3, both natural/forced convection and indirect liquid cooling represent viable solutions due to their ease of design and simulation. In contrast, direct liquid and PCM cooling would be effort-intensive to design and overly complex for second-life scenarios. Additionally, the performance of the second system is

significantly inferior compared to indirect cooling, that has the drawback of energy requirement for the refrigerant pump; however, this is a minor issue for typical second-life applications.

When discussing the implementation of the selected systems in thermal simulations, air cooling can be simulated directly within the simulation environment, even with forced convection, without the need for additional components. Liquid cooling, on the other hand, requires a different approach. The module used in this study lacks the water jacket originally employed for vehicle cooling. Moreover, the previous water cooling system was optimized for the vehicle's specific requirements and available spaces. Therefore, a new serpentine cooling plate is designed for this module (Figure 55). The effectiveness of this design has been validated by Jaffal et al. [70], Sun et al. [116], and numerous other studies, highlighting its simplicity, effective cooling capabilities, and reduced pressure drops.



(a) Plate size.



(b) Plate matching with module bottom.

Figure 55: Serpentine cooling plate.

In Table 16 are summarized material and thermal properties of each component of the module, crucial for thermal simulation.

Table 16: Material and properties of module and cell components.

Component	Material	ρ $\left[\frac{kg}{m^3}\right]$	C_p $\left[\frac{J}{kgK}\right]$	λ $\left[\frac{W}{mK}\right]$
Case	Aluminum	2700	900	238
Wet jelly roll [76]	Graphite/NMC/ Polyethylene	2043	1371	in-plane 33 cross-plane 0.7
Electrolyte	LiPF ₆ in EC/EMC/DEC	1250	1850	—
Pos. current coll.	Aluminum	2700	900	238
Neg. current coll.	Copper	8700	385	400
Pos. tab	Aluminum	2700	900	238
Neg. tab	Copper	8700	385	400
Lateral support	Aluminum	2700	900	238
Frontal plate	Aluminum	2700	900	238
Cooling plate	Aluminum	2700	900	238

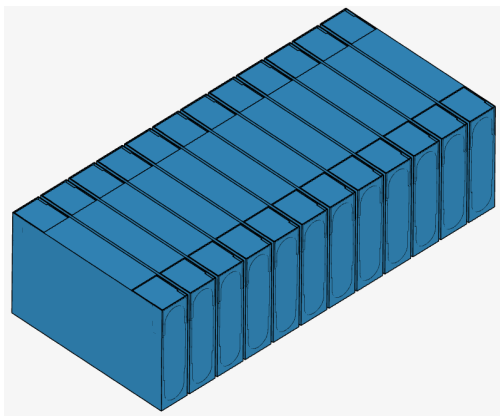
3.4 Thermal simulation

After evaluating the heat produced by the cells and developing the CAD model of the battery module, all necessary elements are in place to advance to the thermal simulation phase. For this purpose, SimScale [56], a cloud-based simulation platform, is selected. This software seamlessly integrates everything required for an end-to-end engineering thermodynamic simulation workflow. Various types of thermodynamic analysis are offered by SimScale. For this study, the "Conjugate Heat Transfer (IBM)" analysis [57] is chosen due to its robustness in simulating flow and heat transfer in complex CAD assemblies.

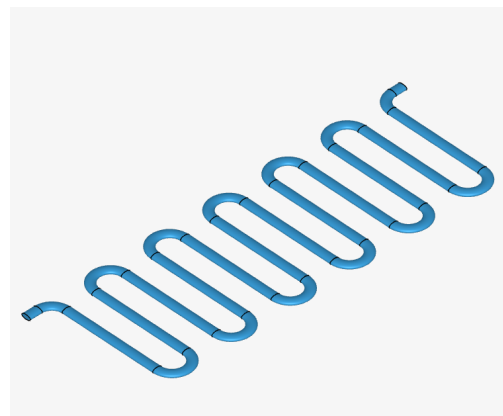
This method solves the same physics as Conjugate Heat Transfer v2.0 but immerses the CAD parts in a Cartesian background grid using the Immersed Boundary Method (IBM). This approach avoids the need to precisely resolve all parts during meshing (body-fitted), making it resilient to irrelevant details that do not significantly impact the overall thermal behavior. Common applications of this analysis type include the simulation of heat exchangers, cooling of electronic equipment, and general-purpose cooling and heating systems.

SimScale provides a user-friendly step-by-step procedure to set up a conjugate heat transfer (IBM) simulation within the platform. The procedure is described in the following points:

1. **Import and edit the geometry in CAD mode.** When performing a Conjugate Heat Transfer (IBM) analysis, CAD simplification is unnecessary because the simulation is resolved in a Cartesian background, avoiding the need to precisely resolve all parts during meshing. Consequently, since the CAD model does not inherently contain the fluid volume, the only task required in this step is the creation of internal flow volumes. This involves creating two different volumes (shown in Figure 56): the first volume fills the interior of the case's cell with the electrolyte, while the second volume (implemented only in simulations with liquid cooling) fills the serpentine of the cooling plate with coolant (blend of water and glycol).



(a) Electrolyte within cell's case.



(b) Coolant within the serpentine cooling plate.

Figure 56: Module's internal flow volumes.

2. **Global setting.** The software enables different features that can be chosen based on application necessities, as shown in 57. In this study, "External flow", "Compressible", "Radiation", "Relative Humidity", and "Joule Heating" are not toggled because their contribution is negligible or not of interest. For the option "Turbulence model", it is selected the k-omega SST solver [58], an in-house version of the widely accepted industry standard turbulence models. For "Time dependency", "Transient" is chosen. This choice is made because it is important to observe not only the convergence of the results but also the step-by-step temperature evolution, particularly in the validation phase.

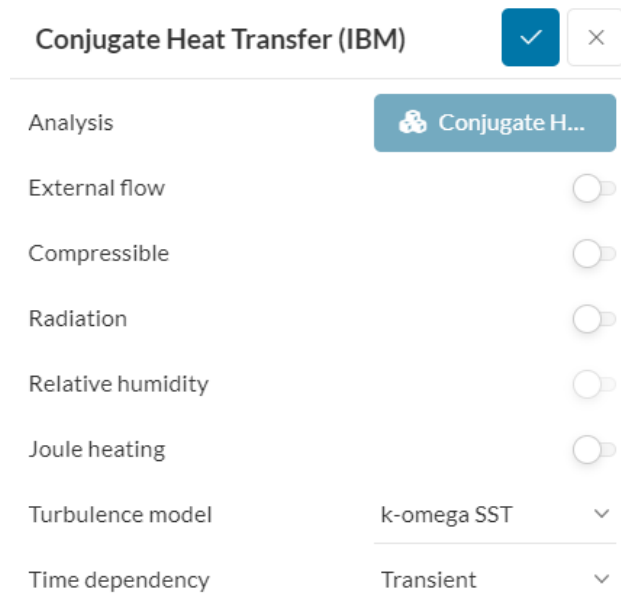


Figure 57: Simulation global settings.

3. **Model.** In this section, the direction and magnitude of gravity are defined. For thermal analysis, it is essential to consider gravity because buoyancy affects the temperature distribution within a fluid. Therefore, a gravitational acceleration of $-9.81m/s^2$ is applied along the z -axis in each simulation, as shown in Figure 58.

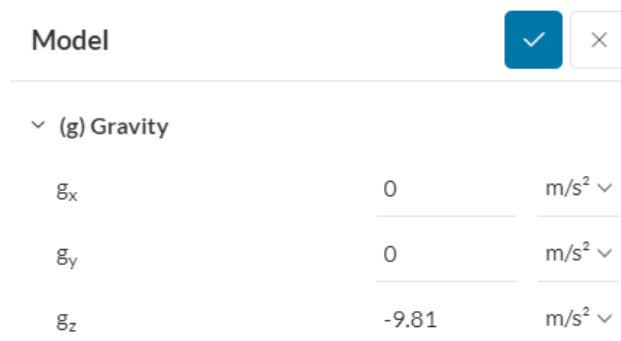


Figure 58: Model gravity.

4. **Materials.** It is crucial to assign specific materials to each element of the geometry to ensure the simulation functions correctly. The software distinguishes between "Fluids" and "Solids" categories. "Fluids" encompass the internal flow volumes, including the water-glycol mixture circulating through the cooling plate and the electrolyte, whose properties are detailed

in Table 16. "Solids" refers to all other elements, with their corresponding material properties outlined in Table 16 as well.

5. **Initial Conditions.** This section requires specifying the initial parameters for the simulation, including "(P) Modified gauge pressure", "(U) Velocity", "(T) Temperature", "(k) Turbulent kinetic energy" and " (ω) Specific dissipation rate". For this simulation, only the temperature needs adjustment and is be set appropriately based on the application. In particular, this feature enables also the setting up of different values assigned to the diverse module subdomains, a very useful option in case the initial temperature of the module components are different.

6. **Boundary conditions.** Boundary conditions are essential for closing the problem at hand by defining the system's interaction with its environment. In this study, two specific boundary conditions are of interest. The first is the "Wall" boundary condition, shown in Figure 59a, which is employed to simulate natural convection scenarios in both validation and second-life application simulations. This condition is applied to all faces exposed to air. The "Heat transfer coefficient" is adjusted based on the convection level: values around 10 W/Km^2 indicate normal convection, lower values suggest limited convection (as applied in the thermal test on the module), and higher values signify increased air agitation, potentially indicating forced convection (as might occur in the second-life application simulation). The external air temperature can also be adjusted according to the specific situation.

The second boundary condition of interest is the "Velocity inlet/outlet", shown in Figure 59b. This condition can be used to characterize the coolant flow within the serpentine, specifying both the flow rate and the temperature of the coolant.

7. **Power Source.** Among all the "Advanced Concepts" available for this type of analysis, this study requires a heat power source. Specifically, the jelly roll of each cell is selected as an "Absolute Power Source" (as also employed by Kleiner et al. [76]). This implies that each element generates the heat power specified under "Power Source Value", as shown in Figure 60. This parameter can accept a CSV file input detailing the heat produced over time. Consequently, this parameter serves as the interface between the thermal model and the thermal simulation, as the heat estimated by the sub-thermal model in PyBaMM is used as input for the thermal simulation.

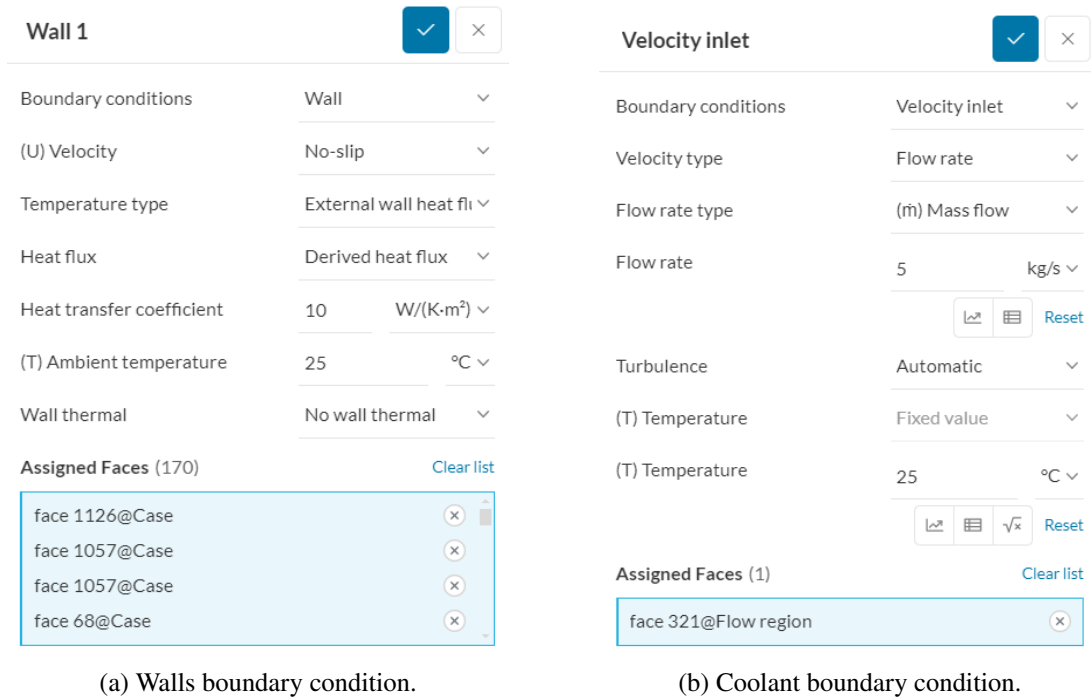


Figure 59: Simulation boundary conditions.

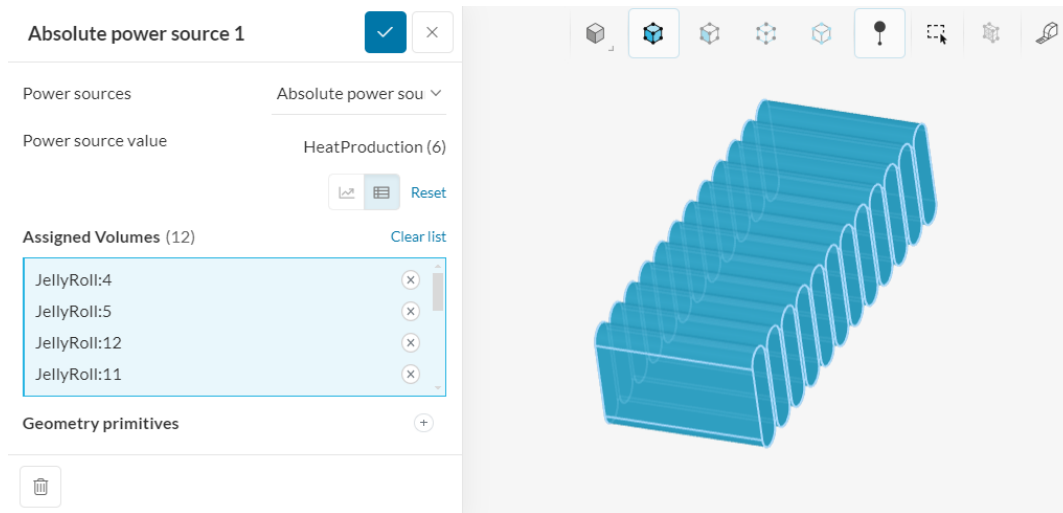


Figure 60: Power sources selection.

8. **Numeric and Simulation control.** "Numerical" settings play an important role in the simulation configuration. They define how to solve the equations by applying proper discretization schemes and solvers to the equations. They help enhance the stability and robustness of the simulation. Although all numerical settings are made available for users to have full control over, the software advises to keep them default unless necessary. Consequently, since there are

not specific requirements for the simulation, the settings are kept untouched.

The "Simulation Control" settings define the general controls over the simulation. In these settings the number of iterations, simulation interval, time-step size, and several other variables are set. The time-step independence will not be investigated in the simulations, due to reduced time and available computational hours.

9. **Result control.** The "Result Control" section enables users to specify additional outputs for simulation results. This section manages the details of result outputs, including write frequency, storage location, and statistical parameters of the data. For these simulations, the primary output of interest is the temperature evolution. Consequently, it is monitored throughout the simulation duration by means of the "Area Average" function, which calculates the average of the scalar result variable over an assigned face. This approximates the temperature evolution of each face of the cell to a unique value. This is a quite reasonable approximation, since the interest of this research is to evaluate the overall thermal performance of the cell/module, not in the temperature gradient of the individual components. Therefore, these metrics are used to validate the model and assess the performance of the battery pack in second-life application simulations.
10. **Mesh.** Meshing is the process of discretization of the simulation domain. That means a large domain is split up into multiple smaller domains and solve equations for them. The Immersed Boundary simulations are based on Cartesian meshes. These do not resolve every part separately as in a body-fitted meshing approach but refine the cartesian grid towards geometrical and topological details and immerse the geometry into it. The above-discussed meshing approach has some strong advantages:
 - Very flexible mesh sizing from very coarse to very fine for all levels of CAD complexity.
 - Automatic defeaturing of small geometrical details.
 - Perfect hexahedral mesh.

Among the three different available methods to define the mesh size, it is chosen the automatic setting that allows to quickly set up mesh by choosing a level of fineness. The range goes from 0 Coarse to 10 fine, with a high number resulting in a finer mesh. The chosen values is 2, as shown in Figure

61 and selected in the application "Cooling of an Electronic Sink" [59], used as reference example.

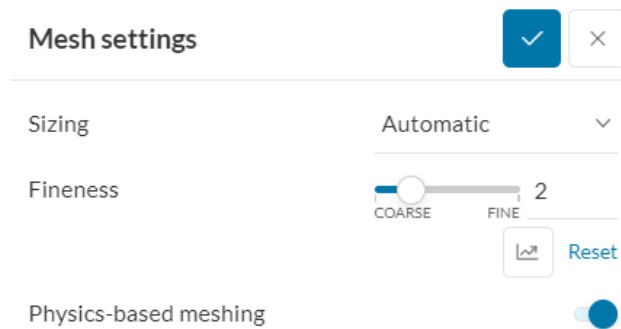


Figure 61: Mesh settings.

3.5 Models coupling

In a previous section, it is explained that the heat produced by a cell, and consequently its internal resistance, depends on SOC, C-rate, and temperature. While the first two parameters are stand alone in the heat production evaluation of the electrochemical model, temperature is not. The relationship between temperature and heat produced highlights a crucial aspect: the interdependence between the electrochemical and thermal models. The thermal model requires the heat produced by the cell as an input, yet this value is determined by the electrochemical sub-model that considers the cell temperature. This temperature, however, is a result of the thermal model's simulation and is heavily influenced by the specific cooling conditions, which vary depending on the application. Given this, it is essential to integrate the two models to ensure they function effectively together, thereby providing the faithful possible outcome.

In section 3.2, the functionality of the thermal sub-model of PyBaMM is described, emphasizing its capability to operate as a standalone thermal model that evaluates temperature only at the cell level across various but uniform cooling scenarios. This is achieved through the parameter "Total heat transfer coefficient", which simulates different cooling intensities. While this parameter has limited usage potential, it can serve as a link between the two models, enabling coupling. Assigning values close to infinity in fact, it allows the cell to instantly adopt the ambient temperature. Unlike the cell temperature, which is calculated by the sub-model, this parameter can be provided as an input.

This establishes the coupling between the electrochemical and thermal models: given a specific duty cycle and starting from an initial temperature, the PyBaMM

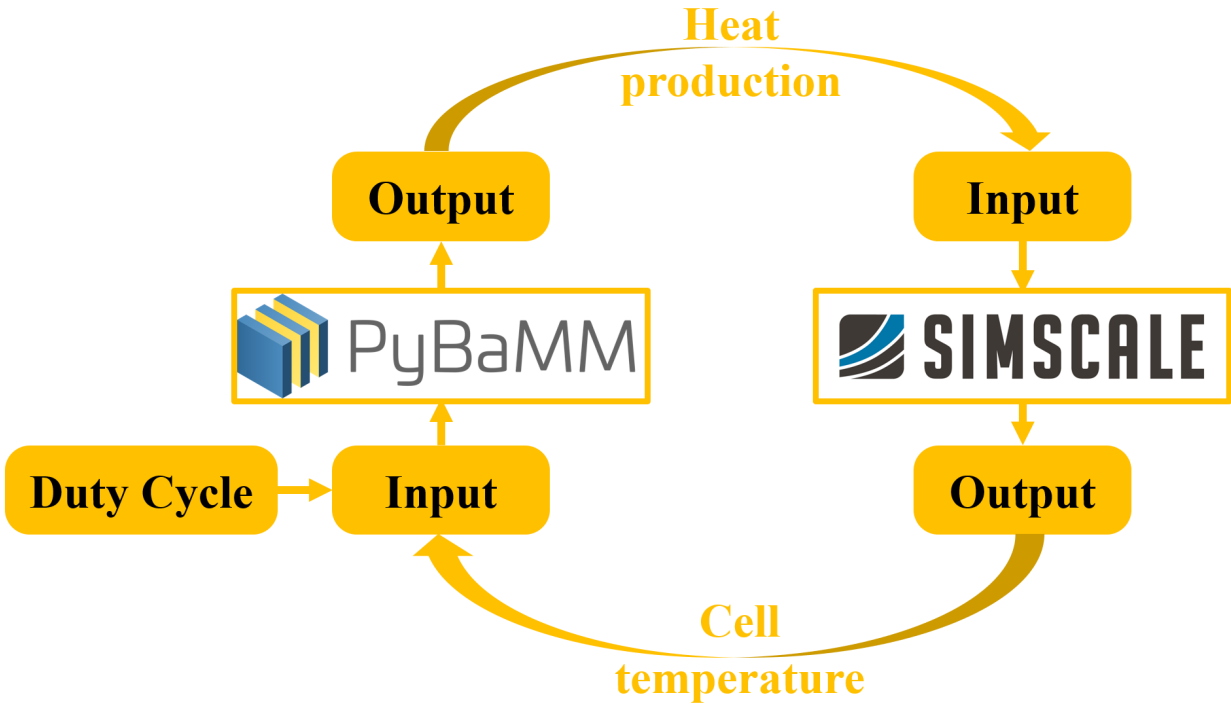


Figure 62: Coupling between electrochemical and thermal models.

model computes the cell’s heat production. This heat production is then used as input for the thermal model/simulation, which, given the boundary conditions characteristic of the scenario (validation or second life application), evaluates the cell temperature continuously throughout the simulation. The resulting cell temperature is fed back into the electrochemical model as the ambient temperature. Due to the near-infinite heat transfer coefficient, this is also be the cell’s temperature. The model then recalculates the heat produced for the same duty cycle, now with updated cell temperature values. The new evaluated heat is again provided as input to the thermal model, creating a feedback loop between the two models.

The iteration loop is stopped when the temperature evolution difference between one thermal simulation and the successive is below a tenth of a percentage point.

3.6 Module thermal test

The coupled electrochemical/thermal model delineated thus far necessitates thermal experimental data for optimization and validation. These experiments must be conducted at the module level to ensure the data aligns with the CAD model and thermal simulations.

As with the teardown and cell cycles, this test was conducted at Accullon Energy™’s laboratory in Columbus, OH.

The premise of this experimental test is straightforward: the module undergoes a complete discharge cycle from 100% to nearly 0% SOC at 30A. Beyond the voltage record of the individual cells, that is added as further validation of the battery model together with dedicated experiment previously conducted, the primary objective of this test is to monitor heat generation during the discharge cycle and the resultant temperature evolution of the cells.

The test is conducted with the module at two distinct initial temperatures: 24°C and high temperature (ranging from 44°C to 48°C depending to the module components), which, as discussed in the subsequent section, represents the reference temperatures for second-life applications.

The experiment set-up is shown in Figure 63. The module is placed in an adiabatic styrofoam chamber maintained at 23°C for both tests. This chamber is employed to ensure the module remains in a controlled environment with a nearly constant temperature and limited heat exchange.

Sixteen thermistors are utilized to monitor the temperature evolution of the cells/module with a resolution of 1 °C. The record is done not only during the discharge from 100% to 0% SOC of the module, but also in the rest/cooling period. This latter record will be fundamental to choose the proper heat transfer coefficient within the adiabatic chamber, allowing also the successive estimation of the cell volume fraction producing heat.

Table 17 details thermistor's placement on the module, partially shown in Figure 64. The focus is primarily on the cell located in the middle of the module, which is subject to the least heat exchange.

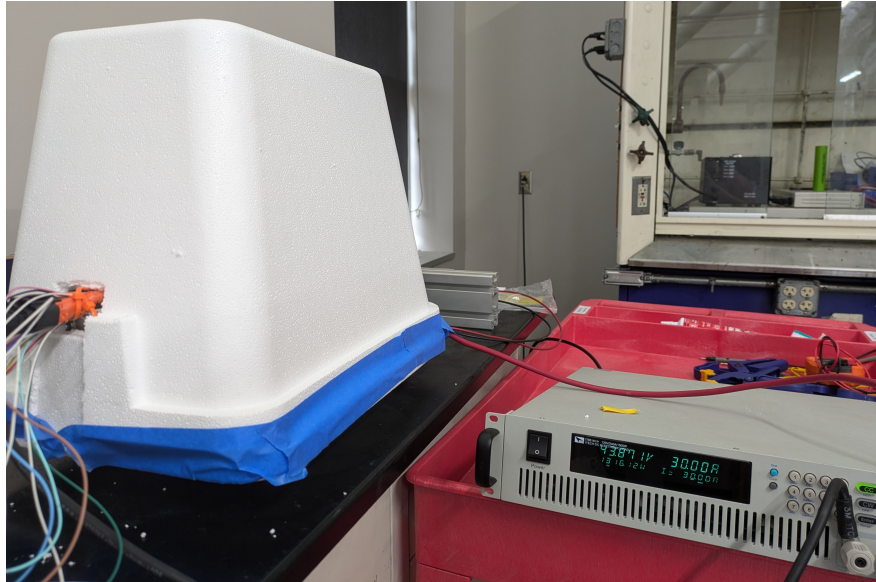


Figure 63: Module within adiabatic styrofoam chamber.

Consequently, seven thermistors are placed: three on the top of this cell (one for each terminal and one corresponding to the vent), one on each side along the module length, and two at the bottom to verify temperature uniformity in that area. This higher number of thermistors is used both for redundancy and to evaluate temperature differences in various areas of the same cell. As imaginable, it is not feasible to place thermistors on the other side of the cell due to their stacked configuration.

Additionally, two thermistors are placed at the bottom of the cell in contact with the front plate (theoretically subject to more heat exchange) and two at the bottom of the cell positioned between the aforementioned cells. These measurements facilitates a comparison of the temperature evolution of cells exposed to different heat transfer coefficients.

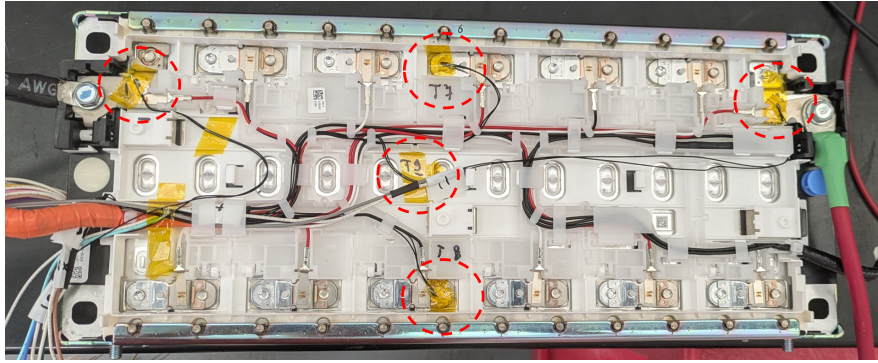
The remaining thermistors are placed on the module terminals (despite not being modeled in the CAD and thus not implemented in the thermal simulation) and in the styrofoam chamber.

Table 17: Thermistors position.

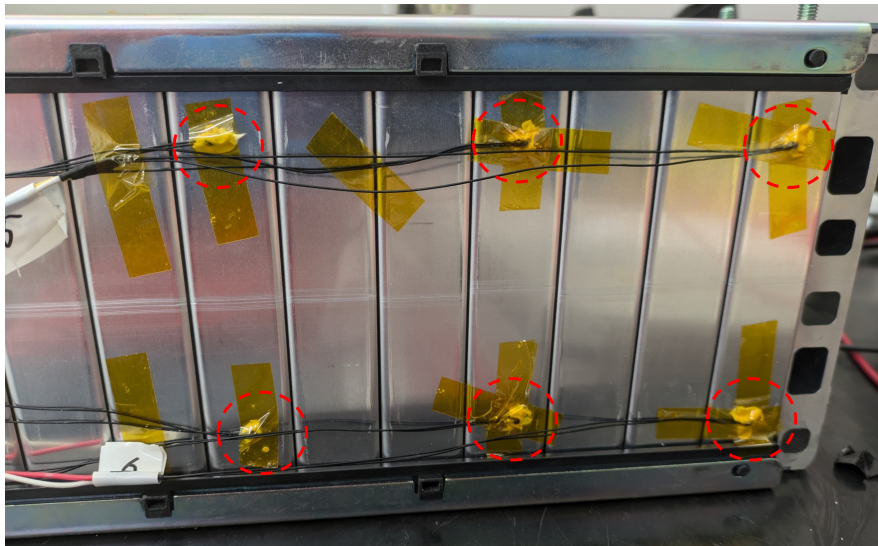
Thermistor	Position	Thermistor	Position
1	Cell 6 Bottom	9	Cell 6 Vent
2	Cell 6 Bottom	10	Cell 6 Side (Neg. Term.)
3	Cell 9 Bottom	11	Module Pos. Term.
4	Cell 9 Bottom	12	Module Neg. Term.
5	Cell 12 Bottom	13	Cell 6 Side (Pos. Term.)
6	Cell 12 Bottom	14	Chamber Top
7	Cell 6 Pos. Term.	15	Chamber Bottom
8	Cell 6 Neg. Term.	16	Ambient Temperature

Note: The cell numbering corresponds to their positions within the module. Cell number 6 is located at the centre of the module, cell number 12 is adjacent to the frontal plate, and cell number 9 is situated in between.

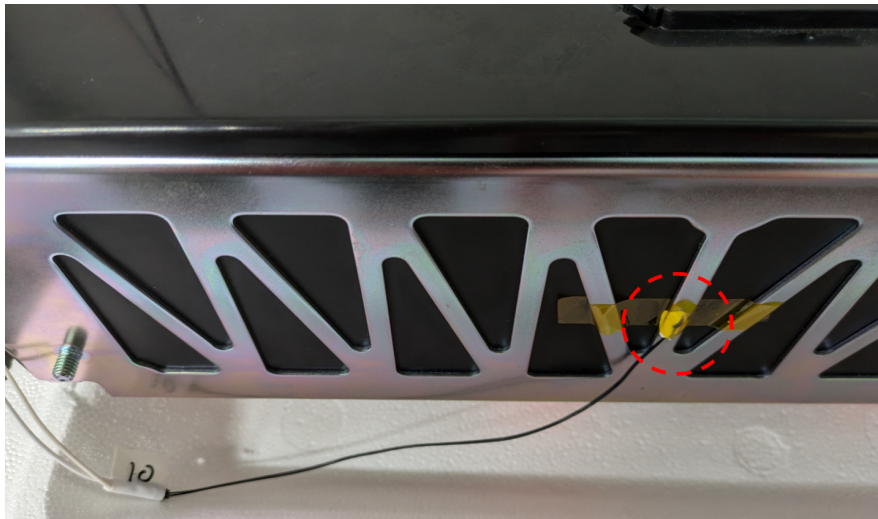
The experimental test enables a comprehensive validation of the coupled electrochemical/thermal model. With this final element, the modeling related to the cell/module is complete. Consequently, the next step is the evaluation of the most suitable second-life scenarios for the battery, followed by corresponding simulations and application assessments.



(a) Top view.



(b) Bottom view.



(c) Side view.

Figure 64: Thermistors set-up on the module.

3.7 Second life applications

As discussed in section 2.8.5, SLBs are viable for a wide range of applications. However, it would be impractical to investigate performance and thermal suitability of the HONDA CLARITY module in every potential second-life scenario. Micheline et al. [93] reviewed the majority of available opportunities for lithium-ion batteries post-first life usage, selecting eight promising applications. These were chosen based on their relevance in the scientific literature and feedback from expert interviews. The applications were then graded on a scale from zero to eight based on charging and discharging rates, required capacity, temperature range, and degree of mobility, with higher marks assigned to applications that better preserve the battery's life during its second usage.

While this study provides valuable insights, it does not solely determine the selection of second-life applications for testing the module. Indeed, the target of this part is to select applications that ensure battery longevity and good performance, but also to demonstrate that, with proper design, appropriate boundary conditions, and effective cooling strategies, the module can perform excellently in various scenarios, including the most challenging ones.

Consequently, the chosen applications are:

- Renewable solar firming: rated 7, for renewable energy storage purposes.
- ESSs for domestic PV: rated 7, for residential energy storage purposes.
- Electric forklifts: rated 5, for industrial purposes. Despite its lower grade compared to other applications, it is included to test the module in a more demanding scenario, due to the mobility feature and higher discharge requirements.

Each application will undergo a thorough analysis of its operational characteristics, utilizing a representative duty cycle selected from established literature. This step will be crucial for gaining insights into the actual performance demands placed on the battery. Understanding these demands will enable the determination of number and configuration of modules required for the new battery pack. Additionally, estimations of the maximum discharge rate, capacity, and volume and weight requirements, where applicable, will be made.

Furthermore, the boundary conditions of each application will be examined, with particular attention to the operating temperature and potential cooling strategies. These strategies will be guided by the forecast heat production under the selected duty cycles. This comprehensive analysis, followed by the design of the battery

pack and its cooling system, will be essential for meeting the requirements of each application while respecting the thermal characteristics of the battery.

3.7.1 Renewable solar firming

Functioning

The goal of renewable solar firming is to maintain a stable power output by compensating for fluctuations in renewable energy generation. This mechanism is realized by ESSs by discharging power during periods of insufficient renewable generation and absorbing power when generation surpasses a certain threshold. The threshold is usually determined based on the forecasted nominal renewable power generation for the given period. This process typically spans multiple hours to ensure a steady power supply. Thus, the ESS addresses the forecast uncertainty in actual renewable generation during this time frame.

A critical distinction between PV firming and PV smoothing is the duration over which the ESS operates. PV smoothing aims to limit the ramp rate of power output and mitigate negative impacts on the grid caused by the variability of PV power output. This involves applying ESS power over short intervals, ranging from one second to one minute. In contrast, PV firming focuses on stabilizing power output over longer durations, ranging from 15 minutes to several hours. The objective of PV firming is to create a composite power output that more closely resembles a consistent block of energy with desired upward slopes, magnitudes, downward slopes, and total duration, as specified by the grid operator [112].



Figure 65: PV plant with its ESSs [44].

Reference duty cycle

The duty cycle for this application is a charge / discharge profile that represents the demands placed on the ESS in order to firm PV power output. The cycle was realized by Schoenwald et Ellison [112] to accurately measure and express the performance of ESS in solar firming application. The data used for such study were taken from the Public Service Company of New Mexico's Prosperity Electricity Storage Project ("PNM Prosperity") [38]. PNM Prosperity consisted of 500 kW/350 kWh batteries, integrated with a 500 kW solar photovoltaic resource. The resultant duty cycle, presented in Figure 66 represents a challenging and yet realistic signal.

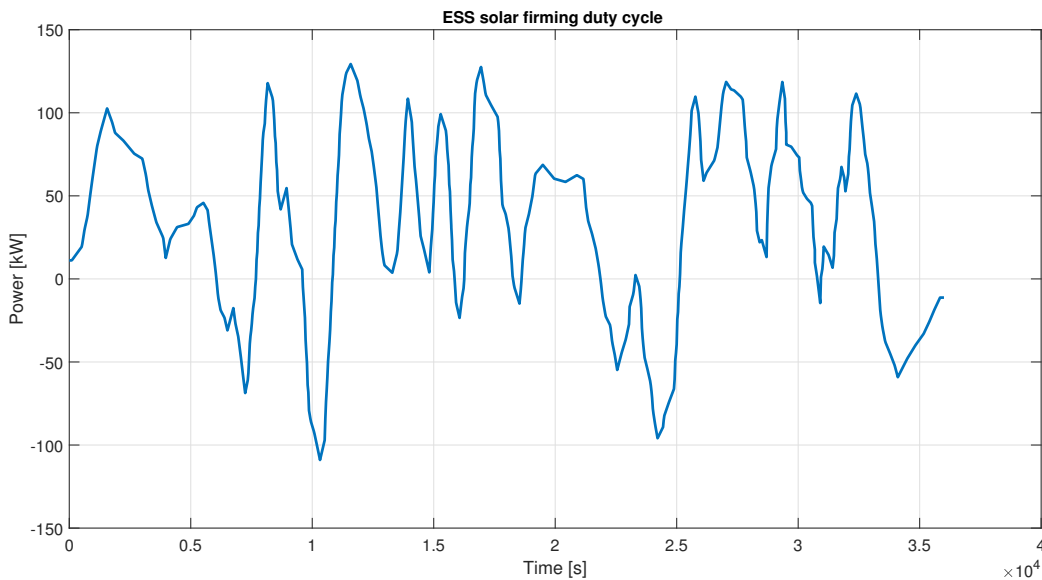


Figure 66: Duty cycle signal for renewables solar firming application [112].

Operating conditions

The plant's capacity requirements are equal to 350 kWh. Therefore, the ESS would necessitate 294 HONDA CLARITY's modules. Each cell will have a maximum power request of 142W, with a maximum discharge rate of 0.4C. The architecture of the "PNM Prosperity" operates at 1000V, leading to an ESS configuration of 21 modules in series and 14 modules in parallel (21S14P).

Given that large photovoltaic installations are typically located in very sunny and hot environments, it is reasonable to expect the same conditions for the ESS used for firming. For this application, a surrounding temperature of 45°C is assumed. Considering the discharge rates, which do not exceed 0.4C, both natural and forced

air cooling could serve as effective and safe cooling strategies.

For this application there are no requirements regarding weight and volume.

3.7.2 ESS for PV domestic application

Functioning

ESSs are essential in residential PV production systems, significantly enhancing energy flexibility, efficiency, and reliability. SLBs can be employed in this scenario for peak shaving, by storing excess energy generated during high production hours for use during low production or high demand periods, and load shifting, by storing energy during off-peak hours when electricity rates are lower and discharging it during peak hours. This maximizes self-consumption of renewable energy, reducing carbon footprint of the energy production sector and increasing household energy autonomy. Additionally, ESSs can easily provide a backup power supply during grid outages, ensuring the operation of critical appliances and systems, thereby enhancing energy security.

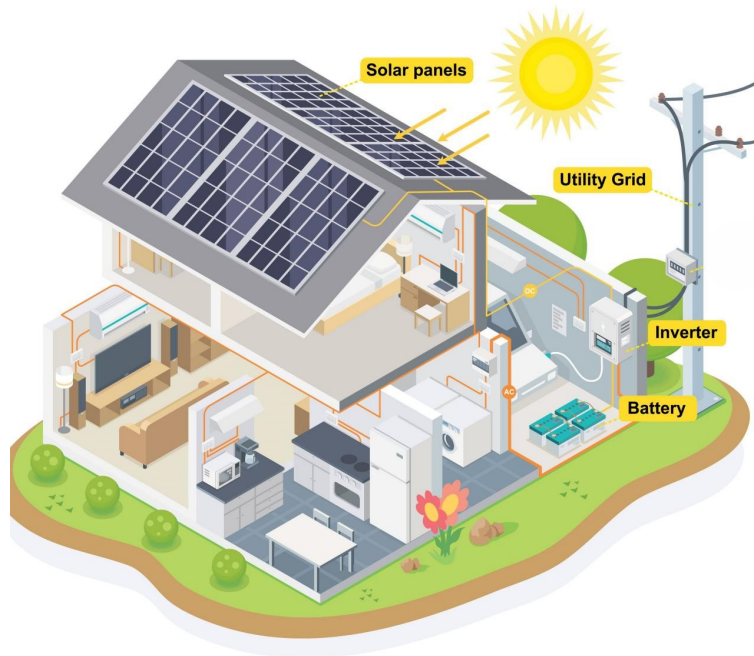


Figure 67: PV and ESS in a residential application [55].

Reference duty cycle

The high flexibility and wide range of operating conditions of an ESS makes challenging the identification of an unique, representative and unambiguous duty

cycle. For this reason, it is decided to test the battery module in a challenging operating scenario: a day in which the autonomous PV production system, coupled with the ESS, provides most of the energy required by all the domestic devices.

Hou et al. [41] collected important data in this field. Figure 68 shows PV generation data of a single residence during a sunny summer day. Thanks to a smart home energy management method, it is possible to optimize scheduling plan of domestic appliances. Figure 69 shows that domestic appliances complete their tasks in the corresponding operation time slots, and non-interruptible appliances also guarantee the operation continuity. Most appliances operate when the PV output is high. In addition, PV generation is used to meet the consumption of appliances, and then to provide charging energy for ESS. With this method of optimization, it is provided not only a reasonable and economical work plan for domestic appliances, but also maximized RES and ESS utilization. The resultant duty cycle of the ESS is reported in Figure 70.

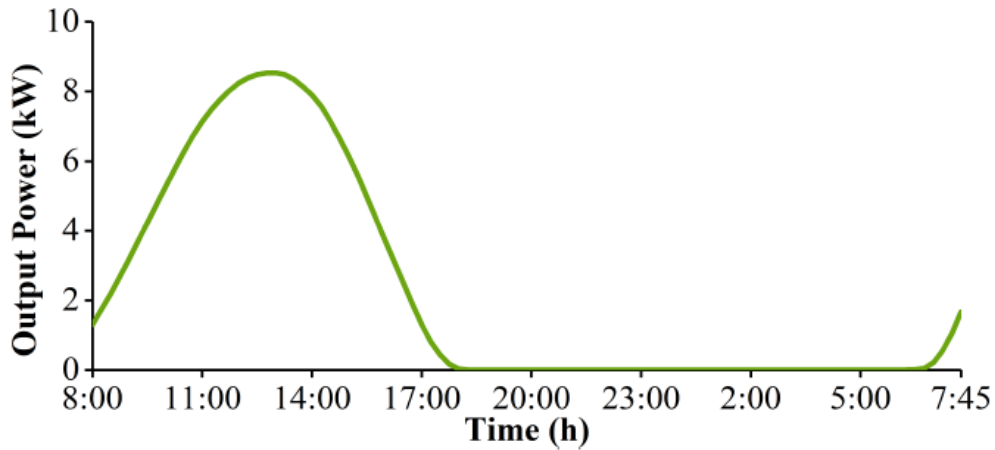


Figure 68: PV generation in summer [41].

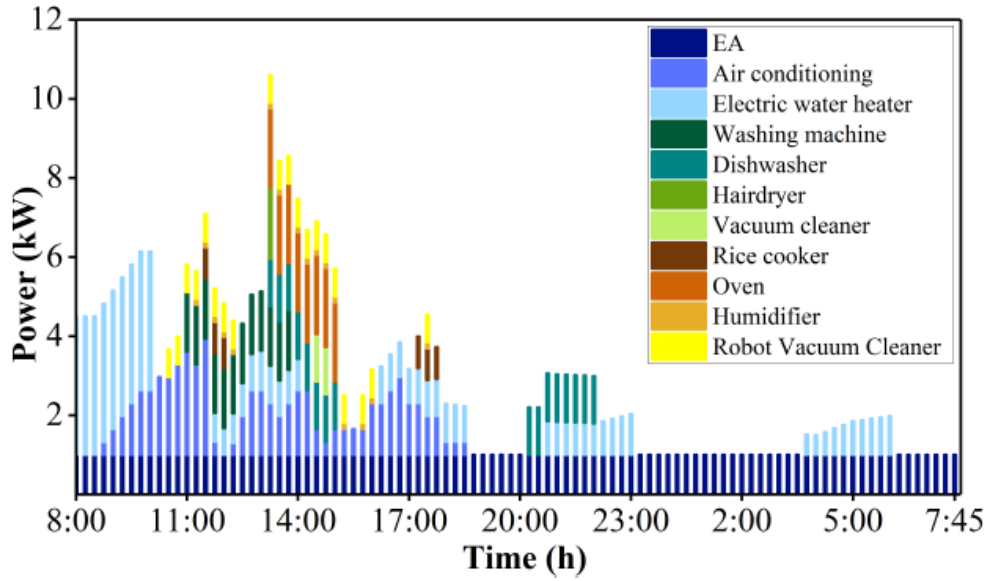


Figure 69: Scheduling plan for domestic appliances [41].

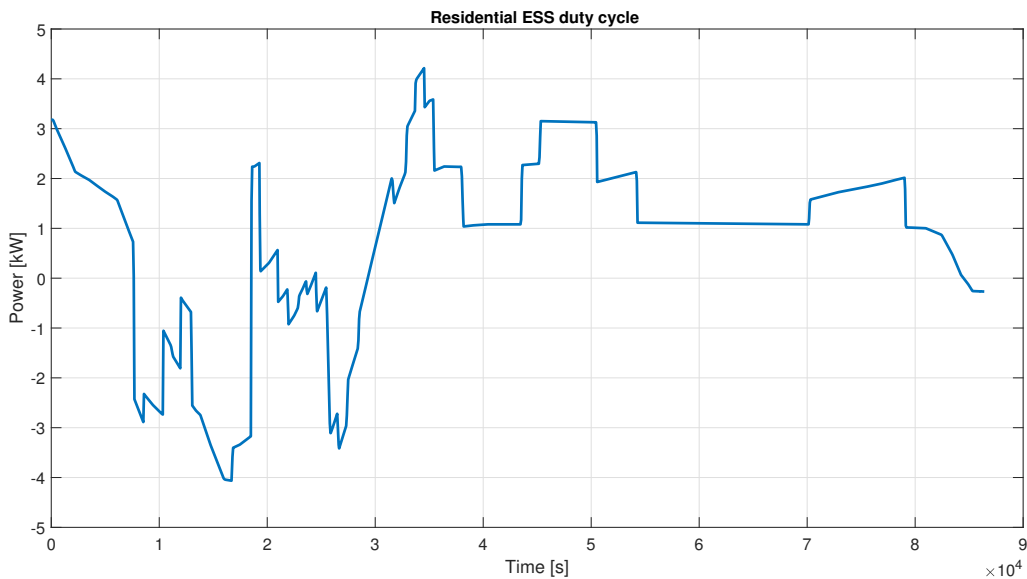


Figure 70: Hypothetical charging and discharging power of ESS under optimal scheduling.

Operating conditions

The required capacity of a domestic ESS is primarily determined by the maximum installed power of the photovoltaic system. It would be worthless to have an excess energy storage capacity if the PV system's power is insufficient to charge it fully. In this case, the installed power is 8.5 kW. For dimensioning the ESS, the ECS2900-H4 model from *FOX ESS* [49], a leading ESS manufacturer, is selected. With an

appropriate number and configuration, the HONDA CLARITY's modules align well with this model and meet all application requirements. Specifically, the necessary architecture comprises ten modules arranged in a 5S2P configuration. This setup results in a total capacity of 12 kWh with a maximum discharge rate of 0.3C.

ESSs can be installed either outdoors or indoors. However, in most cases, in order to protect it from adverse weather conditions, it is typically placed indoors. Therefore, for this application, a constant ambient temperature of 25°C, akin with a domestic environment during summer, is assumed. Additionally, given the maximum discharge rate of 0.3C and the forecast low heat production, natural convection should be sufficient to ensure proper thermal management and safe operating conditions.

Since this is a stationary application, weight is not a significant consideration. Generally, volume is not a primary concern either, but since the installation is indoors, it is roughly considered in this study. The ECS2900-H4 model occupies a volume of 0.13 m³. In comparison, using 10 modules of the HONDA CLARITY, with size shown in Figure 54, the total occupied volume would be less than half of that, amounting to 0.06 m³.

3.7.3 Electric forklift

Functioning

Electric forklifts have become essential machinery in modern industrial operations, valued for their efficiency, versatility, and environmental benefits. Powered by advanced battery systems, these forklifts offer a clean and quiet alternative to traditional internal combustion engine models. Their superior energy efficiency is evident through enhanced energy conversion rates and the ability to recover energy during braking phases, which would otherwise be wasted in conventional forklifts. Electric models are particularly well-suited for indoor environments such as warehouses, manufacturing plants, and distribution centers due to their lack of pollutant emissions and reduced noise levels.

Advancements in battery technology have significantly increased the diffusion of electric forklift, by means of extended operational hours, enabled rapid charging, and improved overall performance. These developments make electric forklifts a reliable and sustainable choice, even in demanding applications such as material handling and logistics, where they previously faced challenges.



Figure 71: Electric forklift [62].

Reference duty cycle

Vadlamudi et al. [121] synthesized a duty cycle for an electric forklift with a driving motor of 10 kW and lifting motor of 12 kW. The duty cycle, reported in Figure 72, represents a classical operation of a forklift, characterized by the motors activation, load approach, lift, transport and release, followed by a new movement towards another load.

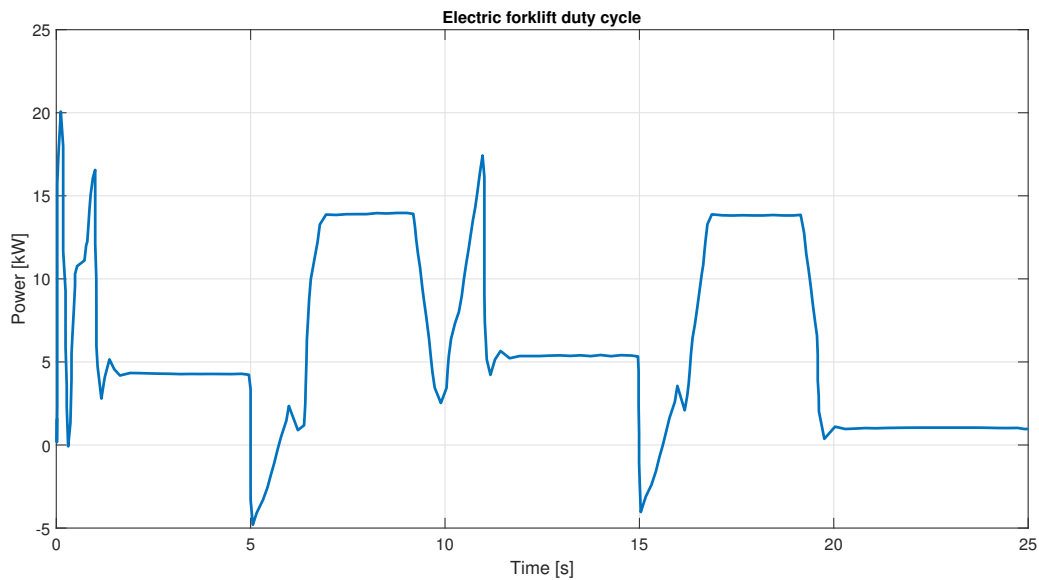


Figure 72: Total power drawn from storage system during an hypothetical forklift's duty cycle [121].

Operating conditions

The required capacity for the battery pack of an electric forklift is determined by the power demands of the driving and lifting motors. Therefore, the Toyota TRAIGO48 1.5t [61], which matches the performance of the forklift used in the duty cycle, is chosen as a reference for dimensioning. This model uses a 48V architecture, analogous to the HONDA CLARITY module, and requires a capacity of 440Ah. Consequently, the battery pack configuration will be 1S16P, resulting in a total capacity of 19.2 kWh with a maximum discharge rate of 1C.

Small-sized electric forklifts, like those considered in this application, typically operate indoors where the temperature is around 25°C. The battery pack is usually housed in a bay under the operator's seat, where air convection may be insufficient to provide proper cooling. Given the maximum discharge rate of 1C and the anticipated higher heat production compared to previous applications, a liquid cooling system be employed. To test under challenging conditions, bottom cooling is the sole method used, simulating an adiabatic environment within the battery enclosure.

Unlike the previous stationary applications, this mobile application imposes constraints on both weight and volume. The TRAIGO48 is again the reference for these requirements. The available volume in the battery bay is 0.15 m³. Sixteen modules of the HONDA CLARITY, accounting for their size and the space needed for the cooling system and cabling, occupies 0.12 m³. Therefore this requirement is completely fulfilled. The weight of the battery pack is crucial for maintaining a low center of gravity, ensuring safe lifting and movement of loads. Therefore, there is a minimum weight requirement for the pack but no maximum. In the Toyota forklift model, the pack weighs 700 kg, whereas the pack with HONDA CLARITY modules weighs only 200 kg. Thus, additional ballast should be collocated in the remaining volume of the battery bay, in order to fulfill the minimum weight requirements.

Table 18 summarizes the characteristics of the designed battery pack in the different second life applications.

Table 18: Battery pack characteristics in second life applications.

Application	Firming	RES	Forklift
Configuration	21S14P	5S2P	1S16P
Operating Voltage [V]	1008	240	48
Energy [kWh]	352.8	12	19.2
Maximum C-rate [C]	0.4	0.3	1
Weight requirements	No	No	Yes
Volume requirements	No	Yes	Yes
Cooling type	Air	Air	Liquid
Operating temperature [°C]	45	25	25
CO₂ Saving [29] [t]	37.4	1.2	2

4 Results

4.1 Electrochemical model

In this section are presented all the results concerning cell experimental tests, SPMe behaviour and its capability in matching the data pre and post the optimization algorithm.

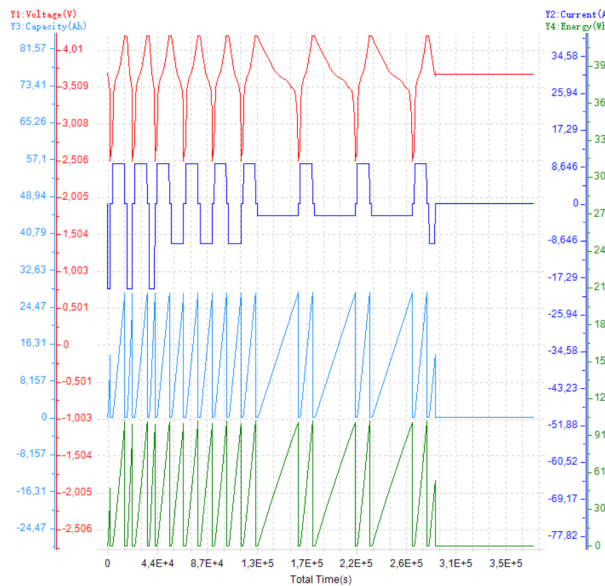
4.1.1 Experimental data

This section presents the results of the experimental tests conducted on the cell, following the procedure outlined in section 3.1.3. The data from the cycler are analyzed using BTSDA Neware post-processing software, which displays not only the current employed during the cycle and the corresponding cell voltage response, but also the discharge energy and capacity.

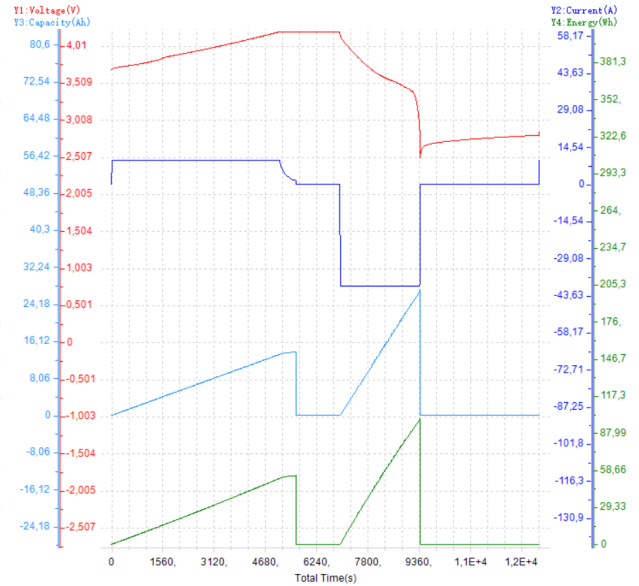
Figures 73a and 73b illustrate the CC-CV charge and CC discharge cycles. In this test, the current is varied from 0.1C to 1.5C while maintaining a constant temperature of 25 °C.

In addition to the voltage response, which remains within the limits specified in the datasheet for each cycle type, the plots provide valuable information about the actual capacity of the cell. Despite slight variations depending on current intensity, both discharge capacity and energy values align with the datasheet specifications, confirming the cell's performance. Specifically, the cell demonstrates approximately 27Ah of capacity and 103Wh of energy.

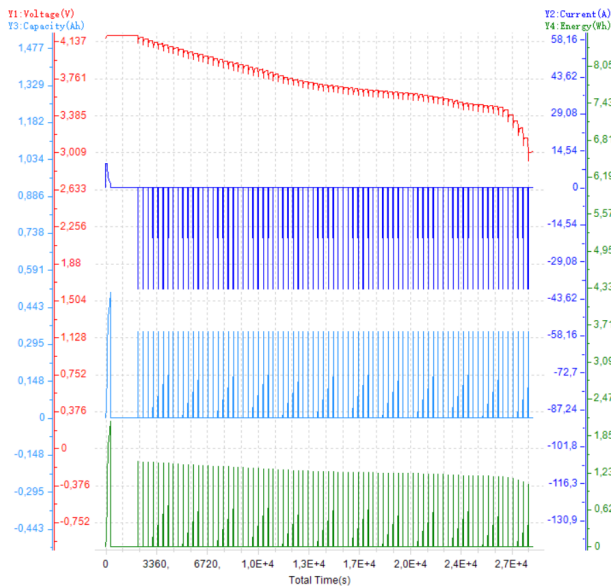
Figures 73c and 73d display the GITT curves. This test consists of 80 discharge pulses at 40A, each followed by a 5-minute rest period. Although less straightforward to interpret than the previous test, this protocol provides insights into the cell's characteristics by probing the entire state of charge range at two different temperatures: 25°C and 45°C. The graphs reveal higher resistance at high and low SOC values, which decreases at intermediate levels. Additionally, as expected, the cell exhibits lower overall resistance and improved efficiency at the higher temperature of 45°C.



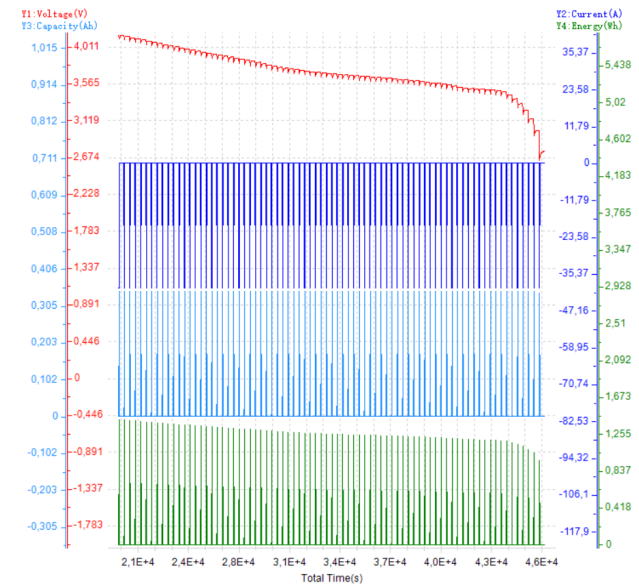
(a) CC-CV Cycles between 2.88A and 20A at 25°C.



(b) Single pulse discharge at 40A and 25°C.



(c) GITT with 80 pulses at 40A and 25°C.



(d) GITT with 80 pulses at 40A and 45°C.

Figure 73: Results of experimental tests on the cell.

4.1.2 Pre-optimization model results

This section illustrates the response of the SPM_e in matching the experimental data prior to updating the model with optimized parameters. Consequently, the results presented in Figure 74 reflect the model's fidelity using only the initial part of the data set updating procedure. This includes parameters derived from the datasheet and geometrical measurements obtained during the teardown, while all

other parameter values remain as in the original data set from Mohtat.

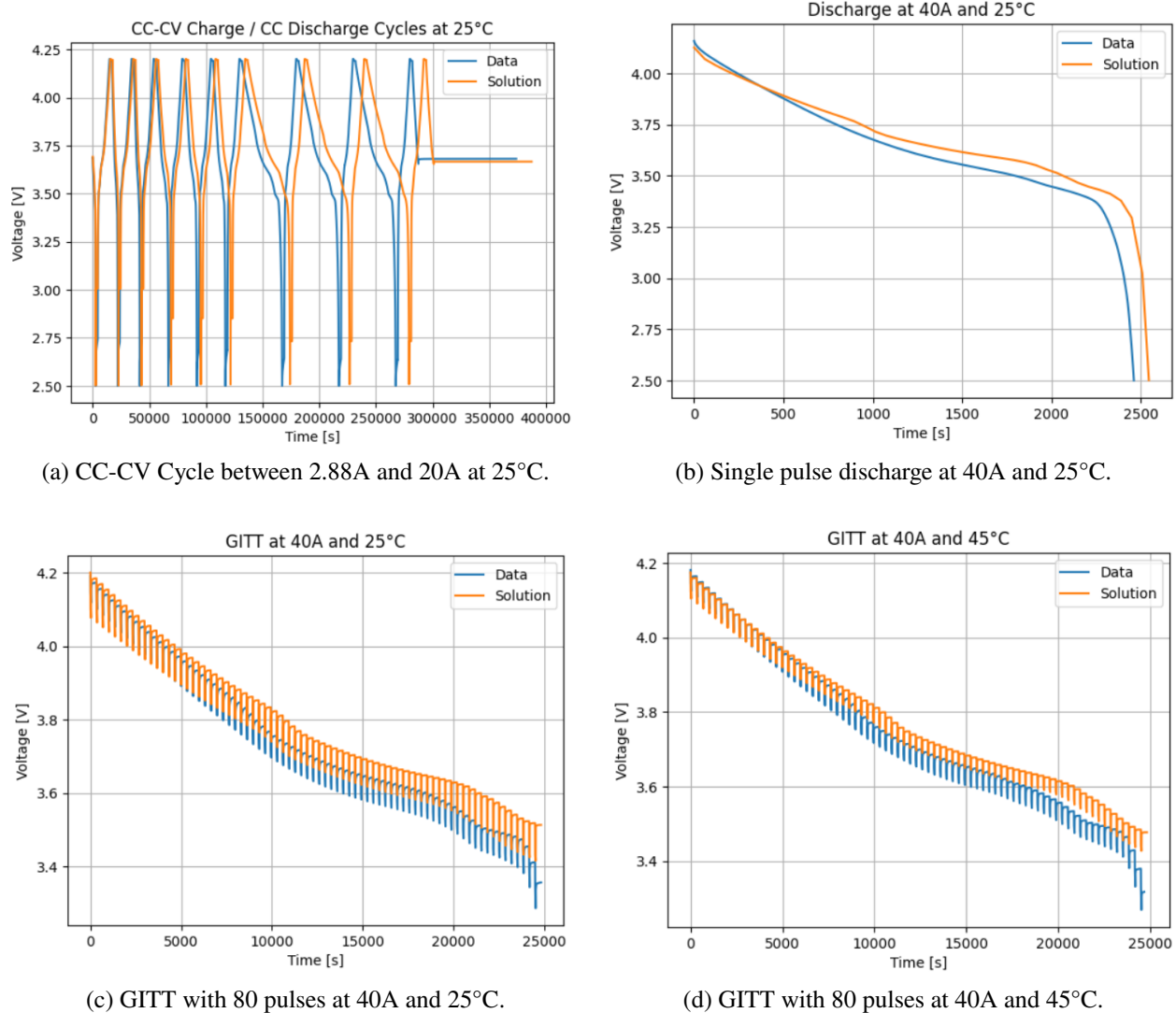


Figure 74: Model match of experimental data before optimization.

The overall results reveal the need for model improvement, regarding both the capacity and kinetic parameters. The model is not capable of following properly the CC-CV cycles, shown in Figure 74a, since it diverges from the experimental data after three discharge/charge cycles. The reason can be attributed to the overestimation of cell capacity, well evident in Figure 74b. This is confirmed also in the reproduction of the GITT tests in Figures 74c and 74d, where, after a satisfying match in the first part, the model is not able to follow the behaviour of the curves, due to evident different capacity and dynamic.

Despite these flaws, the model demonstrates positive aspects, such as the good shape of the curves that closely resemble the experimental data. Additionally,

the simulations conducted at higher temperatures already indicate lower overall resistance. These two points highlight the potential of the model, even at this incomplete stage.

4.1.3 Post-optimization model results

This section illustrates the capability of the SPM_e in matching the experimental data after the optimization and update of the key parameters outlined in section 3.1.3.

For a more detailed analysis of the model response in fitting the CC-CV Charge / CC Discharge cycles, the experimental discharge curves are extrapolated and singularly analyzed in increased current intensity in Figure 75.

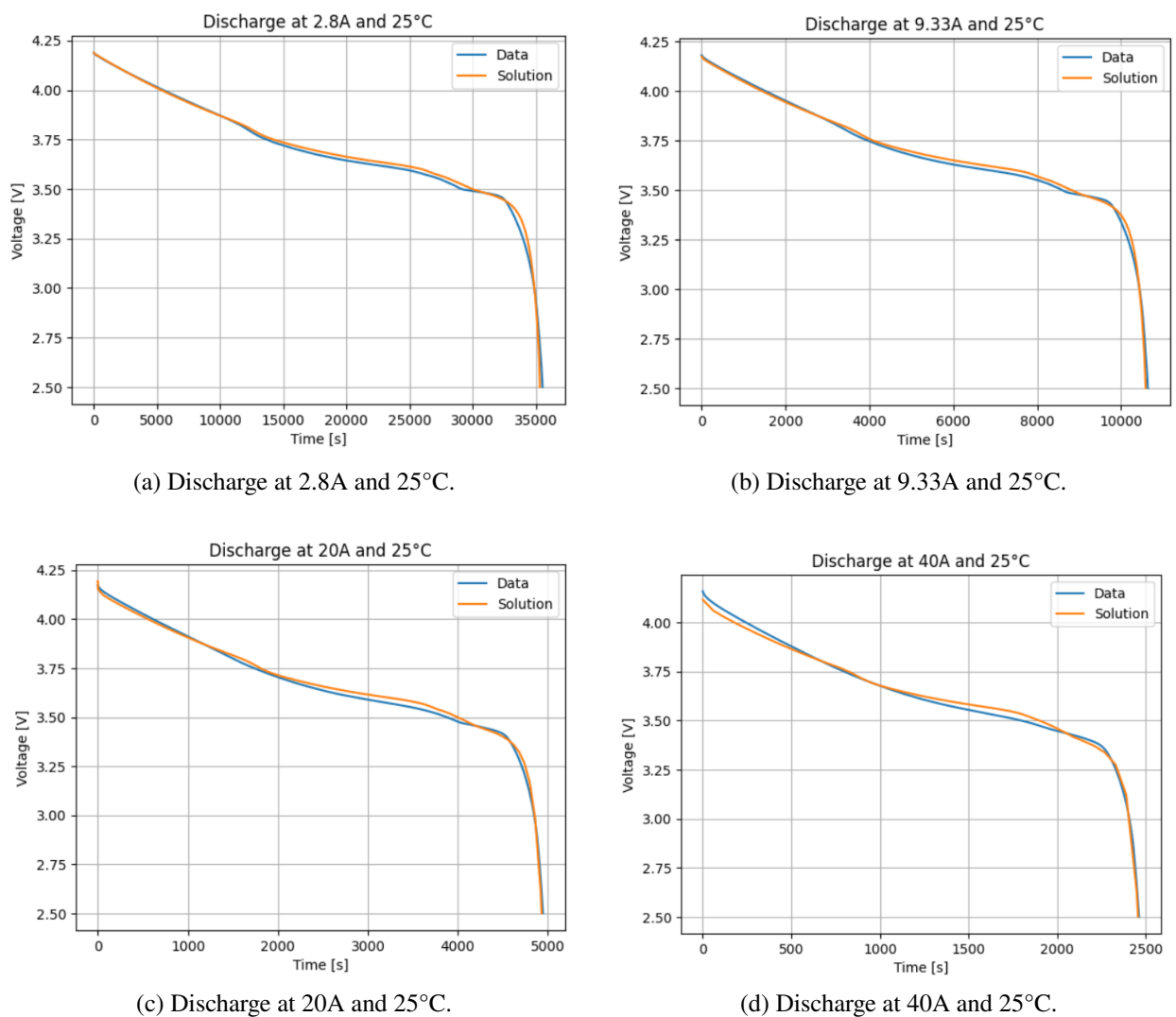


Figure 75: Model match of experimental discharge curves after optimization.

It is well evident from the graphs the model predicts cell behaviour and capacity

with high accuracy across all different current intensities. This marks a significant improvement over the incomplete model presented in the previous section.

Despite that, the model encounters minor challenges in predicting the cell dynamics, especially within the voltage range of 3.75V to 3V. Although the overall shape of the curves is comparable to the experimental data, there is a slight overestimation of voltage within this window.

This discrepancy becomes more pronounced with increasing current intensity, reaching a voltage error of nearly 20mV at 40A discharge. Additionally, for C-rates higher than 0.6C, the model starts undergoing minor fluctuations also at the beginning of the cycle. Several factors could contribute to this behavior, including ohmic polarization, concentration polarization, electrochemical kinetics, and mass transfer. These phenomena exhibit highly nonlinear characteristics at elevated current intensities, which may not be adequately captured by the SPMc.

Nonetheless, this does not pose a significant limitation, as the model is intended to represent the cell in second-life scenarios, where current intensities rarely exceed 1.5C. Therefore, the model's accuracy should suffice to ensure proper safety in voltage evaluation and, consequently, in heat production estimation.

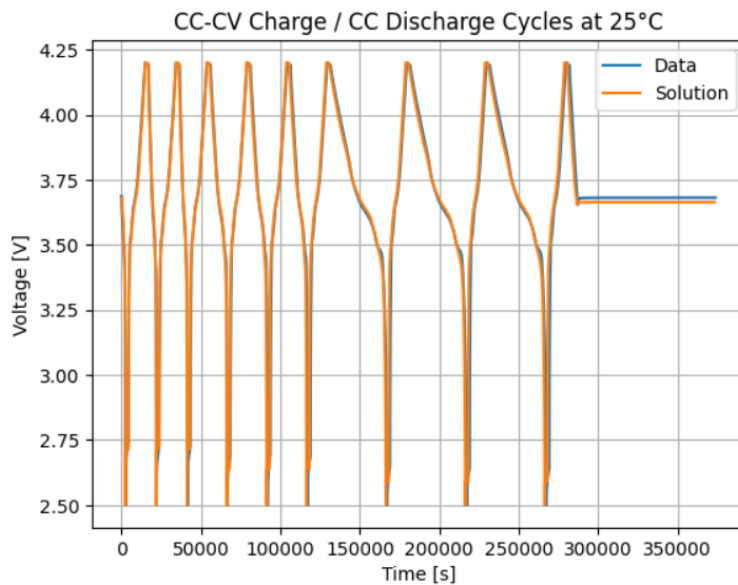


Figure 76: Model match of experimental CC-CV charge/CC discharge curves after optimization.

Figure 76 demonstrates the alignment of the optimized model with the complete test of CC-CV charge and CC discharge cycles. Compared to the unoptimized model, this updated curve shows significant improvement. This plot is particularly relevant as it illustrates the model's capability to accurately replicate the cell's

behavior over an extended period, unlike some models that only perform well with short experimental data. The optimized model successfully matches the cell's performance over more than 11 hours, underscoring its reliability across a variety of conditions.

Up to this point of the analysis SPMe results, all the matching of the model regarded experimental test and simulation conducted at ambient temperature. As expressed several time in this thesis in fact, due to limited test resources, only one experimental test involved a temperature different from the standard conditions. The GITT curve are consequently the only one in which is possible to appreciate the accuracy of the model with different temperature of the cell.

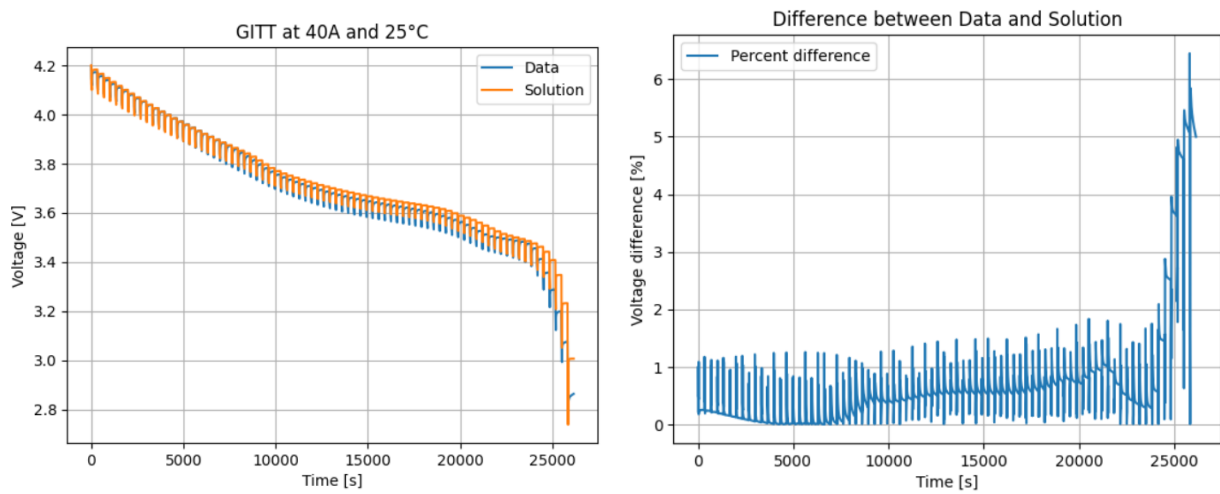


Figure 77: Model match of GITT at 40A and 25°C.

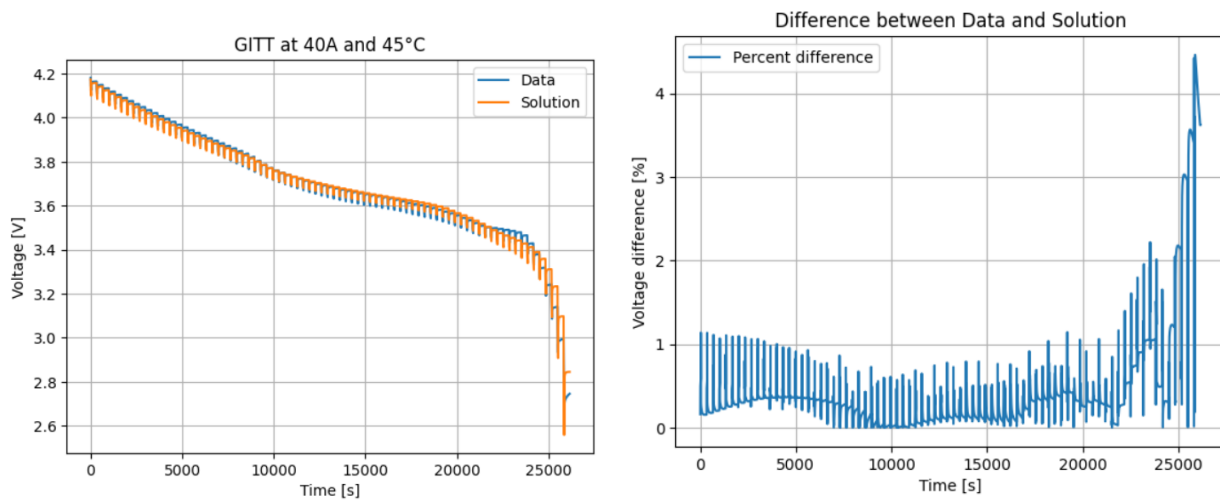


Figure 78: Model match of GITT at 40A and 45°C.

Examining Figures 77 and 78, it is possible to evaluate the model's fidelity in replicating the two GITT curves resulting from 80 pulses, each 31 seconds long, with 5 minutes of rest, at 40A and at temperatures of 25°C and 45°C. These curves present a particular challenge due to their high dynamism and extended duration, but also for the difficulty in optimizing the behaviour for all the test duration. This implies that the model response is a compromise of accuracy between the first, the middle and the last part of the cycles.

The most notable improvement post-optimization is the model's enhanced ability to follow the trajectory of the experimental data, whereas previously, the simulation diverged significantly from the experimental results.

The overall accuracy of the model is evident across a wide SOC range for both simulations, with a percentage between 0.5% and 1.5%. However, a drastic and sudden error increase (especially in the test at room temperature) is observed in the final stages of the test simulations, when the remaining SOC is approximately around 5%. This drastic decrease in modeling accuracy could be attributed to unmodeled non-linear characteristics. Such phenomena would need to be analyzed in detail by means of dedicated and deep experimental tests. Clearly with the available resources it was not possible to further and better investigate this aspect.

Nonetheless, the overall level of accuracy of the model aligns with the thesis's objective, ensuring good accuracy for the majority and most experienced SOC ranges in both the simulations.

Regarding the model's sensitivity to temperature variations, further insights can be drawn. Firstly, the model effectively captures the resistance differences due to temperature changes. It shows a decrease in resistance at 45°C compared to 25°C. Additionally, the model demonstrates better accuracy in matching experimental data at the higher temperature. At room temperature, the average model error ranges between 1% and 1.5% for most of the test (reaching around 6% at the test's end). At 45°C, the error is significantly lower, ranging between 0.5% and 1% and reaching 4% only at the end of the simulation. This notable improvement indicates the model's capability to provide more detailed results in scenarios characterized by high temperatures due to increased heat production or limited cooling.

After the validation of SPM_e, the next step is the discussion of the results obtained in the thermal tests conducted on the module. In this way, both the coupled models will be validated, ensuring an effective simulation of the module in the chosen second life scenarios.

4.2 Coupled electrochemical-thermal model

In this section are illustrated the outcomes of the experiments and simulations concerning the coupled electrochemical-thermal model. This includes the results of the thermal experiments conducted on the battery module, followed by the comparison with the simulation results, outcome of PyBaMM thermal sub-model and thermal simulations in SimScale.

4.2.1 Thermal experimental results

This section presents the results of experimental tests conducted on the module, as outlined in section 3.6. The temperature evolution data is recorded by thermistors with resolution of 1°C and plotted against time. Additionally, also the voltage profiles of the module cells during the discharge phase are recorded and plotted.

In order to allow a clearer visualization of the results, three plots are created for each simulation:

- The first graph presents the data from all thermistors installed on cell 6, located centrally within the module. This cell is subjected to minimal heat exchange, which potentially leads to the highest temperature rise.
- The second graph illustrates the temperature evolution at the bottom of three distinct cells. This plot facilitates an effective comparison of the temperature dynamics among cells positioned at various locations within the module, each experiencing different heat exchange conditions.
- The third graph displays the thermistor records monitoring the chamber, encompassing the ambient temperature as well as the temperatures at the top and bottom of the styrene box containing the battery module.

The first experiment offers simpler analysis and simulation compared to the second. All the module components and even the walls of the adiabatic chamber, start from an initial temperature of 24°C . The air inside the chamber has initial temperature equal to 23°C . Due to this simplicity, the plots can be divided into two distinct areas: from the beginning to approximately 3200 seconds, the temperature evolution is due to module discharge at a current of 30A. Successively, the decrease of the temperature is due to a rest period in which, the module undergoes a cooling period for the remaining 6800 seconds.

These records are essential for validating and refining the coupled model. The cooling phase enables the estimation of the module's heat transfer coefficient within

the styrene box, which is critical for the SimScale simulation. With this data, the discharge phase can be used to determine the value of the cell volume fraction responsible for heat generation, unknown during the creation of the PyBaMM thermal sub-model.

Now it is possible to analyze more in detail the experimental results shown in the first three graphs.

Figure 79 shows the records of thermistors placed on cell 6. The initial notable observation is that the thermistors placed at the cell bottom exhibit uniform temperature trends. This indicates a consistent temperature distribution, thus only one curve is displayed in the graph to simplify interpretation.

Despite starting at the same initial temperature, it quickly becomes apparent which cell areas are most susceptible to rapid temperature increases. The positive terminal and the bottom of the cell show the most significant temperature rise, reaching 33°C by the end of the discharge cycle. These are identified as the most critical areas. They are followed by the negative terminal and cell vent, which exhibit a more moderate increase, peaking at 32°C. The battery sides experience the least heating and exhibit the best heat dissipation, yet still reach 32°C by the end of the discharge cycle.

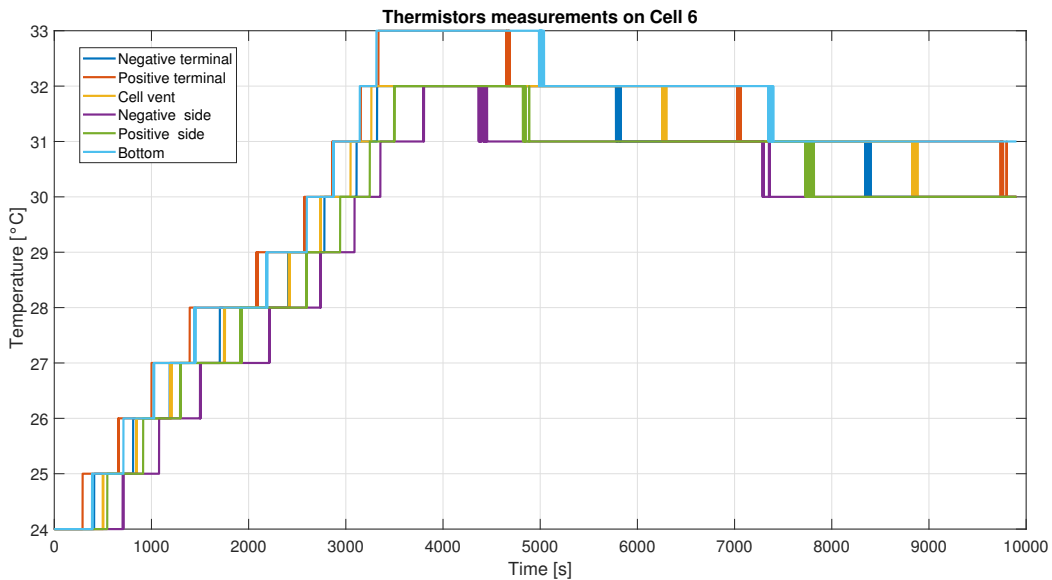


Figure 79: Thermistors measurements on Cell 6 with initial temperature 24°C.

During the cooling phase, the temperature decrease appears fairly uniform across all areas, even considering the different initial temperatures. To ensure safety, the cooling curve of the cell bottom, which experiences the least cooling and the steepest

temperature rise, is used as the reference for evaluating the heat transfer coefficient within the adiabatic chamber. This coefficient is then applied to all surfaces exposed to the air within the module.

Although identifying distinct heat transfer coefficients for each cell area would have enhanced the precision of the thermal simulation, it would have also significantly increased computational demands. Using the lowest heat transfer coefficient ensures a slight overestimation of temperature rise, favoring safety.

Similarly, through tuning in matching the cell's bottom temperature trend, the cell volume fraction generating heat is determined. This parameter, required in the PyaMM thermal sub-model, facilitates the calculation of the absolute heat power produced by the cell. Consequently, the jelly roll is modeled as a single absolute heat power source in the SimScale simulation.

Figure 80 shows the temperature evolution at the bottom of cell 6, cell 9 and cell 12. Similar to cell 6, the thermistors placed at the bottom of the other two cells also exhibit uniform temperature trends, indicating a consistent temperature distribution across all cells. Therefore, only one curve per cell is displayed in the graph to facilitate interpretation.

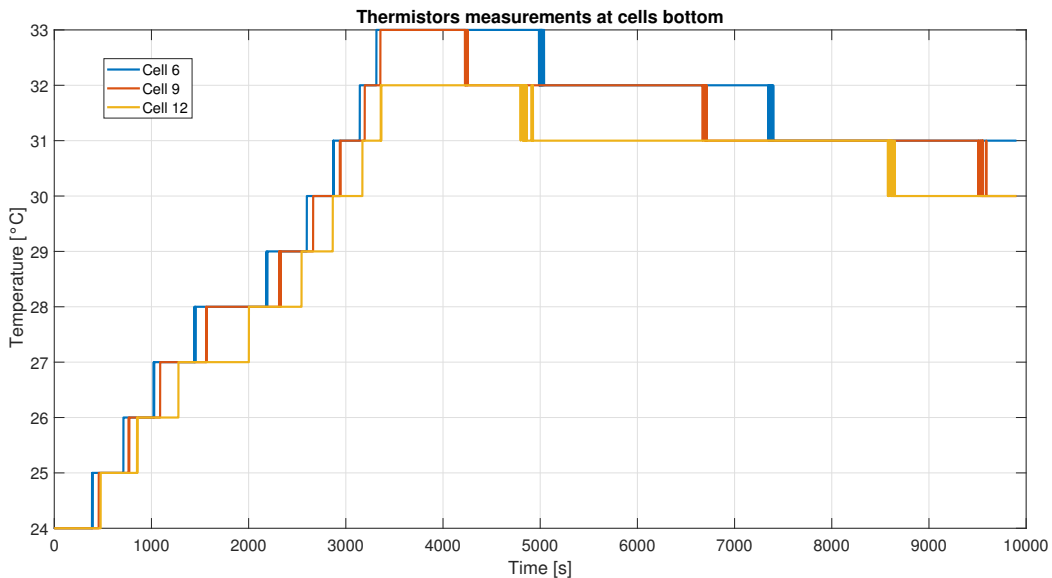


Figure 80: Thermistors measurements at cells bottom with initial temperature 24°C.

During the initial phase of the record, cells 6 and 9 show similar temperature increases, both reaching 33°C simultaneously. In contrast, cell 12 exhibits a lower temperature rise, reaching only 32°C. This highlights a critical aspect: during the heat production phase, cells surrounded by other cells on both sides experience less

efficient heat transfer and consequently higher temperature increases. Conversely, cells at the module's edges, such as cell 12, are subjected to higher heat transfer phenomena. These edge cells are only bordered on one side by another heat source, while the opposite side is adjacent to a passive element that delays but does not obstruct the cooling process.

In the rest phase, the difference between cells 6 and 9 becomes more pronounced. After the discharge cycle ends, cell 9 cools down faster than cell 6, which takes significantly longer to decrease by 1°C. This indicates that when cells are no longer generating heat, their position within the module becomes crucial for effective cooling. This conclusion further supports the decision to use the heat transfer coefficient of cell 6's bottom, as its lower efficiency favors safety.

Figure 81 displays the thermal behavior within the adiabatic chamber, showing ambient conditions as well as the temperature trend at the top and bottom of the box.

The most relevant aspect of this plot is the trend of the ambient condition, which can be given as input value in the boundary condition section of the simulation. Despite a significant rise in the module components' thermal state, the ambient conditions remain constant at the initial value of 23°C, with only sporadic fluctuations.

The graph also illustrates the temperature behavior at the top and bottom of the styrene box, starting from 24°C. Notwithstanding these elements are not present in the mode, the record of their thermal evolution provides useful information. The bottom reaches 29°C, while the top hits 27°C by the end of the discharge cycle. This increase is, as expected, less pronounced than that experienced by the different areas of the cell. Notably, once the maximum thermal state is reached after at the end of the discharge, the box walls' temperature does not decrease as it does for the cells, indicating a simultaneous absorption and release of heat that maintains a steady thermal condition.

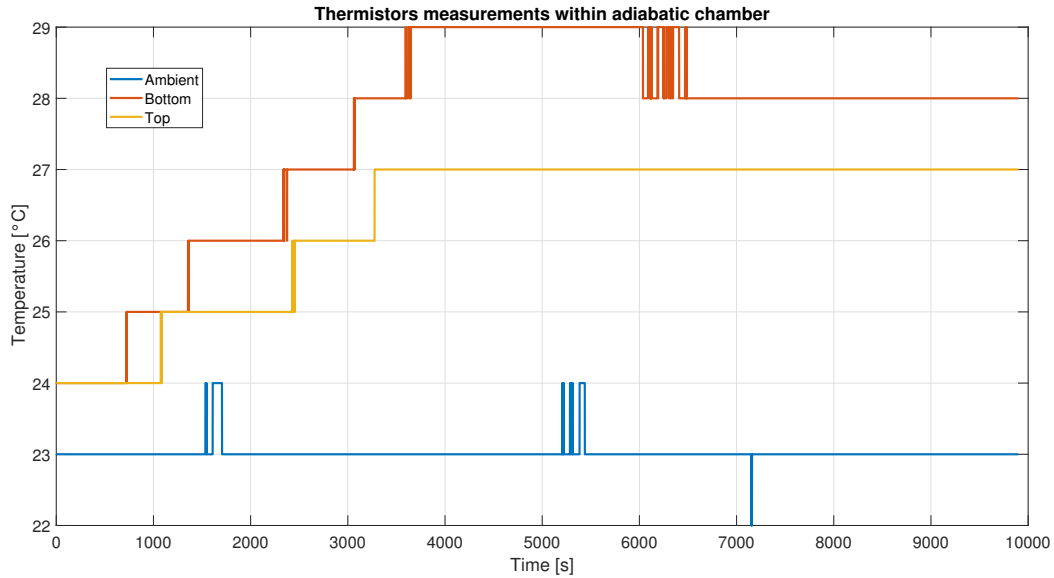


Figure 81: Thermistors measurements within adiabatic chamber.

The second experiment involves more complex data analysis and interpretation, characterized by three distinct phases. Due to pre-heating, each component, including the styrene box, starts at different temperatures ranging from 44°C to 48°C, this will be make more challenging to set proper initial conditions within the thermal simulation. The first phase, lasting approximately 3000 seconds, is a resting period during which the components' thermal states decrease by a few degrees. This is followed by the discharge of the module from 100% to 0% of SOC at 30A, lasting about 3200 seconds, similar to the previous experiment. The final phase is another resting period, analogous to the previous experiment and lasting 6000 seconds, during which all elements within the adiabatic chamber cool down.

These records are crucial as they provide a means to validate the findings from the previous experimental test. Specifically, the heat transfer coefficient of the module and the volume fraction of the cell for heat production estimation can be corroborated using these additional experimental results. This is because the heat transfer coefficient is dependent solely on the convection conditions within the box, which remain unchanged. Consequently, the higher heat exchange is driven by a higher temperature gradient between components and ambient air. Similarly, the volume fraction of the cell responsible for heat production should remain consistent with the previous experiment.

Figure 82 shows the records of thermistors placed on cell 6 during this second experimental test. Despite the different initial conditions, this second test exhibits

the same characteristics as the first. The thermistors at the cell bottom again show uniform trends, indicating a consistent thermal distribution. The areas experiencing the most heating and the least heat exchange are confirmed to be the positive terminal and the bottom of the cell, reaching 49°C. They are followed by the cell vent and negative terminal, which reach 47°C and 46°C, respectively. The sides of the cell demonstrate the least heating and the most efficient heat exchange, reaching only 44°C and 45°C by the end of the discharge process. In any case, a less marked temperature increase is well evident for all the cell areas. This is surely due to the more effective heat exchange process, child of wider temperature difference between the cell components and the ambient temperature.

The cooling phase also shows similarities to the previous test: the thermal decrease appears fairly uniform across all areas, even considering different initial conditions. The temperature decrease is steeper compared to the first test, not due to a different heat transfer coefficient, but because of a larger temperature gradient between the cell parts and the ambient environment, the trend of which is depicted in the third graph.

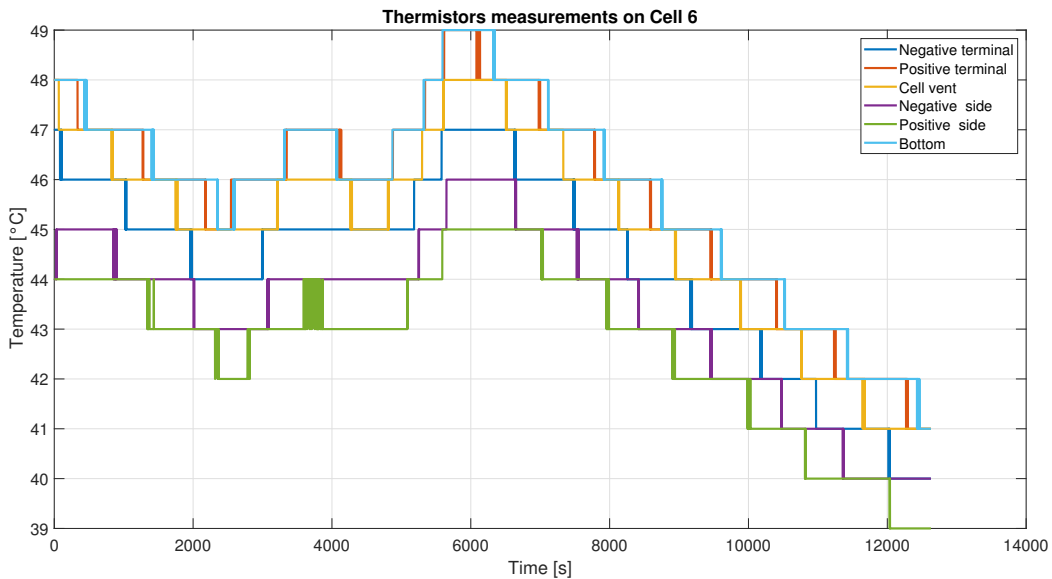


Figure 82: Thermistors measurements on Cell 6 with high initial temperature.

As mentioned earlier, the curve of the bottom of the cell, which experiences the highest heating and the least heat exchange, is used as a reference to confirm the heat transfer coefficient and the volume fraction of the cell producing heat, evaluated based on the first experimental data.

Figure 83 shows the thermal evolution at the bottom of cell 6, cell 9, and cell 12

during the second thermal test. Uniform thermal behavior is recorded at the bottom of cell 9 and cell 12 as well, leading to the plot of only one record.

Consistent with the measurements taken on cell 6 components, this data corroborates the findings from the lower temperature test. Cells 6 and 9 exhibit similar thermal increases, both reaching 49°C, while cell 12 experiences a lower increase, peaking at 46°C. This further confirms that cells surrounded by two other heat sources undergo similar heating and heat exchange processes, unlike cells at the module’s edge, such as cell 12, which are subject to higher heat dissipation towards the frontal plate.

The cooling process, on the other hand, shows a steep and similar temperature decrease for all cells, likely due to effective heat exchange processes driven by the significant temperature difference between the cells and the ambient environment.

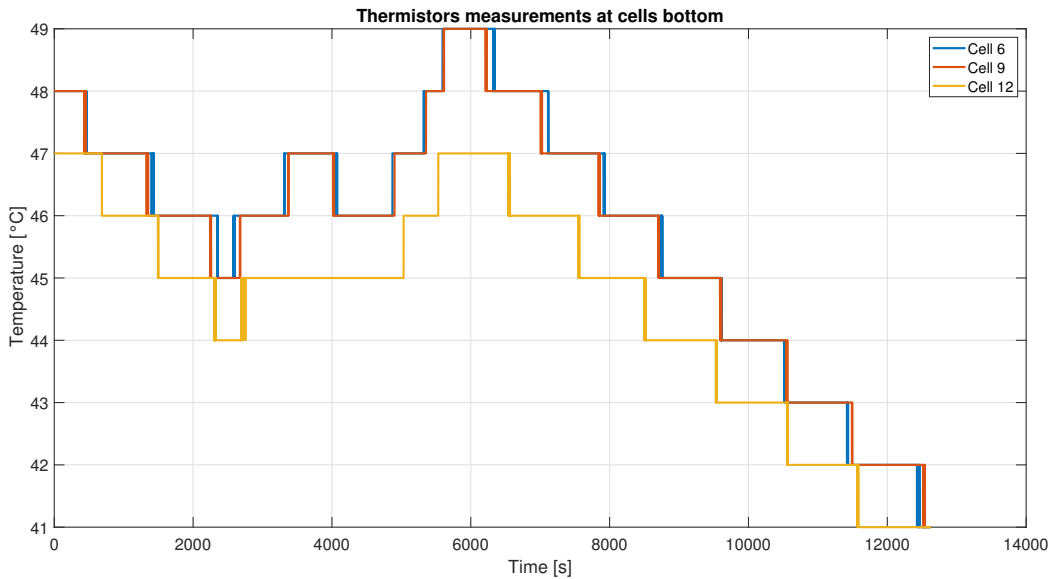


Figure 83: Thermistors measurements at cells bottom with high initial temperature .

Figure 84 shows the thermal evolution within the styrene box during the second thermal test. The ambient thermal profile differs slightly from the previous test. Although the temperature remains at 23°C for most of the time, there are more fluctuations towards 24°C, likely due to the higher initial temperatures of the module.

The thermal behavior at the top and bottom of the chamber does not show the drastic increase observed in the previous test, probably because the temperature rise of the module components is only a few degrees. However, during the cooling phase, the temperature decrease is more pronounced, likely due to the higher initial temperatures, resulting in more efficient heat exchange processes driven by a larger

temperature gradient.

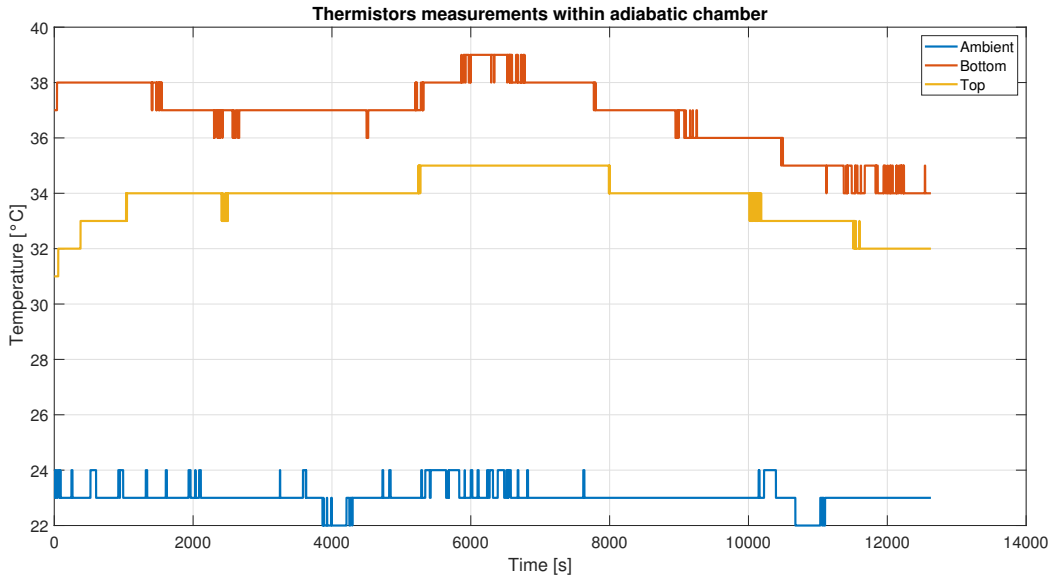
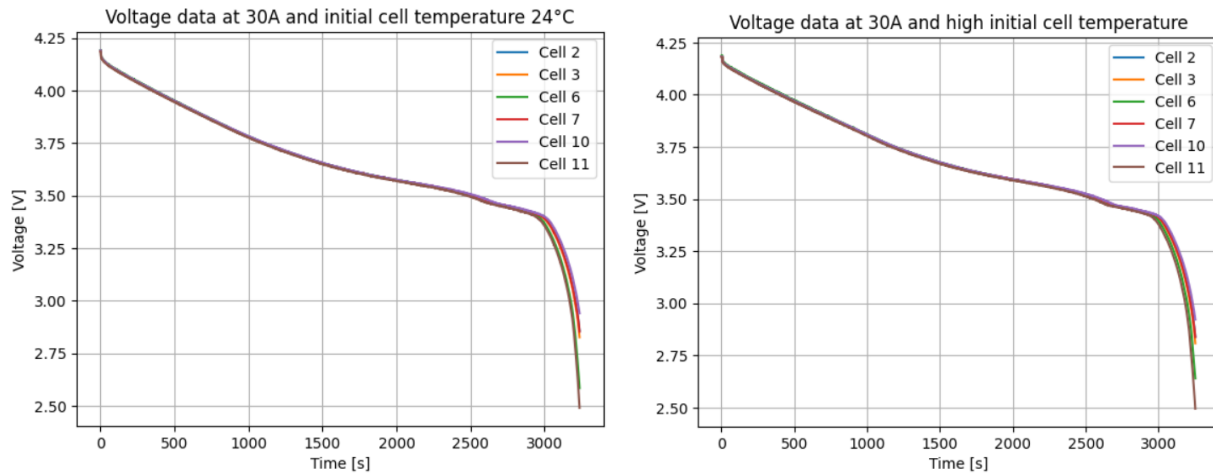


Figure 84: Thermistors measurements within adiabatic chamber.

Figure 85 displays the voltage profiles of some module's cells during the 30A discharge, in the two different thermal conditions.



(a) Cells discharge at 30A and initial temperature 24°C.

(b) Cells discharge at 30A and high temperature.

Figure 85: Cells voltage record during thermal tests.

Despite the different temperatures, there is no significant variation in the voltage trends, both in terms of curve shape and discharge duration, attributable to different capacities. However, these results are valuable for two primary reasons: they contribute to this thesis and provide insights into the battery module's operation.

Firstly, these discharge curves offer additional data to validate the electrochemical model under an additional C-rate at two different temperatures. Secondly, they enable the evaluation of cell discharge behavior within a battery module. While the cells discharge uniformly for most of the cycle, some cells reach 2.5V, whereas others attain 2.8V/2.9V by the end of cycle. The discharge difference between the cells differs for few seconds but it demonstrates that even though the cells within a battery module appear identical, their capacities may slightly vary due to differences in construction quality, aging, and temperature effects.

4.2.2 Model validation

The analysis of the results conducted in the previous section facilitates the establishment of the accurate simulation setup necessary for faithfully replicating the test conditions. This setup strictly adheres to the guidelines outlined in section 3.4. However, certain parameters require meticulous attention to ensure their alignment with the test conditions. Specifically:

- **Initial Conditions:** the initial temperatures of the model components are set in accordance with the initial conditions observed in the test results. For the first simulation, the initial temperature for each element is set to 24°C. In the second test, which is the result of a previous cooling period, different initial thermal states are assigned to the model components, with temperatures ranging from 42°C to 46°C.
- **Boundary Conditions:** this aspect involves two fundamental parameters: the ambient temperature and the heat transfer coefficient. Simscale does not support tabular values for ambient temperature as a function of time. Nevertheless, the experimental data show minor fluctuations of just one degree, with the ambient temperature remaining nearly constant at 23°C in both experiments. Thus, the ambient temperature is set to 23°C for both validation simulations.

As discussed in the previous section, the heat transfer coefficient within the styrene box was unknown during the experimental setup phase. Consequently, the cool-down period following the discharge cycle was recorded to evaluate this coefficient. Using the cooling trend of the cell bottom as a reference, the heat transfer coefficient within the styrene chamber is determined to be $2W/(Km^2)$ for both simulations after several cooling simulations, with initial conditions set to the temperature values at the end of the discharge test.

- **Power Source:** in the simulations, the jelly rolls are modeled as the sole absolute heat power source, requiring the heat produced during the discharge cycle as input. The heat production is evaluated using the PyBaMM thermal sub-model, as explained in section 3.2. Before validating the experimental test, the volume fraction of the cell producing heat needs to be evaluated. The model provides a volume-averaged heat, which must be multiplied by a volume that, due to model simplifications, cannot be the entire cell volume. Experimental test results are used to adjust this parameter until the best match with data is achieved, resulting in a cell fraction producing heat of approximately 50% of the total cell volume. Thus, the jelly rolls are set as an absolute power source, producing the estimated amount of heat as per the thermal sub-model, with the assumption that each cell generates the same amount of heat.
- **Results Control:** The temperature "area average" is applied to all faces for which experimental data are available for comparison, including the bottom of cells 6, 9, and 12, terminals, vent, and module side.

Before proceeding with the validation, two important aspects must be still highlighted.

Firstly, as explained in section 3.5, the coupling of thermal sub-model and thermal simulation involves few iterations. The starting point is the thermal sub-model with a temperature compatible with the experimental data, and the loop is repeated twice. No appreciable differences are observed in the model results after these iterations, so only the results from the last iteration are reported for readability.

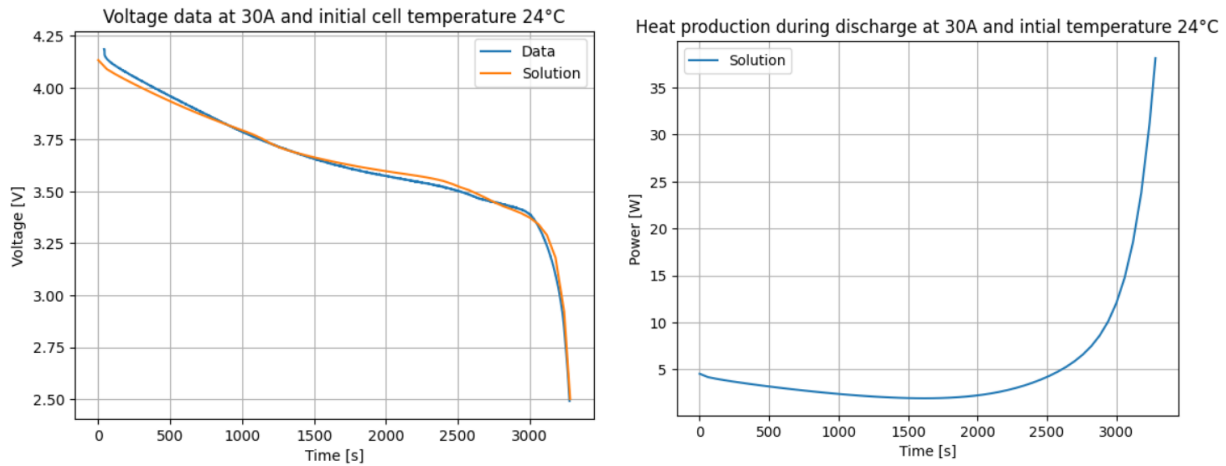
Secondly, regarding the visualization of results, the data are linearized to better visualize the model's accuracy in matching the experimental trends, without forgetting that the resolution still remains limited to 1°C. This operation ensures a certain margin of error, consequently the simulation is considered a good approximation of the experimental data if the temperature trend remains within this resolution range.

It is now possible to analyze the results of the first simulation by comparing them with the experimental data from the test, conducted with a starting temperature of 24°C.

Figure 86 presents the outcomes of the electrochemical model and the thermal sub-model implemented in PyBaMM. The plot in Figure 86a depicts the model's alignment with experimental voltage discharge data. The considerations discussed in the previous section regarding the validation of the electrochemical model are further corroborated here. For a current intensity of 30A, the model accurately

matches the experimental data. The cell's capacity is well represented, although there are minor fluctuations that slightly deviate the model response from an optimal match, particularly at the beginning and just before the voltage drop in the curve. Nevertheless, the error is acceptable, with maximum values of 20 mV.

Graph in Figure 89b illustrates the outcome of the thermal sub-model, specifically the absolute heat power produced by the cell during this discharge cycle. The heat production exhibits a parabolic trend: starting from a value of 5 W, the generated heat progressively decreases, reaching a minimum value of 1.5 W between 1500 and 2000 seconds. After this minimum, the heat production sharply increases, reaching values seven times higher than the initial heat produced by the end of the discharge cycle. Despite the significant increase in the last 10% of the cycle, the heat produced by the cell remains within a narrow range of 1.5 W to 5 W for most of the cycle.



(a) Model match of the discharge curve at 30A.

(b) Absolute heat power produced by the cell.

Figure 86: Outcomes of PyBaMM models for the simulated discharge at initial temperature 24°C.

In figure 87 simulation results are compared with the temperature records obtained from thermistors placed on cell 6 during the discharge cycle at 30A. The simulated thermal evolution exhibits a similar trend to the experimental data. The bottom of the cell, used as a reference in this simulation, is confirmed to be the area with the highest heating and the least heat exchange, maintaining a consistently higher temperature than other cell parts.

In contrast, the simulation shows the positive terminal's temperature evolution closely aligned with that of the negative terminal and cell vent, creating a uniform temperature region on the top of the cell. This discrepancy can be attributed to the thermal model's assumption that only the jelly roll acts as the heat power source within the cell. Consequently, while the positive terminal actively contributes to

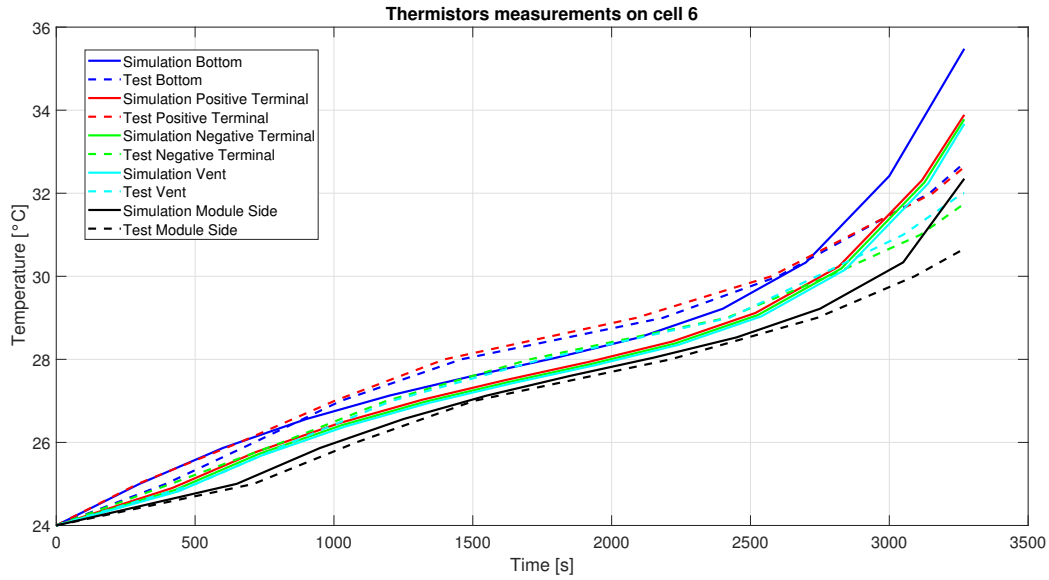
heat production in the experiment, causing it to heat up, it is treated as a passive component in the model, subject to heat transfer processes like the other parts. The module side is confirmed to be the area subjected to the least heating and the highest heat exchange processes.

Overall, the predicted temperature trend follows the parabolic shape of heat production, with moderate heat production at the beginning, reduced heat production in the middle part of the cycle, and significantly higher heat production towards the end.

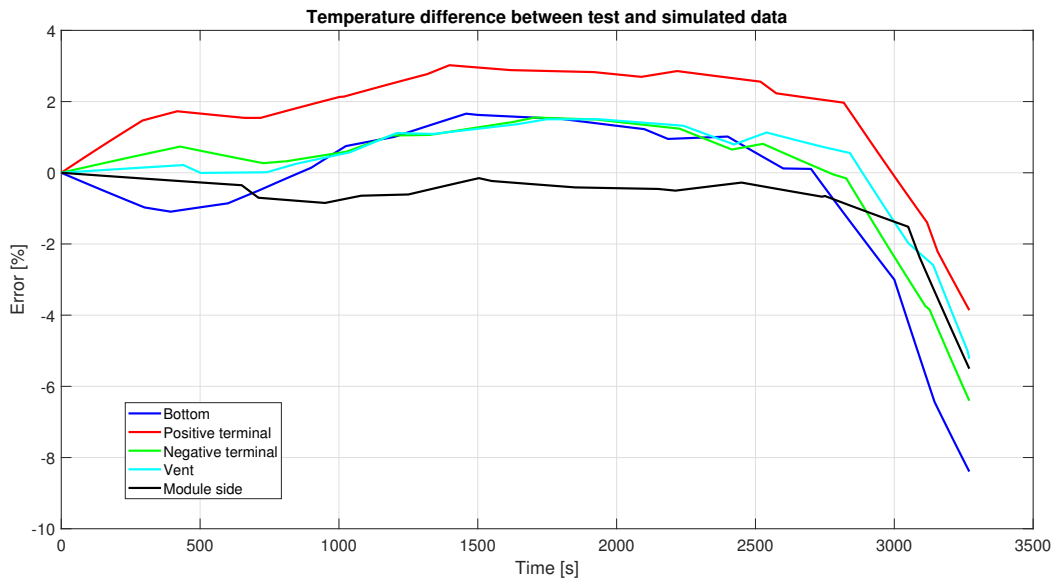
Comparing the simulation with the real data, the prediction is highly accurate up to 2800 seconds, with an error margin swinging around 2%. There is a slight temperature overestimation in the initial phase, followed by a slight underestimation in the middle part of the simulation. After 2800 seconds, when the remaining SOC is around 10%, the model's overestimation progressively increases, reaching an error of nearly 8%.

This trend was anticipated following the validation of the electrochemical model, due to the reduced fidelity of the GITT in the final part of the discharge cycle. Additionally, the steep increase in heat production observed in the last 5% of SOC indicates unrealistic cell behavior, highlighting the challenges in cell modeling at low SOC. This is due to highly non-linear characteristics, in particular particle size distributions and non uniformity of the particles states (lithiation degree) within that distributions, which are difficult to model accurately with limited resources.

Nonetheless, this overestimation favors safety by providing a conservative estimate of the required cooling for potential second-life applications.



(a) Temperature evolution comparison.

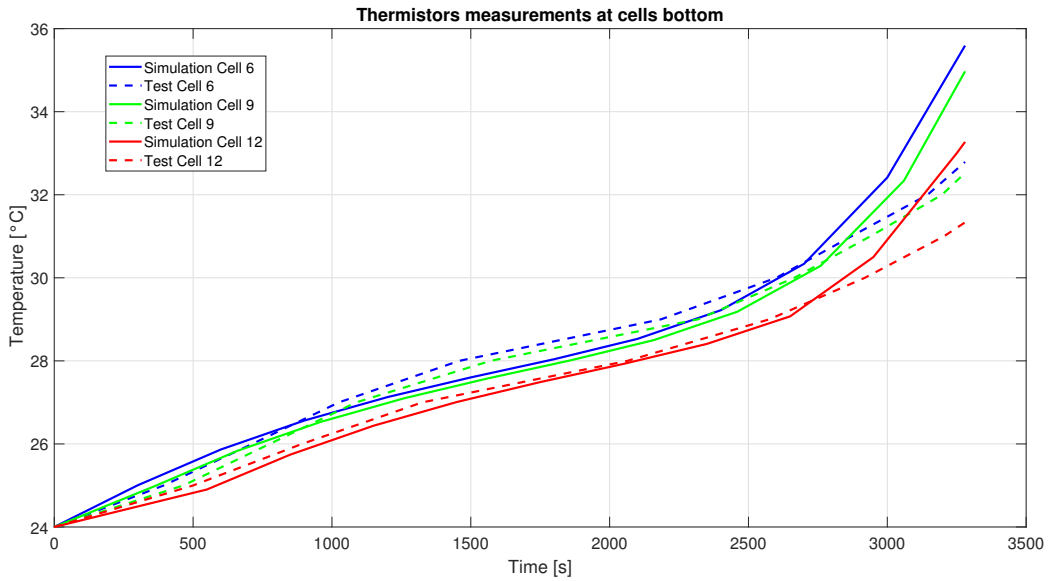


(b) Percentage difference.

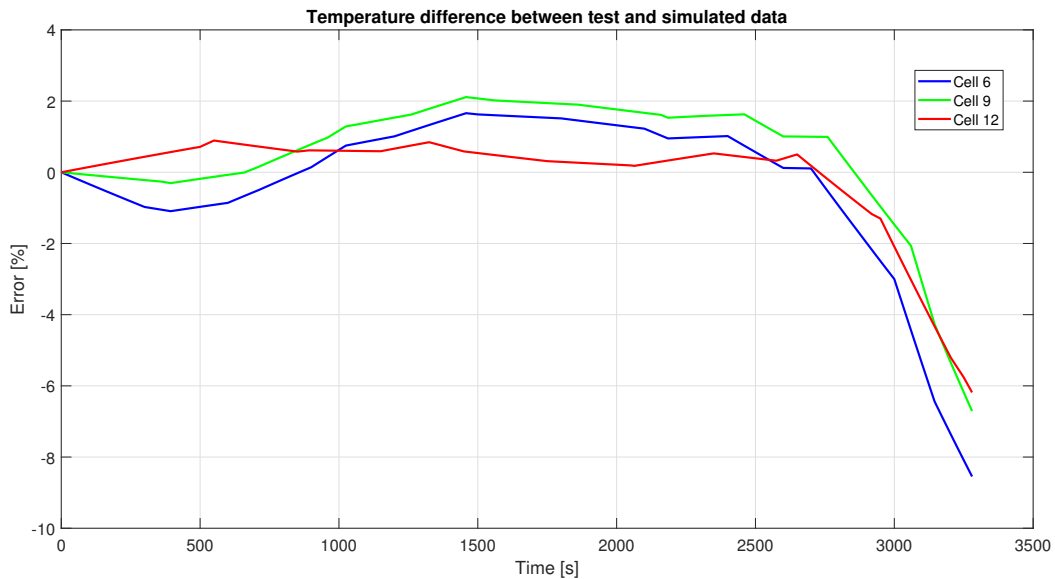
Figure 87: Simulation match with thermistors measurements on cell 6, for the test with initial temperature 24°C.

Figure 88 compares the simulation results with the test data from thermistors placed at the bottom of cells 6, 9, and 12. The simulation provides information consistent with the analysis of the experimental data. The temperature evolution of cells 6 and 9 is very similar, whereas cell 12 exhibits different behavior, being subjected to less heating and more significant heat exchange processes. This

demonstrates the model's capability in evaluating the heat exchange characteristics of different cells. Specifically, cells sandwiched between other heat power sources show a similar thermal trend, while cells at the module's extremes, in contact with a passive element such as the frontal plate, experience more heat exchange.



(a) Temperature evolution comparison.



(b) Percentage difference.

Figure 88: Simulation match with thermistors measurements on cells 6, 9 and 12, for the test with initial temperature 24°C.

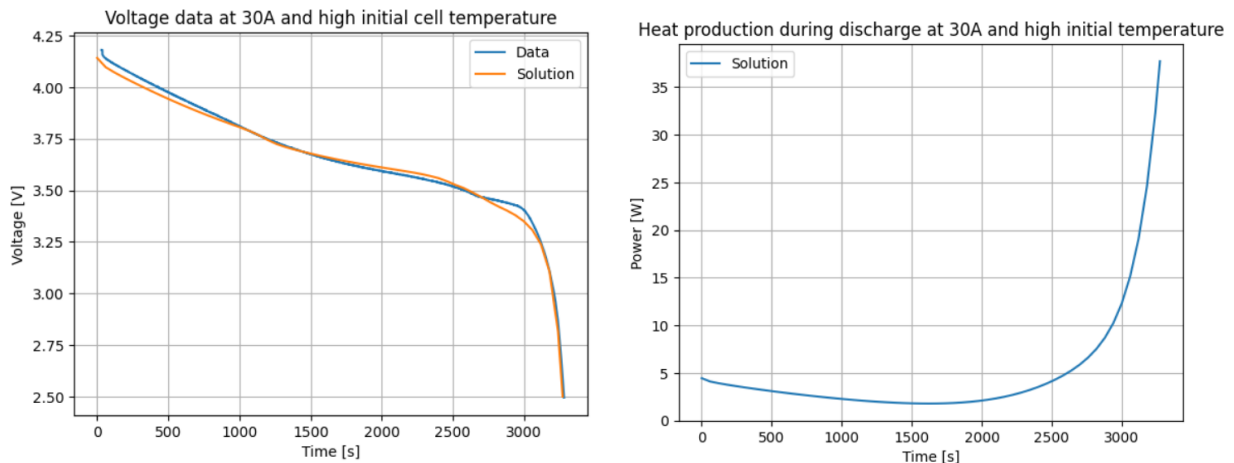
Regarding the model's accuracy, the same considerations made for the previous

graph apply here. Until the cells reach 10% of the remaining SOC, the percentage error of the model’s predictions hovers around 2%. However, the model’s accuracy progressively decreases towards the end of the discharge cycle, reaching errors between 6% to 8% in the final moments. This percentage error reflects the decreased accuracy of the electrochemical model and the heat overestimation of the thermal sub-model.

Despite this, the crucial aspect is that the model provides a good prediction for the majority of the discharge cycle. Even though the accuracy decreases in the last part of the cycle, this only plays in favor of safety, as it overestimates the cooling capacity necessary for the module.

It is now possible to analyze the results of the second simulation, which reproduced the temperature evolution of the module during at discharge at 30A but with initial temperature of the cells in the interval 44°C and 46°C.

In Figure 89 the outcomes of the electrochemical model and its thermal sub-model are presented. As expected from the analysis of the experimental discharge curves done in the previous section, which did not highlight substantial differences, the simulated discharge curve also shows very low sensitivity to temperature changes. Consequently, the accuracy of the model in matching the experimental data is comparable to what was previously described. The cell capacity is well represented, with minor fluctuations slightly deviating the model response from an optimal match. The maximum error values of 20 mV occur just before the voltage drop region.



(a) Model match of the discharge curve at 30A.

(b) Absolute heat power produced by the cell.

Figure 89: Outcomes of PyBaMM models for the simulated discharge at high initial temperature.

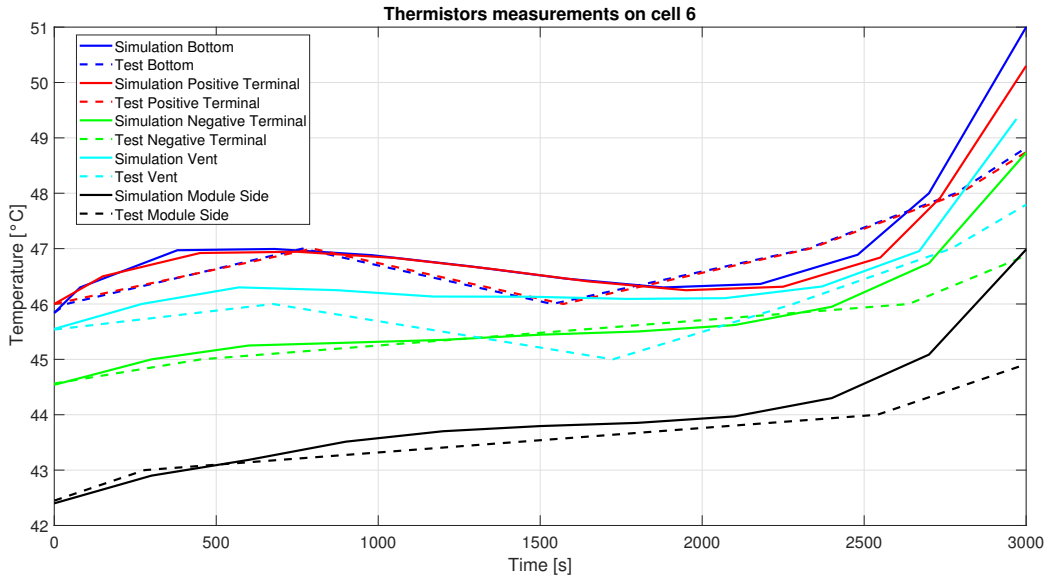
This discussion also applies to the outcomes of the thermal sub-model, specifically

the plot of the produced heat. The trend and overall value of the heat produced during the cycle are comparable to the previous simulation. Although there is a slight difference in the produced heat, it is almost imperceptible. This is likely due to improved efficiency from enhanced chemical reactions at the higher temperature.

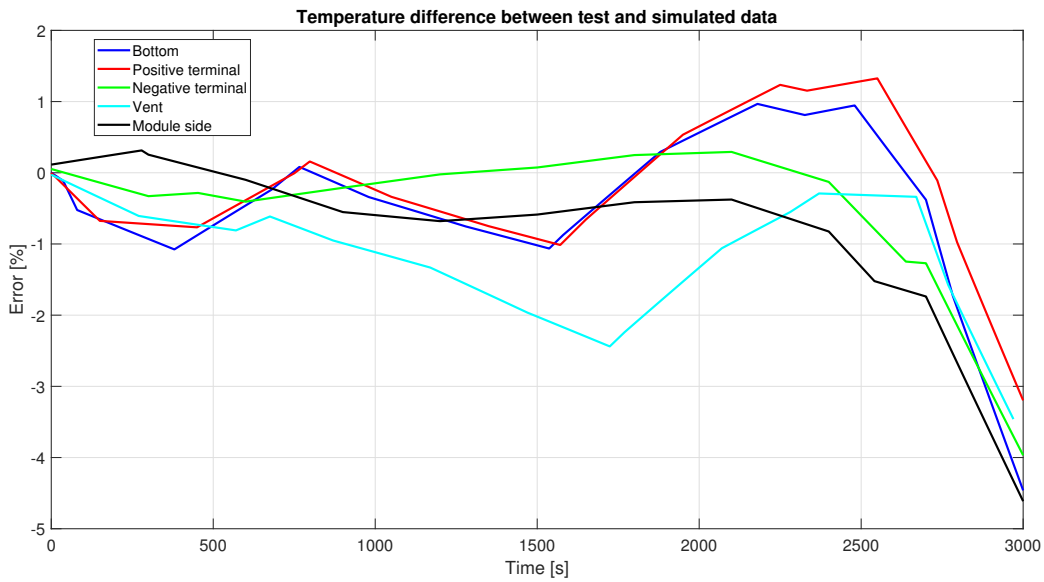
Continuing the discussion of the results, it is possible to analyze the simulation's match with the thermistor measurements on cell 6, shown in Figure 90. A notable aspect is the more complex interpretation of these results compared to the simulation at 24°C. In this case, different initial temperatures are set for the parts of cell 6, making the comparison graph less straightforward. The differences in thermal evolution could be due to varying levels of heating and heat exchange intensity resulting from the different initial temperatures. Nonetheless, the model's ability to reproduce the experimental data is analyzed.

Each curve shows a good overall approximation of the thermal evolution of different cell areas, with the bottom of the cell confirmed to be the most sensitive area, subjected to high heating and lower heat exchange processes. Unlike the previous case, the terminals and cell vent exhibit different initial temperatures, resulting in a non-uniform temperature distribution at the top of the cell. The module side, both in the simulation and experiment, demonstrates the least heating and most effective heat exchange processes.

Regarding the model's accuracy, the considerations made for the previous simulation are also valid here. The model effectively reproduces the experimental thermal evolution for most of the test, maintaining a percentage error around 2% up to 2800 seconds, corresponding to about 10% of the remaining module state of charge. As in the previous simulation, the accuracy progressively decreases as the SOC drops, reaching a maximum error between 3% and 5% towards the end. Despite similarities with the previous results, this simulation shows a less steep increase in error percentage, possibly due to the better accuracy of the electrochemical presented in section 4.1.3.



(a) Temperature evolution comparison.

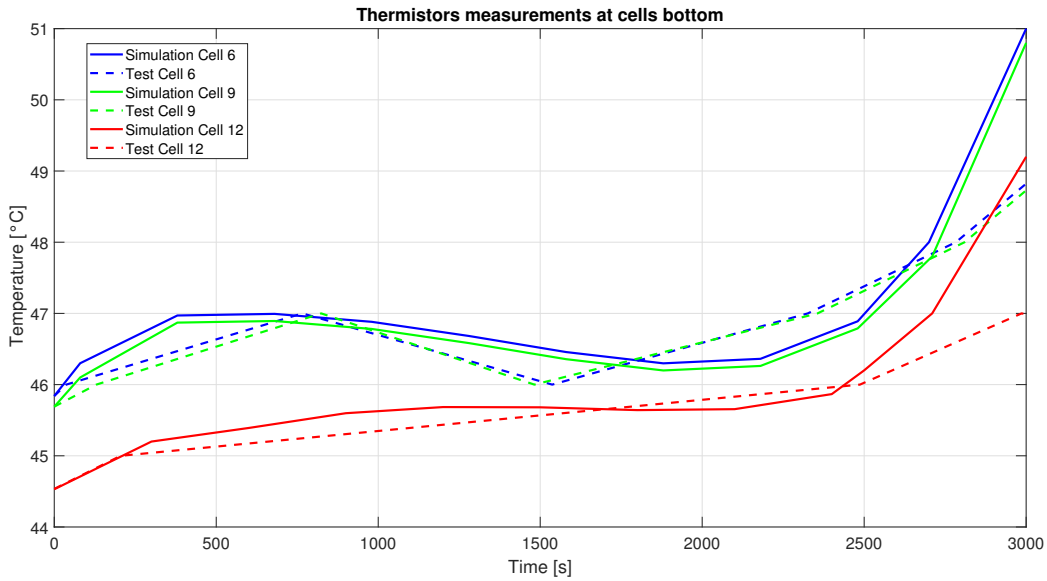


(b) Percentage difference.

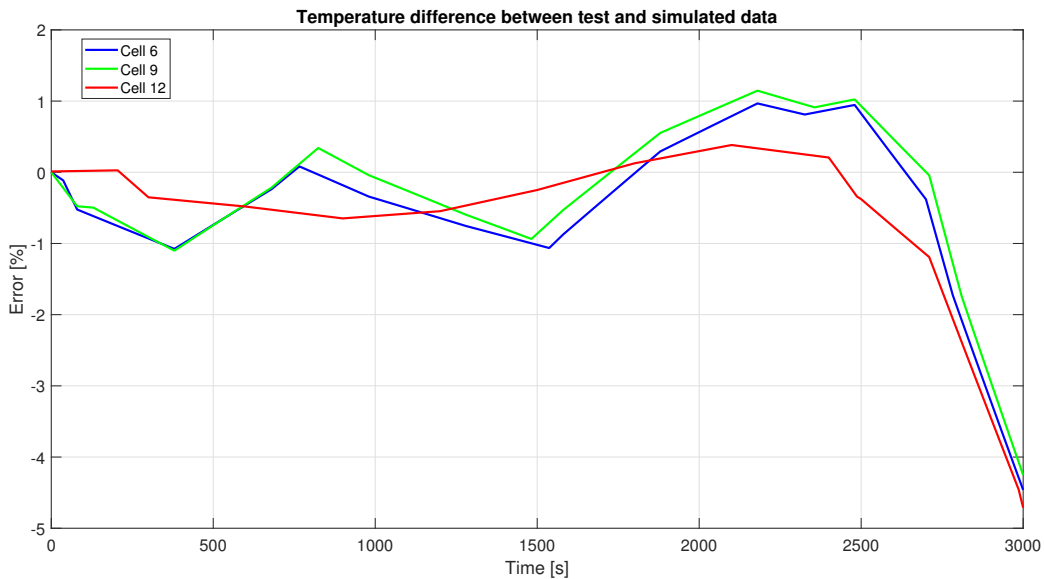
Figure 90: Simulation match with thermistors measurements on cell 6, for the test with high initial temperature.

Discussing the simulation matching of the thermal evolution of cells 6, 9, and 12, the considerations made for the previous graph are also applicable here. Figure 91 shows a good prediction for all cell temperature evolutions, despite the less straightforward reading due to different initial temperatures between cells 6, 9, and 12. Notably, as previously discussed, the trends for cells 6 and 9 are nearly identical. This demonstrates the model’s capability to accurately recognize the heating and

heat exchange processes for elements standing between two heat source, even under different temperature conditions. As in the experiment, the behavior of cell 12 differs from the other, starting at a lower temperature and exhibiting a less steep temperature increase due to the passive frontal plate on one side.



(a) Temperature evolution comparison.



(b) Percentage difference.

Figure 91: Simulation match with thermistors measurements on cells 6, 9 and 12, for the test with high initial temperature.

The model's accuracy is consistent with the previous comparison and even

improved. It accurately describes the thermal evolution of the cells, maintaining a percentage error around 1% up to 2800 seconds. The model slightly overestimates the temperature increase for most of the discharge cycle, followed by a slight underestimation just before the 2800-second mark. After this point, coinciding with the SOC drop, the accuracy progressively decreases, reaching errors between 4% and 5% by the end of the simulation. This error margin aligns with the temperature evolution prediction for cell 6, also demonstrating improved temperature evolution predictions for cells 9 and 12 compared to the simulation results at the initial temperature of 24°C. The reasons for this improvement are the same as previously discussed.

In the preceding graphs, all potential comparisons between the simulated and experimental data of the recorded temperature evolution have been thoroughly analyzed. The coupled electrochemical-thermal model exhibits a satisfactory prediction of the temperature evolution of the module for each of the recorded areas by thermistors. This demonstrates not only an accurate prediction of heat production in the cells during the discharge cycle but also a faithful representation of the module in the simulation, even when simplified relative to the original.

The model ensures high reliability under both tested conditions, with an overall error within two percentage points for the majority of the discharge cycles. However, this comparison has also highlighted two primary weaknesses of the model. Firstly, with the module simplified by considering the jelly roll as the sole heat source within the cells, the heat production contribution from other components, mainly the terminals, is not adequately represented. This could be problematic for applications with high current intensity, leading to significant and uneven heating at the battery terminals. Nevertheless, this is not an issue for the second-life applications selected for this module, which will experience a maximum discharge rate comparable to the tested conditions. In these tests, the alignment of the cell terminals with the temperature evolution of the cell bottom was observed, indicating that the terminals will be subjected to the same conditions as the cell bottom, the area with the highest heating phenomena, which is well represented by the model.

The second aspect pertains to the heating overestimation by the coupled model when the module drops below 10% of the remaining state of charge. The accuracy progressively decreases, reaching an overestimation of 8% in the worst case. This highlights the challenge of modeling the behavior of a cell approaching complete discharge due to the above mentioned highly non-linear phenomena. Despite this, the overestimation covers a narrow range of the actual module capacity, which, in

some applications, may never be encountered. Even if such a range is reached, the temperature rise estimation favors safety by overestimating the required cooling for the module.

The outcomes of the previous validation process has demonstrated the incredible value of the electrochemical-thermal coupled model. Well evident is its capability of effectively reproducing diverse duty cycles, evaluating the voltage evolution, the required discharge rates, levels of power, but, overall, the heat produced during the cycles. With such information it is in fact possible to evaluate the temperature evolution within the module, for given cooling conditions. This peculiarity makes the model an effective and valuable tool in the preliminary thermal performance evaluation. Consequently, is is possible to go forward, passing to the last part of this study: the simulation of the chosen second life scenarios and the assessment of the module thermal performance.

4.3 Second life assessment

In this final section, the outcomes of simulations designed to replicate the selected second-life applications are analyzed. This involves reproducing the duty cycle within both the coupled electrochemical-thermal model and its simulation, under the specified boundary conditions. The presented results are derived from two iterations conducted within the model's loop to achieve the most accurate and reliable outcome.

4.3.1 Renewable solar firming

In this section are presented the results of the solar firming duty cycle simulation.

Figure 92 presents the results of the PyBaMM model, illustrating voltage, current, terminal power, and heat production of a representative module's cell. Starting from a SOC of 100%, the cell sustains energy delivery for the entire 10-hour reference duty cycle, alternating between discharge (predominantly) and charge (less frequently) phases, and concluding with minimal remaining energy.

As anticipated during the design phase, the cell experiences a maximum current rate of 0.4C and a peak terminal power of 40W during multiple discharge cycles. In contrast, the charging phases are less demanding, reaching a current rate of 0.3C and terminal power around 30W.

These parameters indicate a well-dimensioned battery pack, capable of meeting the application's requirements without excessively stressing the cells, thereby preserving their available capacity. Consequently, the corresponding heat production

is lower compared to tested conditions with higher current intensities. The heat generation remains around 1W for most of the cycle, rising to approximately 5W towards the end of the duty cycle when the SOC is low and model heat production prediction increases.

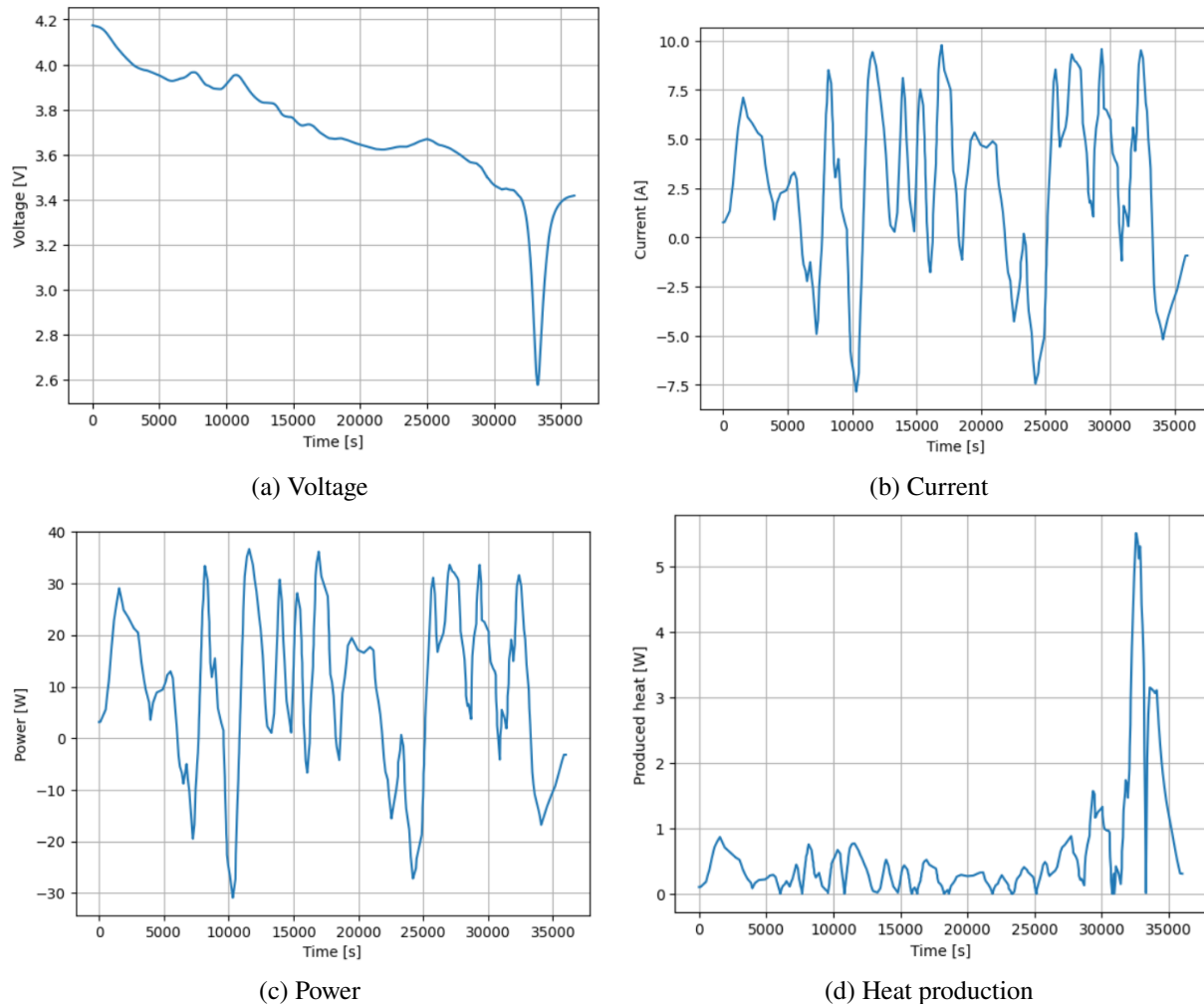


Figure 92: Solar firming duty cycle.

The duty cycle is subsequently simulated within the thermal model. The boundary conditions are outlined in Table 18. The initial temperature of the pack is approximately 45°C, replicating a hot, sunny day, and it is subjected to natural air convection at 45°C, simulated with a heat transfer coefficient of 10W/Km², applied to all exposed surfaces.

Figure 93 depicts the temperature evolution of the jelly rolls throughout the entire simulation. Unlike previous simulations, this analysis focuses on the temperature changes within the jelly rolls, the core of heat production, making it critical to

monitor their thermal behavior.

The first key observation is that, despite the challenging cooling conditions and the cells' heat production, the temperature remains within an optimal range, between 45°C and 47°C. Only towards the end of the cycle does the temperature slightly rise, reaching 50°C. This increase is attributed to the higher heat production predicted by the model in the final SOC phase. Despite the overestimation of heat production and its increase, the module's temperature stays within a safe and optimal range.

This simulation also confirms the trend observed in the experiments and validation. The temperature evolution in cells 6 and 9 is quite similar, as they undergo the same heating and cooling processes. Conversely, cell 12 exhibits more cooling and lower temperatures, due to the presence of the frontal plate acting as a passive cooling element.

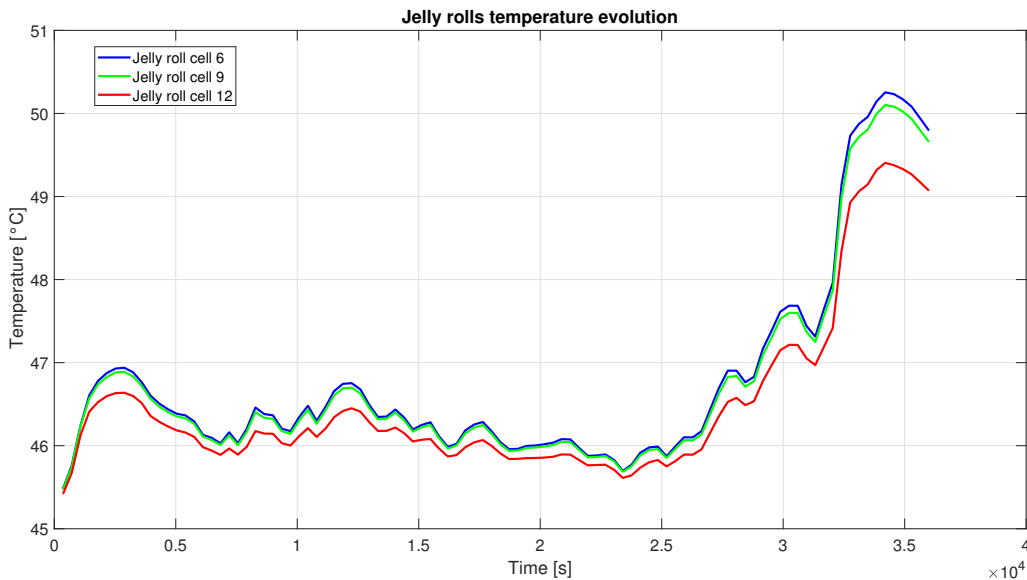
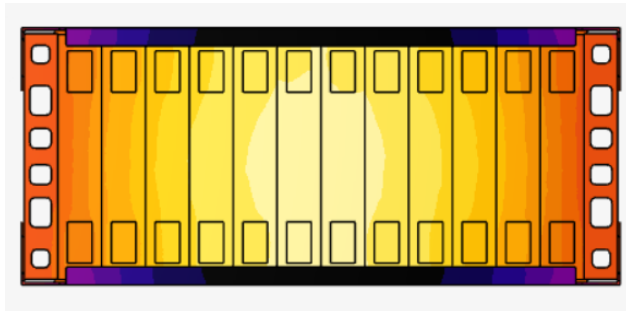


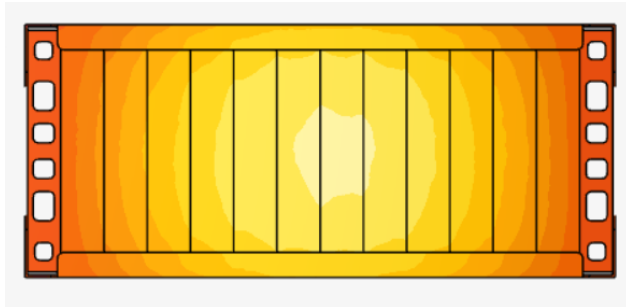
Figure 93: Jelly rolls temperature evolution in solar firming duty cycle.

Figure 94 does not provide significant insights for assessing this application for the module. However, it is included to offer a graphical visualization of the temperature distribution within the module at the end of the simulated duty cycle, when the module experiences its highest temperatures.

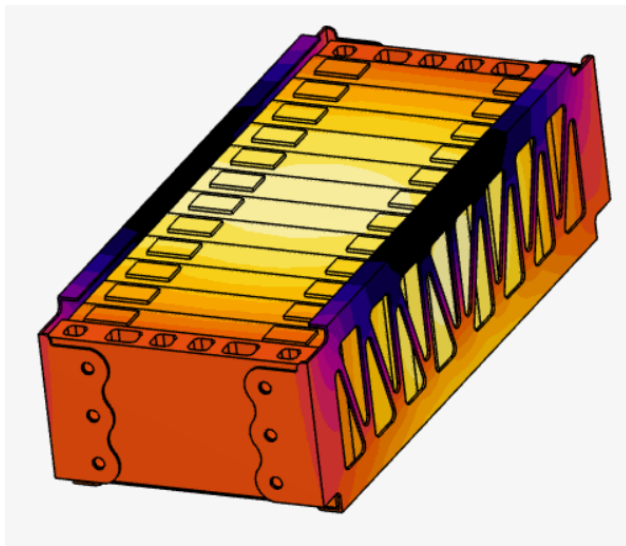
The top and bottom views clearly show that the highest temperature is concentrated in the middle of the module, gradually decreasing towards the edges. Despite this, the temperature distribution is relatively uniform across the module, with a temperature variation of only a few degrees between the different components.



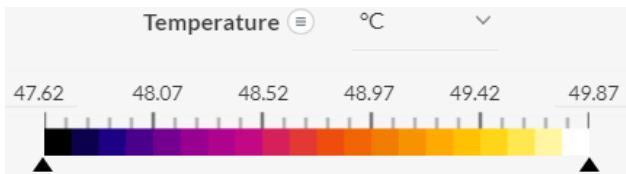
(a) Module top view



(b) Module bottom view



(c) Module isometric view



(d) Legend

Figure 94: Module temperature at the end of firming duty cycle.

4.3.2 ESS for PV domestic application

This section presents the results of the domestic ESS duty cycle simulation. Figure 95 shows the results of the PyBaMM model, with the same outputs as the previous simulation.

According to the specifications in Table 18 and starting from a SOC of 47% (to better appreciate the performance of the ESS), the simulation shows the capability of the ESS to ensure supply energy to the domestic environment for 13.5 hours, from 8 am to 9:30 pm. This indicates that, to cover the daily energy needs of the household, both the ESS and the PV plant would need to be enlarged, increasing storage capacity and recharging capability from the panels. Despite this, the result is satisfactory, as the ESS and PV plant can ensure the house's energy independence from the grid during peak usage hours, leaving only the nighttime hours, characterized by low electricity consumption, uncovered.

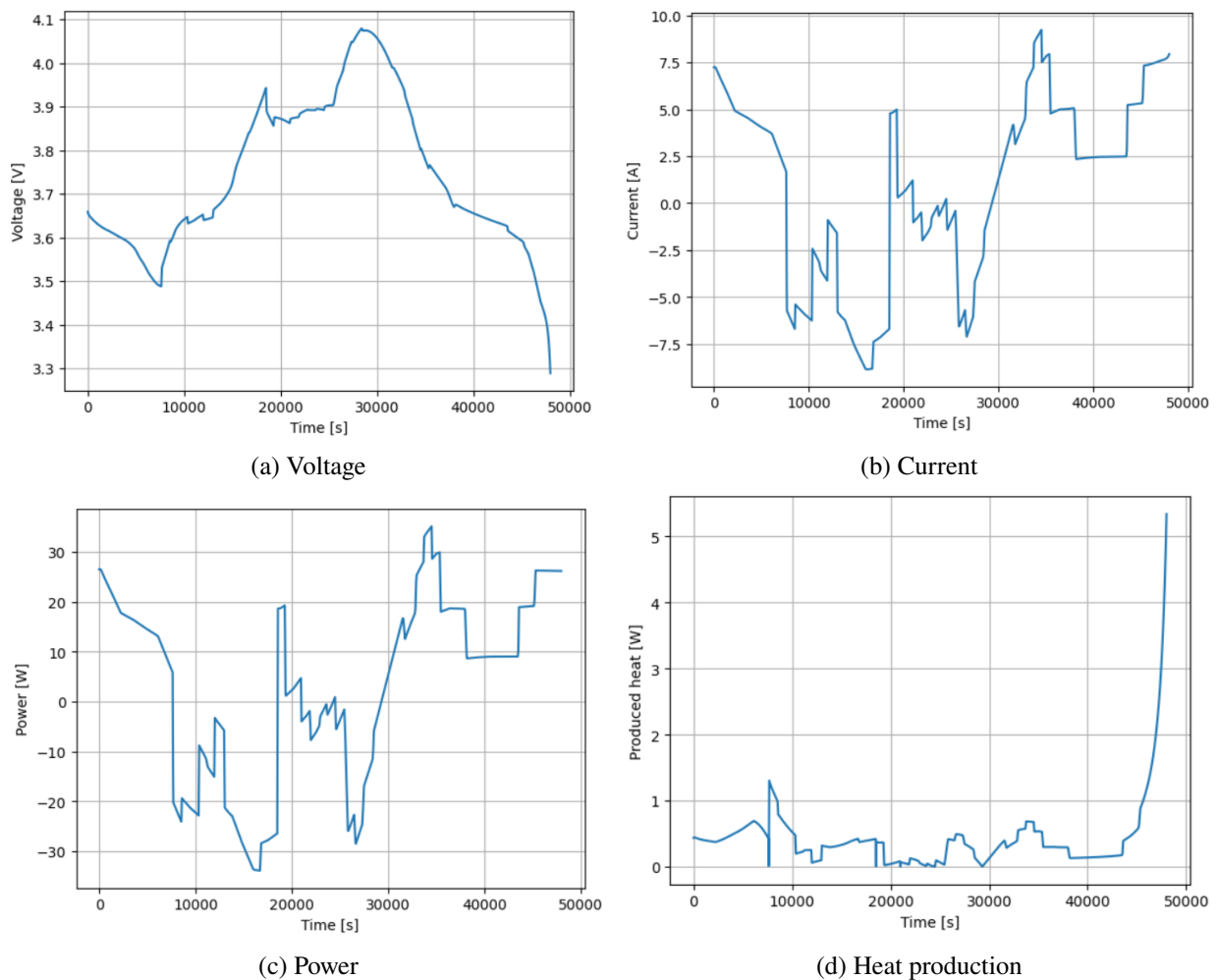


Figure 95: Domestic ESS duty cycle.

The resultant current intensity aligns with the predictions made during the design phase, with a maximum rate of 0.3C for both charging and discharging. Similarly, the power reaches a maximum value of 30W. This condition results in reduced heat production, around 0.5W for most of the day, with a peak of 1W when charging begins. The final part of the cycle shows higher heat production corresponding to the cell's final discharge. Nonetheless, the heat power peaks at 5W at the end of the simulation. This condition is clearly less demanding compared to the previous one, indicating a very favorable temperature evolution in the thermal simulation.

Figure 96 illustrates the temperature evolution of the jelly rolls throughout the entire simulation. The initial temperature of the pack simulates indoor summer conditions, starting around 25°C. Cooling is achieved through natural convection of the surrounding air at 25°C, simulated with a heat transfer coefficient of 10W/Km², applied to all exposed surfaces of the module.

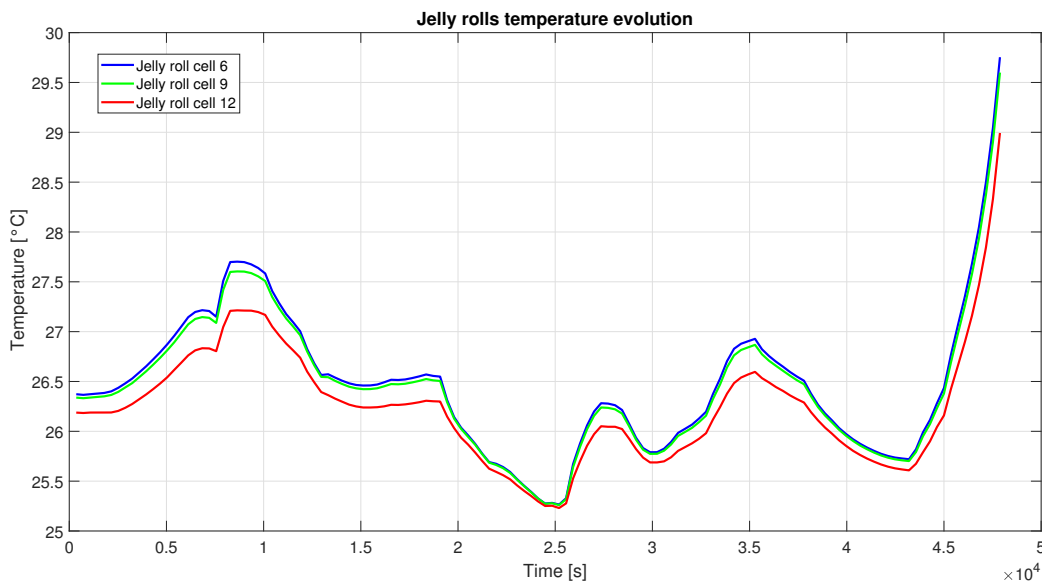
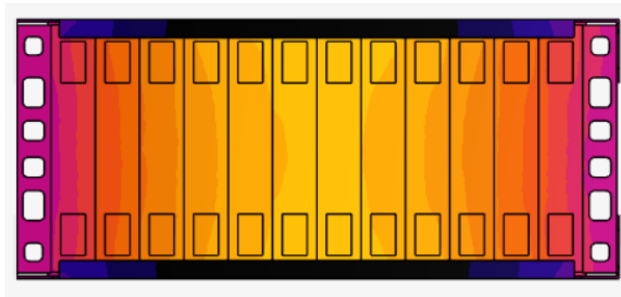


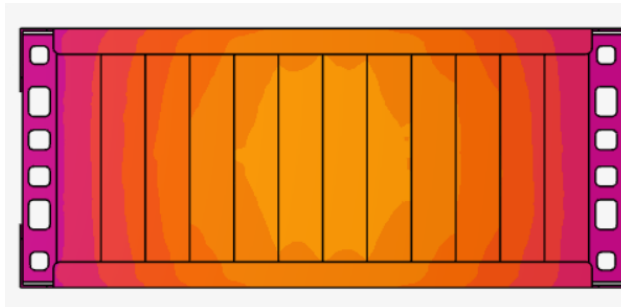
Figure 96: Jelly rolls temperature evolution in domestic ESS duty cycle.

The temperature evolution of the jelly rolls aligns with expectations from previous analyses. Given that these conditions are less demanding than those applied for solar firming, both in terms of current intensity and cooling (due to lower ambient temperatures), the temperature evolution of the jelly rolls is optimal. It remains between 25°C and 27°C for most of the cycle. Only at the end of the discharge phase, corresponding to the increased heat production forecasted by the thermal sub-model, does the temperature rise steeply, reaching almost 30°C. This temperature is perfectly safe and even optimal for the module. The different behaviors between cell 6 and 9

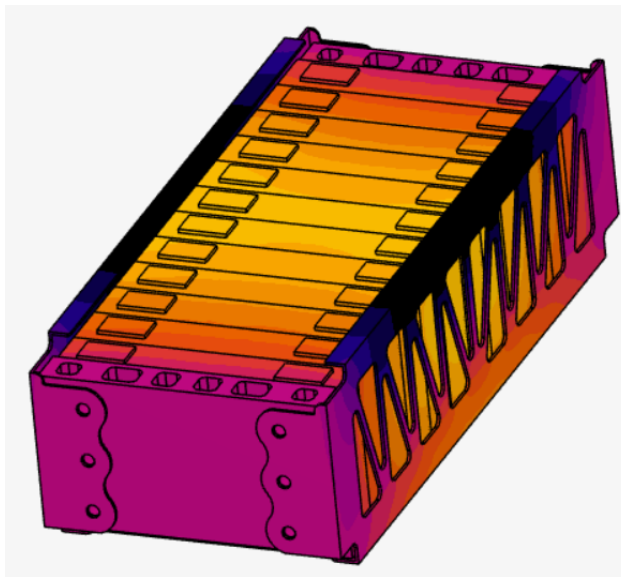
and cell 12 are also confirmed in this case.



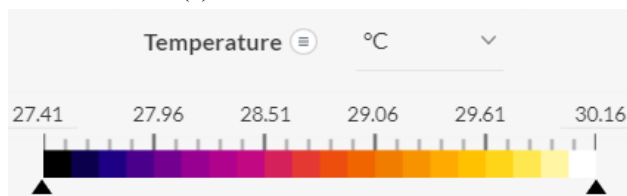
(a) Module top view



(b) Module bottom view



(c) Module isometric view



(d) Legend

Figure 97: Module temperature at the end of domestic ESS duty cycle.

Also in this case, the graphical temperature distribution within the module at the end of the duty cycle is shown in Figure 97. The distribution is consistent with the previous simulation, except for the temperature range, which is between 27°C and 30°C.

The cells in the middle are again shown to be subjected to the highest heating, while the other components, acting as passive elements, experience less heating and consequently a lower temperature increase. This visualization reinforces the observation that the core cells bear the brunt of the thermal load, while peripheral components maintain relatively cooler temperatures.

4.3.3 Electric forklift

This section presents the results of the electric forklift duty cycle simulation. Figures 98, 99, 100, and 101 display the results of the PyBaMM model. Due to the high frequency of the duty cycle, lasting only 25 seconds, the plots of the complete duty cycle are not easily readable. Therefore, a detailed view of the results from second 1000 to second 1025 is also included. Starting from a full SOC, the battery module, with specifications outlined in Table 18, can ensure almost three continuous hours of autonomy.

The resultant current and power intensity align with the forecasts made during the design phase of the pack. The maximum C-rate is 1C, experienced in the last part of the duty cycle, where the required maximum power of 80W leads to an increase in current intensity to compensate for the voltage decrease due to the decreasing SOC.

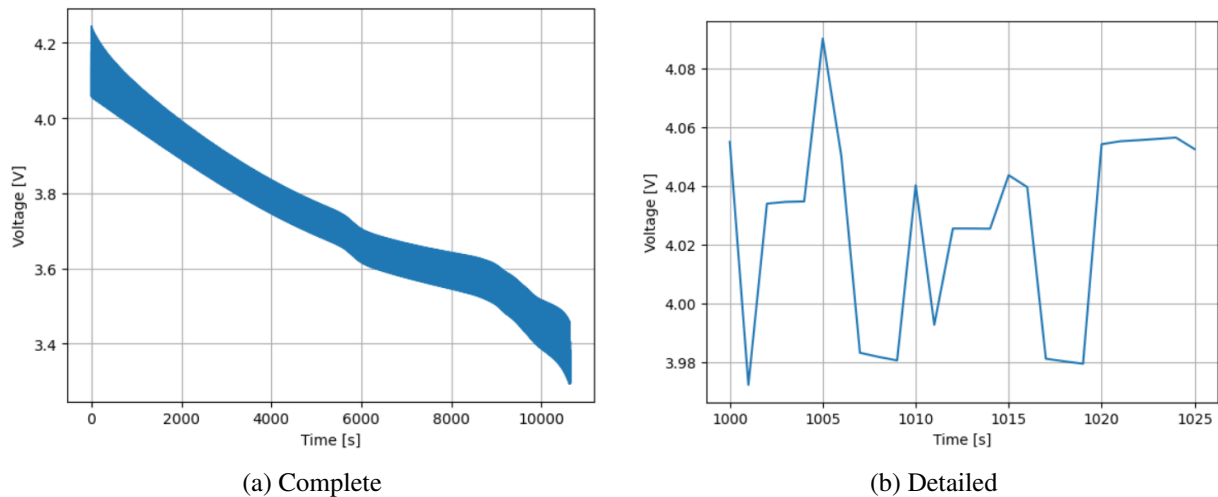


Figure 98: Forklift voltage duty cycle.

The heat produced during the cycle is reasonably higher than in previous

applications and more similar to the trends observed in the simulated tests. The heat production values range between 0 and 4W, with a "hollow" in the middle of the cycle. The estimated heat progressively increases, reaching a maximum of 14W at the end of the simulation. However, it is important to note that these values are not continuously emitted by the cells as in the previous simulations. Due to the high frequency of the duty cycle, the heat production follows the detailed plot shown in Figure 100b, with few peaks during the complete cycle. This makes the final part of the cycle less challenging than it appears, as there are periods of relatively low heat production.

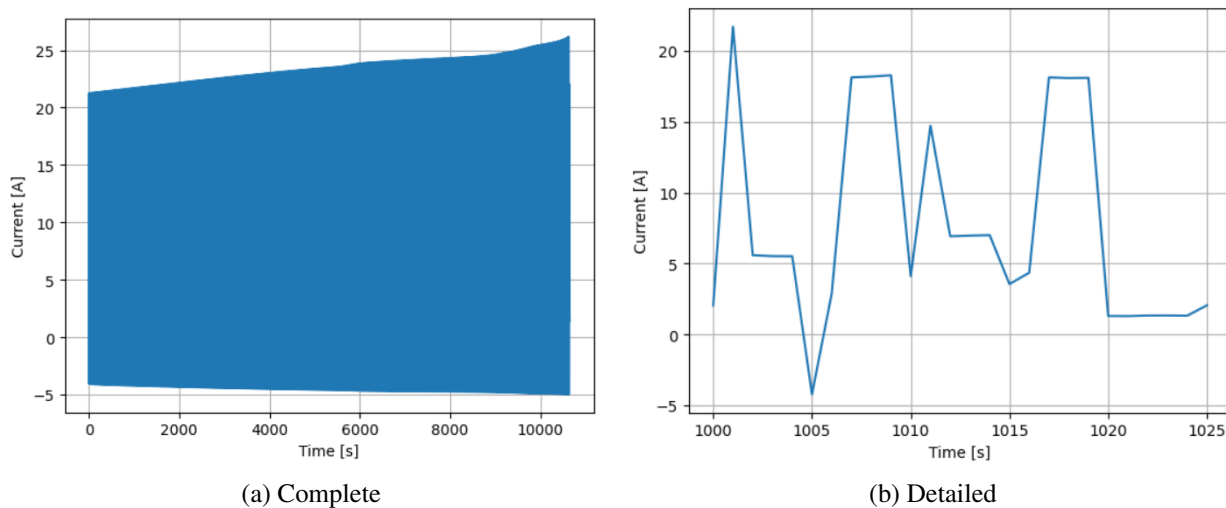


Figure 99: Forklift current duty cycle.

Figure 102 illustrates the temperature evolution of the jelly rolls throughout the entire simulation. Unlike the other simulations, this figure presents the temperature evolution of jelly rolls in cells 1, 4, 8, and 12; the reason for that choice is explained in the discussion on boundary conditions. The initial temperature of the cells ranges between 32°C and 36°C. The cooling system, detailed in section 3.7.3, is a serpentine cooling system with a constant coolant flow rate of 10g/s (values taken used by Choudhari et al. [25] and Zhang et al. [131] in similar applications).

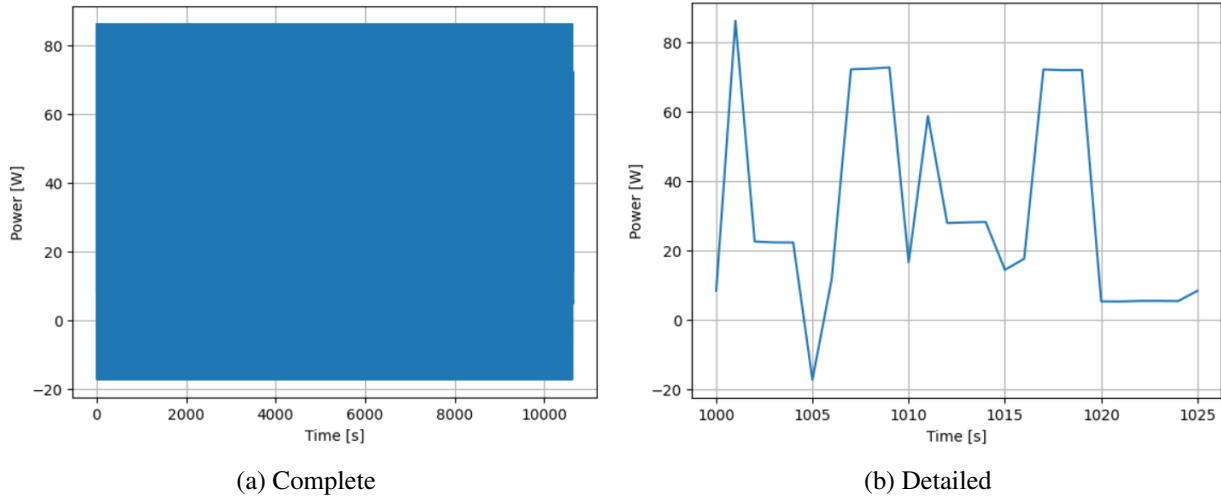


Figure 100: Forklift power duty cycle.

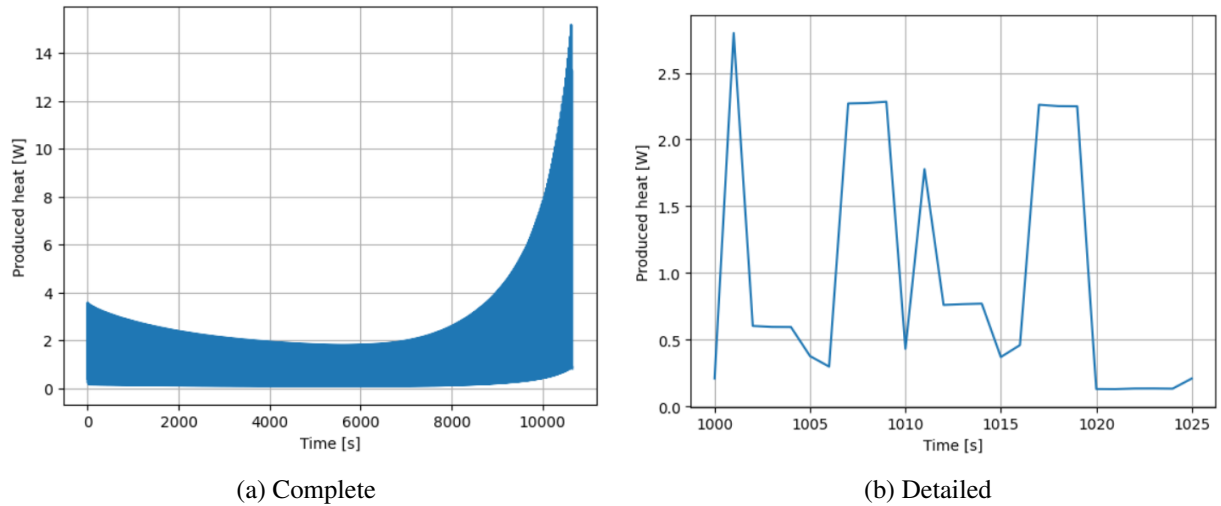


Figure 101: Forklift heat production duty cycle.

The coolant enters the system at a temperature of 25°C , assumed to match the ambient temperature. This is the only cooling mechanism for the entire module, simulating an adiabatic environment where convection is limited in effectiveness. Consequently, cooling is provided solely from the cell bottom by a coolant flow that first passes under cell 1 and then reaches cell 12. Consequently, monitoring these specific cells aims to assess how the cooling efficiency varies for cells located at different points along the serpentine.

The temperature evolution graph demonstrates that the cooling conditions are sufficient to ensure not only proper cooling of the jelly rolls but also remarkable cooling uniformity. Despite the characteristics of the system, the serpentine cooling

method effectively cools all recorded cells uniformly. Additionally, even starting from relatively higher temperatures, the jelly rolls are cooled down to temperatures comparable to that of the coolant. This result showcases the system’s effectiveness but warrants an important caveat. The coolant flow rate is derived from literature and does not provide a precise assessment of the system’s actual potential, especially considering that pressure drops are not accounted for in this study. Unfortunately, due to the high computational cost of this simulation, it was not possible to further investigate lower flow rates that might maintain the same cooling capacity while potentially reducing pressure drops.

The final consideration pertains to the latter part of the simulation. Unlike previous cases, this phase does not exhibit the expected temperature increase based on the estimated heat production. This discrepancy can be explained by the nature of the heat production peaks. Although the peak heat production is five times higher than the values experienced during most of the cycle, these conditions occur only briefly within each duty cycle. These peaks are sporadic rather than continuous, meaning that between peaks, the cells not subjected to prolonged periods of intense heating, have time to cool down and do not accumulate significant heat.

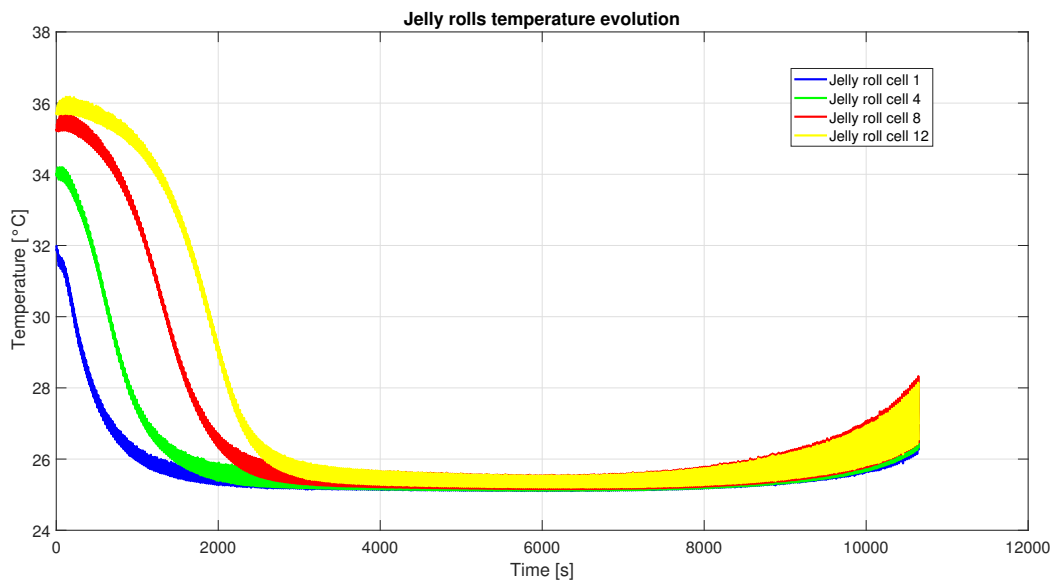


Figure 102: Jelly rolls temperature evolution in forklift duty cycle.

In this final case, the graphical output presented in Figure 103 provides significant insights into the temperature distribution within the module and the effectiveness of the cooling system at the end of the reference duty cycle. Despite cooling being provided only from the cell bottom, the temperature distribution within the module

remains fairly uniform, with a temperature variation of only a few degrees. This uniformity is observed both along the height of the cell case and across the length of the module.

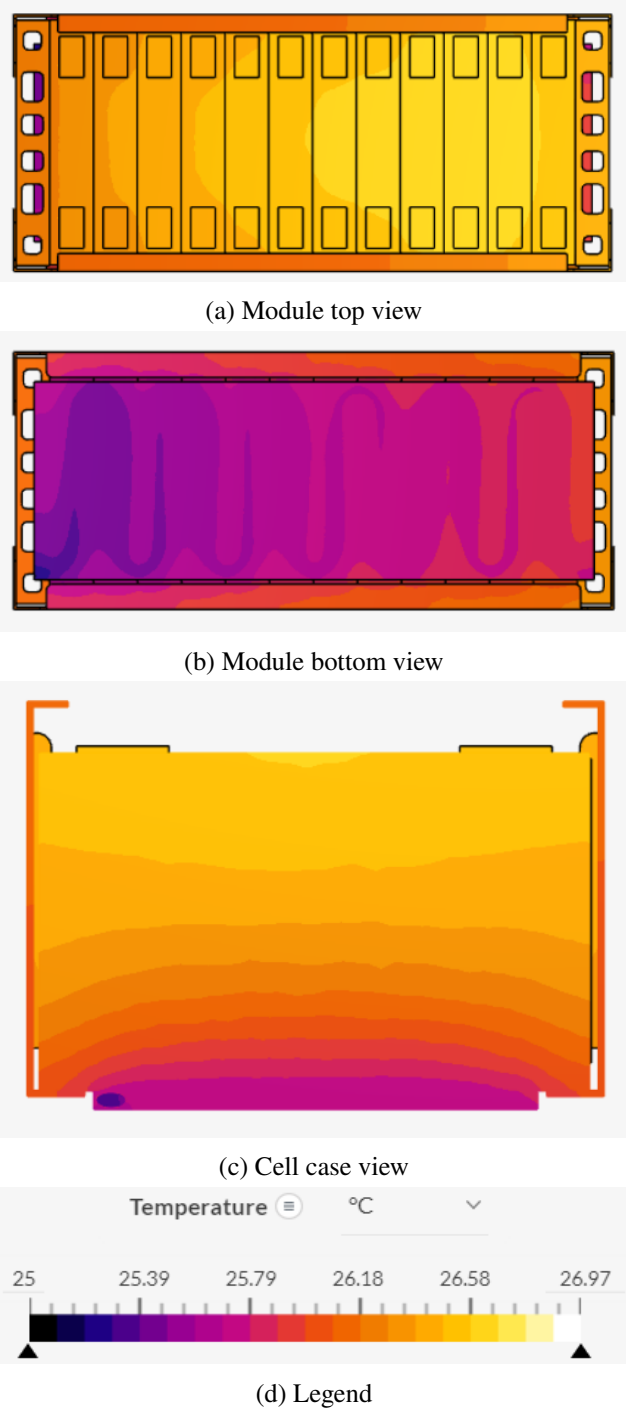


Figure 103: Module temperature at the end of forklift duty cycle.

The model allows for visualization of the heat flux from the top to the bottom

of the cell, showing a progressive decrease in temperature as the distance to the cooling plate decreases. A similar trend is observed for the temperature gradient along the length of the module and the coolant temperature. Cells closer to the coolant entrance receive slightly better cooling, while cells farther from the entrance experience higher temperatures. Conversely, the coolant temperature, which starts at 25°C, progressively increases as it moves through the module, due to cells cooling along its path.

The outcome of these simulations is very clear: the battery module is valuable in all the tested duty cycles. The modules configurations, designed to define new battery packs, demonstrates their capability to extensively satisfy the needs of the chosen second life applications, ensuring level of power and discharge rates that widely safe guard the remaining capacity of the cells. The resultant thermal performance of the module, outcome of the thermal simulations, demonstrates its value in all the second life scenarios conditions, even if really challenging in cooling as in the case of the solar firming and electric forklift.

5 Conclusion

In this thesis, a critical and complex engineering challenge was addressed: the precise evaluation of characteristics and the thermal performance of a repurposed PHEV's module for second-life applications, despite limited experimental resources. An innovative and effective methodology was employed, utilizing a validated coupled electrochemical-thermal model to determine the module's suitability for the intended second-life scenarios.

The SPM_e was implemented using PyBaMM software, encompassing all the fundamental PDEs of the model. A comprehensive set of 30 parameters was required for the model's complete resolution. Initially, these parameters were sourced from accredited literature and subsequently refined through three steps: incorporating parameters from the available datasheet, measuring geometric parameters, and optimizing through an algorithm. The model was validated using two types of experimental tests: CC-CV charge / CC discharge cycles with C-rates ranging from 0.1C to 1.5C at room temperature, and two GITTs curves at 40A, conducted at 25°C and 45°C. The model demonstrated high average accuracy in replicating the experimental data, particularly at elevated temperatures, with overall error values within a few percentage points. However, the accuracy in matching discharge curves decreased as current intensity increased, leading to minor oscillations and errors up to 20mV at 40A. Additionally, the model struggled to predict cell behavior in the final stages of the GITT curves, resulting in errors up to 4% at 45°C and up to 6% at 25°C. Despite these limitations, the model's ability to reproduce cell behavior was deemed sufficiently accurate for the purposes of this study.

The thermal model comprised several components. The module was replicated in CAD software with some simplifications in cell design, where only the jelly roll, as a single entity, acted as the heat source. Heat production was estimated using a PyBaMM thermal sub-model. These elements facilitated the implementation of thermal simulations within SimScale software, capable of simulating various boundary conditions. The two models are interdependent since the heat produced during a cycle, estimated by means of the thermal sub-model, depends on cell's temperature, which is the output of the thermal simulation that, in turn, requires heat production as input. Consequently, at least two iterations of this loop were necessary for each simulation to achieve convergence to appropriate results. The coupled model was validated through two thermal tests: the module, enclosed in a polystyrene adiabatic box, underwent a discharge cycle at 30A at two different temperatures:

25°C and 46°C. The heating and cooling conditions experienced by the module within the box were replicated in SimScale, allowing for a comparison with the recorded temperature evolution during the tests. The coupled model exhibited good accuracy in matching the temperature evolution, with percentage errors within 2% for most of the tests. The only exception was in the final part of the cycle (the last five state of charge points), where the model overestimated heat production by up a maximum of 8%. This overestimation was not a significant issue for the project's objectives, as the final state of charge instants are not often encountered in several applications and, more importantly, it favors safety by overrating the cooling required to control temperature evolution.

The final phase of the project involved evaluating the module's suitability for second-life applications. The selected ones were solar firming, residential PV, and electric forklift. Operating conditions, including pack configuration and cooling, and a reference duty cycle were chosen for each application. These elements enabled simulations to evaluate the designed pack's performance in the new conditions. The results were particularly encouraging, demonstrating the battery's capability to follow the chosen duty cycle with limited current intensity and sufficient capacity. Most importantly, the pack exhibited exceptional thermal performance under all simulated conditions, with poor heating and safe temperature evolution, thus confirming its suitability for the selected second-life scenarios with a significant margin.

6 Possible future developments

The multidisciplinary and the inner characteristics of this thesis work open several opportunities for future developments.

One possible path includes enhancing the electrochemical model to address its significant limitations. Overall accuracy may be increased through more specific experimental tests and further optimization efforts, which would help reducing oscillations and errors, especially at higher current rates. Additionally, accuracy during the final part of dynamic cycles could be improved by better modeling the cell's non-linear behavior, leading to a closer fit with experimental data and improved heat estimation accuracy comparable to other cycle parts.

Another aspect involves the cell's thermal behavior, which has only been analyzed and tested at room and high temperatures. However, lithium-ion batteries are also highly sensitive to low temperatures, which can cause significant aging phenomena during both charging and discharging. Including modeling and management of these conditions would make the model more comprehensive.

Furthermore, the model could be integrated with a basic aging prediction scheme. This study only discussed external factors limiting aging, neglecting those related to the battery's normal operation. Predicting the aging trajectory of the battery for each second-life scenario would be particularly useful in estimating service duration and possibly overestimating the required battery capacity for a given duration target.

The last additional improvement could be a more accurate representation of the cell as a heat source. In this study, the jelly roll was simplified as the sole heat source, but in reality, other components, such as current collectors, also generate significant heat. Consequently, evaluating and modeling these additional heat sources would result in more accurate thermal simulations and temperature distributions within the module.

References

- [1] Mohamed Abdel-Monem, Omar Hegazy, Noshin Omar, Khiem Trad, Sven De Breucker, Peter Van Den Bossche, and Joeri Van Mierlo. Design and analysis of generic energy management strategy for controlling second-life battery systems in stationary applications. *Energies*, 9(11):889, 2016.
- [2] Maheshwari Adaikkappan and Nageswari Sathiyamoorthy. Modeling, state of charge estimation, and charging of lithium-ion battery in electric vehicle: view. *International Journal of Energy Research*, 46(3):2141–2165, 2022.
- [3] Mohsen Akbarzadeh, Theodoros Kalogiannis, Joris Jaguemont, Jiacheng He, Lu Jin, Maitane Berecibar, and Joeri Van Mierlo. Thermal modeling of a high-energy prismatic lithium-ion battery cell and module based on a new thermal characterization methodology. *Journal of Energy Storage*, 32:101707, 2020.
- [4] Levke Albertsen, Jessika Luth Richter, Philip Peck, Carl Dalhammar, and Andrius Plepys. Circular business models for electric vehicle lithium-ion batteries: An analysis of current practices of vehicle manufacturers and policies in the eu. *Resources, conservation and recycling*, 172:105658, 2021.
- [5] Mohammad Alipour, Carlos Ziebert, Fiorentino Valerio Conte, and Riza Kizilel. A review on temperature-dependent electrochemical properties, aging, and performance of lithium-ion cells. *Batteries*, 6(3):35, 2020.
- [6] Hanjiro Ambrose, Dimitry Gershenson, Alexander Gershenson, and Daniel Kammen. Driving rural energy access: a second-life application for electric-vehicle batteries. *Environmental Research Letters*, 9(9):094004, 2014.
- [7] Sabri Baazouzi, Niklas Feistel, Johannes Wanner, Inga Landwehr, Alexander Fill, and Kai Peter Birke. Design, properties, and manufacturing of cylindrical li-ion battery cells—a generic overview. *Batteries*, 9(6):309, 2023.
- [8] Farid Bahiraei, Amir Fartaj, and Gholam-Abbas Nazri. Electrochemical-thermal modeling to evaluate active thermal management of a lithium-ion battery module. *Electrochimica Acta*, 254:59–71, 2017.
- [9] Emmanuel Balogun, Elizabeth Buechler, Siddharth Bhela, Simona Onori, and Ram Rajagopal. Ev-ecosim: A grid-aware co-simulation platform for

- the design and optimization of electric vehicle charging infrastructure. *IEEE Transactions on Smart Grid*, 2023.
- [10] Todd M Bandhauer, Srinivas Garimella, and Thomas F Fuller. A critical review of thermal issues in lithium-ion batteries. *Journal of the electrochemical society*, 158(3):R1, 2011.
- [11] S Barcellona and L Piegari. Effect of current on cycle aging of lithium ion batteries. *Journal of Energy Storage*, 29:101310, 2020.
- [12] D Bernardi, E Pawlikowski, and John Newman. A general energy balance for battery systems. *Journal of the electrochemical society*, 132(1):5, 1985.
- [13] Christoph R Birkl, Matthew R Roberts, Euan McTurk, Peter G Bruce, and David A Howey. Degradation diagnostics for lithium ion cells. *Journal of Power Sources*, 341:373–386, 2017.
- [14] Younes Boujoudar, Hassan Elmoussaoui, and Tijani Lamhamdi. Lithium-ion batteries modeling and state of charge estimation using artificial neural network. *International Journal of Electrical and Computer Engineering*, 9(5):3415, 2019.
- [15] Claudio Brivio. Battery energy storage systems: Modelling, applications and design criteria. 2017.
- [16] Alberto Broatch, Pablo Olmeda, Xandra Margot, and Luca Agizza. A generalized methodology for lithium-ion cells characterization and lumped electro-thermal modelling. *Applied Thermal Engineering*, 217:119174, 2022.
- [17] Ferran Brosa Planella, Weilong Ai, Adam M Boyce, Abir Ghosh, Ivan Korotkin, Smita Sahu, Valentin Sulzer, Robert Timms, Thomas G Tranter, Maxim Zyskin, et al. A continuum of physics-based lithium-ion battery models reviewed. *Progress in Energy*, 4(4):042003, 2022.
- [18] Maximilian Bruch, Lluís Millet, Julia Kowal, and Matthias Vetter. Novel method for the parameterization of a reliable equivalent circuit model for the precise simulation of a battery cell’s electric behavior. *Journal of Power Sources*, 490:229513, 2021.
- [19] Lluç Canals Casals, Beatriz Amante García, and Maria Margarita González Benítez. Aging model for re-used electric vehicle batteries in

- second life stationary applications. In *Project Management and Engineering Research: AEIPRO 2016*, pages 139–151. Springer, 2017.
- [20] M Castle, G Richardson, and JM Foster. Understanding rapid charge and discharge in nano-structured lithium iron phosphate cathodes. *European Journal of Applied Mathematics*, 33(2):328–368, 2022.
- [21] İrfan Çetin, Ekrem Sezici, Mustafa Karabulut, Emre Avci, and Fikret Polat. A comprehensive review of battery thermal management systems for electric vehicles. *Proceedings of the Institution of Mechanical Engineers, Part E: Journal of Process Mechanical Engineering*, 237(3):989–1004, 2023.
- [22] Ephrem Chemali, Phillip J Kollmeyer, Matthias Preindl, and Ali Emadi. State-of-charge estimation of li-ion batteries using deep neural networks: A machine learning approach. *Journal of Power Sources*, 400:242–255, 2018.
- [23] Chang-Hui Chen, Ferran Brosa Planella, Kieran O’regan, Dominika Gastol, W Dhammika Widanage, and Emma Kendrick. Development of experimental techniques for parameterization of multi-scale lithium-ion battery models. *Journal of The Electrochemical Society*, 167(8):080534, 2020.
- [24] Kai Chen, Zeyu Li, Yiming Chen, Shuming Long, Junsheng Hou, Mengxuan Song, and Shuangfeng Wang. Design of parallel air-cooled battery thermal management system through numerical study. *Energies*, 10(10):1677, 2017.
- [25] VG Choudhari, AS Dhoble, and TM Sathe. A review on effect of heat generation and various thermal management systems for lithium ion battery used for electric vehicle. *Journal of Energy Storage*, 32:101729, 2020.
- [26] K Darcovich, DD MacNeil, S Recoskie, and B Kenney. Coupled electrochemical and thermal battery models for thermal management of prismatic automotive cells. *Applied Thermal Engineering*, 133:566–575, 2018.
- [27] Xu Deng and Tao Lv. Power system planning with increasing variable renewable energy: A review of optimization models. *Journal of Cleaner Production*, 246:118962, 2020.
- [28] Shicong Ding, Yiding Li, Haifeng Dai, Li Wang, and Xiangming He. Accurate model parameter identification to boost precise aging prediction of lithium-ion batteries: A review. *Advanced Energy Materials*, 13(39):2301452, 2023.

- [29] Erik Emilsson and Lisbeth Dahllöf. Lithium-ion vehicle battery production-status 2019 on energy use, co2 emissions, use of metals, products environmental footprint, and recycling, 2019.
- [30] Siamak Farhad, M Younessi-Sinaki, MR Golriz, and F Hamdullahpur. Exergy analysis and performance evaluation of cng to lng converting process. *International Journal of Exergy*, 5(2):164–176, 2008.
- [31] F.Lambert. Breakdown of raw materials in tesla’s batteries and possible bottlenecks. Nov.01,2016.
- [32] Ping Fu, Lan Zhao, Xuguang Wang, Jian Sun, and Zhicheng Xin. A review of cooling technologies in lithium-ion power battery thermal management systems for new energy vehicles. *Processes*, 11(12), 2023.
- [33] Alice Gaehring, Rhea Kripalani, Dakota Neuls, Owen Rondeau, and Naomi Schlag. Modeling li-ion battery behavior to identify safety limits. In *2021 IEEE MIT Undergraduate Research Technology Conference (URTC)*, pages 1–5. IEEE, 2021.
- [34] B Gohla-Neudecker, M Bowler, and S Mohr. Battery 2 nd life: Leveraging the sustainability potential of evs and renewable energy grid integration. In *2015 International Conference on Clean Electrical Power (ICCEP)*, pages 311–318. IEEE, 2015.
- [35] Bangjun Guo, Chenghao Liu, Yizhao Gao, Chong Zhu, Xi Zhang, Xiaole Ma, and Fang Wang. A combining electrochemical model for lifepo4-graphite lithium-ion battery considering cathode heterogeneous solid phase phenomenon. *International Journal of Energy Research*, 46(11):15231–15243, 2022.
- [36] Yu Guo, Yishu Qiu, Bo Lei, Yue Wu, Youjie Shi, Wenjiong Cao, Hecheng Liu, and Fangming Jiang. Modeling and analysis of liquid-cooling thermal management of an in-house developed 100 kw/500 kwh energy storage container consisting of lithium-ion batteries retired from electric vehicles. *Applied Thermal Engineering*, 232:121111, 2023.
- [37] Mohammed Hussein Saleh Mohammed Haram, Jia Woon Lee, Gobbi Ramasamy, Eng Eng Ngu, Siva Priya Thiagarajah, and Yuen How Lee. Feasibility

- of utilising second life ev batteries: Applications, lifespan, economics, environmental impact, assessment, and challenges. *Alexandria Engineering Journal*, 60(5):4517–4536, 2021.
- [38] J Hawkins, S Willard, B Arellano, A Mammoli, and JJ Simmins. Storage for simultaneous voltage smoothing and energy shifting. In *2014 IEEE PES T&D Conference and Exposition*, pages 1–5. IEEE, 2014.
- [39] CX He, QL Yue, MC Wu, Qing Chen, and TS Zhao. A 3d electrochemical-thermal coupled model for electrochemical and thermal analysis of pouch-type lithium-ion batteries. *International Journal of Heat and Mass Transfer*, 181:121855, 2021.
- [40] Elham Hosseinzadeh, Ronny Genieser, Daniel Worwood, Anup Barai, James Marco, and Paul Jennings. A systematic approach for electrochemical-thermal modelling of a large format lithium-ion battery for electric vehicle application. *Journal of power sources*, 382:77–94, 2018.
- [41] Xuan Hou, Jun Wang, Tao Huang, Tao Wang, and Peng Wang. Smart home energy management optimization method considering energy storage and electric vehicle. *IEEE access*, 7:144010–144020, 2019.
- [42] 2024 [https://cleantechnica.com/2015/04/26/electric-car history/](https://cleantechnica.com/2015/04/26/electric-car-history/), last accessed on July 15.
- [43] 2024 <https://dieselnet.com/tech/energy.powertrains.batteries.php>, last accessed on July 15.
- [44] 2024 [https://energydigital.com/renewable-energy/huawei-launches-solar-pv-and-energy-storage solutions](https://energydigital.com/renewable-energy/huawei-launches-solar-pv-and-energy-storage-solutions), last accessed on July 15.
- [45] 2024 https://it.wikipedia.org/wiki/La_Jamais-Contente, last accessed on July 15.
- [46] 2024 [https://letstalkscience.ca/educational-resources/stem-explained/how-does-a-lithium-ion-battery work](https://letstalkscience.ca/educational-resources/stem-explained/how-does-a-lithium-ion-battery-work), last accessed on July 15.
- [47] <https://pybamm.org/>.
- [48] 2024 [https://techlar.weebly.com/batteries-parallel-and series.html](https://techlar.weebly.com/batteries-parallel-and-series.html), last accessed on July 15.
- [49] 2024 [https://us.fox ess.com/](https://us.foxess.com/), last accessed on July 15.

- [50] 2024 <https://www.batemo.com/products/batemo-cell-explorer/unknown-manufacturer-honda-clarity/>, last accessed on July 15.
- [51] 2024 <https://www.batemo.com/products/batemo-cell-explorer/unknown-manufacturer-honda-clarity/>, last accessed on July 15.
- [52] 2024 <https://www.deltamodtech.com/blog/battery-electrode-coating/>, last accessed on July 15.
- [53] 2024 <https://www.ebay.com/itm/225304675424>, last accessed on July 15.
- [54] 2024 <https://www.gettyimages.com.mx/detail/fotografnoticias/143064462?language=it>, last accessed on July 15.
- [55] 2024 <https://www.hgtv.com/design/remodel/mechanical-systems/solar-power-101>, last accessed on July 15.
- [56] 2024 <https://www.simscale.com/>, last accessed on July 15.
- [57] 2024 <https://www.simscale.com/docs/analysis-types/conjugate-heat-transfer-ibm/>, last accessed on July 15.
- [58] 2024 <https://www.simscale.com/docs/simulation-setup/global-settings/k-omega-sst/>, last accessed on July 15.
- [59] 2024 <https://www.simscale.com/docs/tutorials/thermal-management-cht-analysis-electronics-box/>, last accessed on July 15.
- [60] 2024 <https://www.townsendhonda.com/2019-honda-clarity-plug-in-hybrid/>, last accessed on July 15.
- [61] 2024 <https://www.toyotaforklift.ca/en>, last accessed on July 15.
- [62] 2024 <https://www.toyotaforklift.com/lifts/electric-motor-rider-forklifts/core-electric-forklift>, last accessed on July 15.
- [63] 2024 <https://www.tycorun.com/blogs/news/what-is-liquid-cooled-battery-cooling>, last accessed on July 15.
- [64] Xiaosong Hu, Xinchun Deng, Feng Wang, Zhongwei Deng, Xianke Lin, Remus Teodorescu, and Michael G Pecht. A review of second-life lithium-ion batteries for stationary energy storage applications. *Proceedings of the IEEE*, 110(6):735–753, 2022.

- [65] Gary Hunt et al. Usabc electric vehicle battery test procedures manual. *United States Department of Energy: Washington, DC, USA*, 1996.
- [66] Matthew J Hunt, Ferran Brosa Planella, Florian Theil, and W Dhammika Widanage. Derivation of an effective thermal electrochemical model for porous electrode batteries using asymptotic homogenisation. *Journal of Engineering Mathematics*, 122:31–57, 2020.
- [67] Owais Iqbal. Fundamentals of automotive engineering. *Univesity of Windosr*, 2023.
- [68] Unai Iraola, Iosu Aizpuru, Jose Maria Canales, Ander Etxeberria, and Iñigo Gil. Methodology for thermal modelling of lithium-ion batteries. In *IECON 2013-39th Annual Conference of the IEEE Industrial Electronics Society*, pages 6752–6757. IEEE, 2013.
- [69] R. Irle. Global ev sales for 2021 h1. 2021.
- [70] Hayder Mohammad Jaffal, Nabeel Sameer Mahmoud, Ahmed Abdulnabi Imran, and Ala Hasan. Performance enhancement of a novel serpentine channel cooled plate used for cooling of li-ion battery module. *International Journal of Thermal Sciences*, 184:107955, 2023.
- [71] Nader Javani, I Dincer, GF Naterer, and GL Rohrauer. Modeling of passive thermal management for electric vehicle battery packs with pcm between cells. *Applied Thermal Engineering*, 73(1):307–316, 2014.
- [72] Guiwen Jiang, Ling Zhuang, Qinghua Hu, Ziqiang Liu, and Juhua Huang. An investigation of heat transfer and capacity fade in a prismatic li-ion battery based on an electrochemical-thermal coupling model. *Applied Thermal Engineering*, 171:115080, 2020.
- [73] Dipti Kamath, Siddharth Shukla, Renata Arsenault, Hyung Chul Kim, and Annick Anctil. Evaluating the cost and carbon footprint of second-life electric vehicle batteries in residential and utility-level applications. *Waste Management*, 113:497–507, 2020.
- [74] Phattara Khumprom and Nita Yodo. A data-driven predictive prognostic model for lithium-ion batteries based on a deep learning algorithm. *Energies*, 12(4):660, 2019.

- [75] Ui Seong Kim, Chee Burm Shin, and Chi-Su Kim. Effect of electrode configuration on the thermal behavior of a lithium-polymer battery. *Journal of Power Sources*, 180(2):909–916, 2008.
- [76] Jan Kleiner, Lidiya Komsiyiska, Gordon Elger, and Christian Endisch. Modelling of 3d temperature behavior of prismatic lithium-ion cell with focus on experimental validation under battery electric vehicle conditions. In *2019 25th International Workshop on Thermal Investigations of ICs and Systems (THERMINIC)*, pages 1–6. IEEE, 2019.
- [77] Sergey A Krachkovskiy, Jamie M Foster, J David Bazak, Bruce J Balcom, and Gillian R Goward. Operando mapping of li concentration profiles and phase transformations in graphite electrodes by magnetic resonance imaging and nuclear magnetic resonance spectroscopy. *The Journal of Physical Chemistry C*, 122(38):21784–21791, 2018.
- [78] Gregory B Less, Jung Hwan Seo, S Han, Ann Marie Sastry, Jochen Zausch, Arnulf Latz, Sebastian Schmidt, Christian Wieser, Dirk Kehrwald, and Stefan Fell. Micro-scale modeling of li-ion batteries: parameterization and validation. *Journal of The Electrochemical Society*, 159(6):A697, 2012.
- [79] Shuangqi Li, Pengfei Zhao, Chenghong Gu, Siqi Bu, Jianwei Li, and Shuang Cheng. Modeling and mitigating the cycle aging cost of vehicle batteries in energy transportation nexus. *IEEE Transactions on Smart Grid*, 2023.
- [80] Weihan Li, Decheng Cao, Dominik Jöst, Florian Ringbeck, Matthias Kuipers, Fabian Frie, and Dirk Uwe Sauer. Parameter sensitivity analysis of electrochemical model-based battery management systems for lithium-ion batteries. *Applied Energy*, 269:115104, 2020.
- [81] Bor Yann Liaw, Rudolph G Jungst, Angel Urbina, and Thomas L Paez. Modeling of battery life i. the equivalent circuit model (ecm) approach. *Tech. Rep.*, 2003.
- [82] Iker Lopetegi, Gregory L Plett, M Scott Trimboli, Josu Yeregui, Laura Oca, Clara Rojas, Eduardo Miguel, and Unai Iraola. Lithium-ion battery aging prediction with electrochemical models: P2d vs spme. In *2023 IEEE Vehicle Power and Propulsion Conference (VPPC)*, pages 1–7. IEEE, 2023.

- [83] Valentina Lucaferri, Michele Quercio, Antonino Laudani, and Francesco Riganti Fulginei. A review on battery model-based and data-driven methods for battery management systems. *Energies*, 16(23):7807, 2023.
- [84] Peter D Lund, Juuso Lindgren, Jani Mikkola, and Jyri Salpakari. Review of energy system flexibility measures to enable high levels of variable renewable electricity. *Renewable and sustainable energy reviews*, 45:785–807, 2015.
- [85] Shuai Ma, Modi Jiang, Peng Tao, Chengyi Song, Jianbo Wu, Jun Wang, Tao Deng, and Wen Shang. Temperature effect and thermal impact in lithium-ion batteries: A review. *Progress in Natural Science: Materials International*, 28(6):653–666, 2018.
- [86] Scott G Marquis, Valentin Sulzer, Robert Timms, Colin P Please, and S Jon Chapman. An asymptotic derivation of a single particle model with electrolyte. *Journal of The Electrochemical Society*, 166(15):A3693, 2019.
- [87] Egoitz Martinez-Laserna, Iñigo Gandiaga, Elixabet Sarasketa-Zabala, Julia Badedá, D-I Stroe, Maciej Swierczynski, and Ander Goikoetxea. Battery second life: Hype, hope or reality? a critical review of the state of the art. *Renewable and Sustainable Energy Reviews*, 93:701–718, 2018.
- [88] Egoitz Martinez-Laserna, Elixabet Sarasketa-Zabala, Igor Villarreal Sarria, Daniel-Ioan Stroe, Maciej Swierczynski, Alexander Warnecke, Jean-Marc Timmermans, Shovon Goutam, Noshin Omar, and Pedro Rodriguez. Technical viability of battery second life: A study from the ageing perspective. *IEEE Transactions on Industry Applications*, 54(3):2703–2713, 2018.
- [89] Egoitz Martinez-Laserna, Elixabet Sarasketa-Zabala, D-I Stroe, Maciej Swierczynski, Alexander Warnecke, Jean-Marc Timmermans, Shovon Goutam, and Pedro Rodriguez. Evaluation of lithium-ion battery second life performance and degradation. In *2016 IEEE Energy Conversion Congress and Exposition (ECCE)*, pages 1–7. IEEE, 2016.
- [90] M Waseem Marzook, Alastair Hales, Yatish Patel, Gregory Offer, and Monica Marinescu. Thermal evaluation of lithium-ion batteries: Defining the cylindrical cell cooling coefficient. *Journal of Energy Storage*, 54:105217, 2022.
- [91] Jinhao Meng, Guangzhao Luo, Mattia Ricco, Maciej Swierczynski, Daniel-Ioan Stroe, and Remus Teodorescu. Overview of lithium-ion battery modeling

- methods for state-of-charge estimation in electrical vehicles. *Applied sciences*, 8(5):659, 2018.
- [92] Fabian Menz, Marius Bauer, Olaf Böse, Moritz Pausch, and Michael A Danzer. Investigating the thermal runaway behaviour of fresh and aged large prismatic lithium-ion cells in overtemperature experiments. *Batteries*, 9(3):159, 2023.
- [93] Emanuele Michelini, Patrick Höschele, Florian Ratz, Michael Stadlbauer, Werner Rom, Christian Ellersdorfer, and Jörg Moser. Potential and most promising second-life applications for automotive lithium-ion batteries considering technical, economic and legal aspects. *Energies*, 16(6):2830, 2023.
- [94] Celina Mikolajczak, Michael Kahn, Kevin White, and Richard Thomas Long. *Lithium-ion batteries hazard and use assessment*. Springer Science & Business Media, 2012.
- [95] Peyman Mohtat, Suhak Lee, Valentin Sulzer, Jason B Siegel, and Anna G Stefanopoulou. Differential expansion and voltage model for li-ion batteries at practical charging rates. *Journal of The Electrochemical Society*, 167(11):110561, 2020.
- [96] Tomás Montes, Maite Etxandi-Santolaya, Josh Eichman, Victor José Ferreira, Lluís Trilla, and Cristina Corchero. Procedure for assessing the suitability of battery second life applications after ev first life. *Batteries*, 8(9):122, 2022.
- [97] Piotr Mroz, Piotr Gorny, Martyna Ekiert, and Tadeusz Uhl. An estimation of lithium-ion battery state of health-ageing-included modelling and experimental studies. *Diagnostyka*, 17, 2016.
- [98] Kirill Murashko et al. Thermal modelling of commercial lithium-ion batteries. 2016.
- [99] Ashkan Nazari and Siamak Farhad. Heat generation in lithium-ion batteries with different nominal capacities and chemistries. *Applied Thermal Engineering*, 125:1501–1517, 2017.
- [100] N.Nhede. End-of-life electric vehicle batteries: Recycling or second-life? 2020.

- [101] Linda Olsson, Sara Fallahi, Maria Schnurr, Derek Diener, and Patricia Van Loon. Circular business models for extended ev battery life. *Batteries*, 4(4):57, 2018.
- [102] Alexander Otto, Sven Rzepka, Thomas Mager, Bernd Michel, Claudio Lanciotti, Thomas Günther, and Olfa Kanoun. Battery management network for fully electrical vehicles featuring smart systems at cell and pack level. In *Advanced Microsystems for Automotive Applications 2012: Smart Systems for Safe, Sustainable and Networked Vehicles*, pages 3–14. Springer, 2012.
- [103] Ahmad A Pesaran. Battery thermal management in ev and hevs: issues and solutions. *Battery Man*, 43(5):34–49, 2001.
- [104] Andrea Pozzi, Gabriele Ciaramella, Stefan Volkwein, and Davide M Raimondo. Optimal design of experiments for a lithium-ion cell: parameters identification of an isothermal single particle model with electrolyte dynamics. *Industrial & Engineering Chemistry Research*, 58(3):1286–1299, 2018.
- [105] ZG Qu, WQ Li, and WQ Tao. Numerical model of the passive thermal management system for high-power lithium ion battery by using porous metal foam saturated with phase change material. *International Journal of hydrogen energy*, 39(8):3904–3913, 2014.
- [106] Lin Rao and John Newman. Heat-generation rate and general energy balance for insertion battery systems. *Journal of the Electrochemical Society*, 144(8):2697, 1997.
- [107] Vittorio Ravello. E-powertrain components course materials. *Politecnico di Torino*, 2023.
- [108] Jorn M Reniers, Grietus Mulder, Sina Ober-Blöbaum, and David A Howey. Improving optimal control of grid-connected lithium-ion batteries through more accurate battery and degradation modelling. *Journal of Power Sources*, 379:91–102, 2018.
- [109] Venu Sangwan, Avinash Sharma, Rajesh Kumar, and Akshay K Rathore. High fidelity equivalent circuit model parameter extraction for characterization and simulation of li-ion cells in battery electric vehicles. *Electric Power Components and Systems*, 46(14-15):1672–1685, 2018.

- [110] Samveg Saxena, Caroline Le Floch, Jason MacDonald, and Scott Moura. Quantifying ev battery end-of-life through analysis of travel needs with vehicle powertrain models. *Journal of Power Sources*, 282:265–276, 2015.
- [111] Alexander P Schmidt, Matthias Bitzer, Árpád W Imre, and Lino Guzzella. Experiment-driven electrochemical modeling and systematic parameterization for a lithium-ion battery cell. *Journal of Power Sources*, 195(15):5071–5080, 2010.
- [112] D Schoenwald and J Ellison. Determination of duty cycle for energy storage systems in a renewables (solar) firming application, sand2016-3636. *Sandia National Laboratories, Albuquerque, New Mexico*, 87185, 2016.
- [113] Mohammad Shahjalal, Probir Kumar Roy, Tamanna Shams, Ashley Fly, Jahedul Islam Chowdhury, Md Rishad Ahmed, and Kailong Liu. A review on second-life of li-ion batteries: Prospects, challenges, and issues. *Energy*, 241:122881, 2022.
- [114] Joshua Smith, Michael Hinterberger, Peter Hable, and Juergen Koehler. Simulative method for determining the optimal operating conditions for a cooling plate for lithium-ion battery cell modules. *Journal of Power Sources*, 267:784–792, 2014.
- [115] V Sulzer, SG Marquis, R Timms, M Robinson, and SJ Chapman. Python battery mathematical modelling (pybamm), j. open res. softw., 9 (2021), 14.
- [116] Yasong Sun, Ruihuai Bai, and Jing Ma. Design and thermal analysis of a new topological cooling plate for prismatic lithium battery thermal management. *Applied Thermal Engineering*, 219:119547, 2023.
- [117] Aikun Tang, Jianming Li, Liusheng Lou, Chunxian Shan, and Xuezhen Yuan. Optimization design and numerical study on water cooling structure for power lithium battery pack. *Applied Thermal Engineering*, 159:113760, 2019.
- [118] D Thiruvonasundari and K Deepa. Electric vehicle battery modelling methods based on state of charge–review. *J. Green Eng*, 10(1):24–61, 2020.
- [119] Ben Thompson. *Repurposing electric vehicle batteries in a mixed array for grid storage*. PhD thesis, 2018.

- [120] Robert Timms, Scott G. Marquis, Valentin Sulzer, Colin P. Please, and S. Jonathan Chapman. Asymptotic reduction of a lithium-ion pouch cell model. *SIAM Journal on Applied Mathematics*, 81(3):765–788, 2021.
- [121] Sai Datta V Rao Vadlamudi, Volkan Kumtepel, Selin Ozcira, and Anshuman Tripathi. Hybrid energy storage power allocation and motor control for electric forklifts. In *2016 Asian Conference on Energy, Power and Transportation Electrification (ACEPT)*, pages 1–5. IEEE, 2016.
- [122] Chris White and Lukas G Swan. Pack-level performance of electric vehicle batteries in second-life electricity grid energy services. *Journal of Energy Storage*, 57:106265, 2023.
- [123] Billy Wu, Vladimir Yufit, Monica Marinescu, Gregory J Offer, Ricardo F Martinez-Botas, and Nigel P Brandon. Coupled thermal–electrochemical modelling of uneven heat generation in lithium-ion battery packs. *Journal of Power Sources*, 243:544–554, 2013.
- [124] Meng Xu, Zhuqian Zhang, Xia Wang, Li Jia, and Lixin Yang. A pseudo three-dimensional electrochemical–thermal model of a prismatic lifepo4 battery during discharge process. *Energy*, 80:303–317, 2015.
- [125] Tomoya Yamagishi and Takashi Ishikura. Development of electric powertrain for clarity plug-in hybrid. *SAE International Journal of Alternative Powertrains*, 7(3):323–334, 2018.
- [126] Y.Kotak. End of electric vehicle batteries:reuse vs. recyle. Apr.2021.
- [127] Kelvin O Yoro and Michael O Daramola. Co2 emission sources, greenhouse gases, and the global warming effect. In *Advances in carbon capture*, pages 3–28. Elsevier, 2020.
- [128] Rekabra Youssef, Jiacheng He, Mohsen Akbarzadeh, Joris Jaguemont, Lysander De Sutter, Maitane Berecibar, and Joeri Van Mierlo. Investigation of thermal behavior of large lithium-ion prismatic cell in natural air convection. In *2020 9th International Conference on Renewable Energy Research and Application (ICRERA)*, pages 43–47. IEEE, 2020.
- [129] Xiaoling Yu, Zhao Lu, Liyu Zhang, Lichuan Wei, Xin Cui, and Liwen Jin. Experimental study on transient thermal characteristics of stagger-arranged lithium-ion battery pack with air cooling strategy. *International Journal of Heat and Mass Transfer*, 143:118576, 2019.

- [130] Han Yuan, Shen Li, Tao Zhu, Simon O’Kane, Carlos Garcia, Gregory Offer, and Monica Marinescu. A electrochemical-electro-thermal coupled computational framework to simulate the performance of li-ion batteries at cell-level: Analysis on the thermal effects. *arXiv preprint arXiv:2303.09838*, 2023.
- [131] Xinghui Zhang, Zhao Li, Lingai Luo, Yilin Fan, and Zhengyu Du. A review on thermal management of lithium-ion batteries for electric vehicles. *Energy*, 238:121652, 2022.
- [132] Linpei Zhu, Fei Xiong, Hu Chen, Dan Wei, Gang Li, and Chenzhi Ouyang. Thermal analysis and optimization of an ev battery pack for real applications. *International Journal of Heat and Mass Transfer*, 163:120384, 2020.
- [133] Alana Zülke, Ivan Korotkin, Jamie M Foster, Mangayarkarasi Nagarathinam, Harry Hoster, and Giles Richardson. Parametrisation and use of a predictive dfn model for a high-energy nca/gr-siox battery. *Journal of The Electrochemical Society*, 168(12):120522, 2021.

Vita auctoris

NAME: Emanuele Lettieri

PLACE OF BIRTH: Eboli, Italy

YEAR OF BIRTH: 2001

EDUCATION: Liceo Scientifico E. Medi, Battipaglia, Italy, 2019

Politecnico di Torino, B.Sc, Turin, Italy, 2022

Politecnico di Torino, M.A.Sc, Turin, Italy, 2024

University of Windsor, M.A.Sc, Windsor, Canada, 2024